Extending the Measurement Range of High-speed Speckle Pattern Interferometry

Tao Wu

Submitted for the degree of Doctor of Philosophy

Heriot-Watt University

School of Engineering and Physical Sciences

September 2009

Abstract

A digital speckle pattern interferometer based on a complementary metal-oxide semiconductor (CMOS) camera was developed. The temporal evolution of dynamic deformation was measured using inter-frame phase stepping. A numerical and analytical investigation showed that the maximum surface velocity that can be reliably measured with inter-frame phase stepping corresponds to ±0.3 times the surface velocity at which the interferogram is sampled at the Nyquist limit (v_{Nyq}). The flexibility of the CMOS detector readout was used to identify regions of interest with full-field time-averaged measurements and then to interrogate those regions with time-resolved measurements sampled at up to 70 kHz.

To increase the surface velocity measurement range, spatial phase stepping was introduced to the high-speed CMOS system. A pair of binary phase gratings introduced double-channel sensing with a fixed phase step between the two channels. The maximum surface velocity was increased to $\pm 1.0 v_{Nyq}$. Sub-Nyquist theory was implemented for the dynamic measurements and the measurement range with a continuous-wave laser illumination was increased by an order of magnitude with respect to inter-frame phase stepping to $\pm 3.0 v_{Nyq}$. A numerical and analytical investigation showed that with a reduced exposure, for example from pulsed laser illumination, the maximum surface velocity that can be reliably measured is $\pm 15.9 v_{Nyq}$ and the surface acceleration is $\pm 253.3 v_{Nyq}$ with the current set-up.

Due to spatial variations in speckle intensity, some low-modulating and saturated pixels within the small regions of interest interrogated at up to 70 kHz could not be analysed. The nonlinear Linlog^{TM} response of the CMOS camera was used to increase the valid measurement area on the object surface by incorporating pixels that would be below a modulation threshold or saturated if recorded with a linear CCD detector.

Acknowledgment

First and foremost I am heartily thankful to my supervisor, Professor Andrew Moore, whose knowledge, support and encouragement enabled me to develop an understanding of the subject. I cannot expect a better supervisor, without him this thesis would not have been completed. He was always there to meet and talk about my ideas, ask me good questions and to help me solve my problems.

Thanks must be given to the colleagues in our research group, especially Steve Earl, Dr. Jesus Valera and Dr. Iain Wallace for their good questions, advice and kind assistance in the lab. My thanks must be extended to technicians in the department workshop, especially Cameron Smith, Richard Kinsella and Iain Drummond who gave kind support for my experiment.

I owe deep gratitude to my wife, Rong. She has given all her available support and advice on my research, experiments, paperwork, writing-up and daily life. I am greatly indebted to my parents for their unconditional and endless support, and understanding. Special thanks go to my son, Tong, who was born during the period of my PhD research and makes my life brilliant and promising.

Lastly, I offer my regards and blessings to all of those who supported me in any respect during the completion of the thesis.

Table of Contents

List of publications:

Journal

- T. Wu, J.D.C. Jones and A.J. Moore,
  "High-speed phase-stepped digital speckle pattern interferometry using a CMOS camera",
  Applied Optics 45(23) 5845-5855 (2006)

- T. Wu, S. Earl, J.D. Valera and A.J. Moore,
  "High-speed sub-Nyquist spatial phase-stepped speckle pattern interferometry",
  In preparation

- S. Earl, T. Wu, J.D. Valera and A.J. Moore,
  "Modal analysis with an optical multipoint vibrometer",
  In preparation

Conference

- T. Wu, A.J. Moore and J.D.C. Jones,
  "Dynamic phase-stepped digital speckle pattern interferometry"
  in Photon 04 (Glasgow) 38 (Institute of Physics, Bristol, 2004) No ISBN

- T. Wu, S. Earl, J.D.C. Jones and A.J. Moore,
  "High speed, sub-Nyquist speckle pattern interferometry using two binary diffraction gratings",
  in Photon 06 (Manchester) 50 (Institute of Physics, Bristol, 2006) No ISBN
  Awarded FASIG prize for Outstanding Student Presentation

- S. Earl, T. Wu, J.D.C. Jones and A.J. Moore,
  "Modal analysis with a CMOS multipoint vibrometer",
  in Photon 06 (Manchester) 87-88 (Institute of Physics, Bristol, 2006) No ISBN

- S.Earl, T. Wu, J.D.C. Jones and A.J. Moore,
  "High-speed multipoint vibrometer for modal analysis",
  in *Seventh International Conference on Vibration Measurements by Laser Techniques: Advances and Applications*, E.P. Tomasini (ed), Proc. SPIE 6345 Paper 6345-38 (SPIE Bellingham, WA, 2006) ISBN: 9780819464217

- S. Earl, T. Wu, J.D.C Jones and A.J. Moore, P. Daborn, A. Tribe, P. Hayden, P. Ind and G. Smith,
  "Impact testing with a high-speed multipoint vibrometer",
  in *IMAC 26: Structural dynamics*, A.L. Wicks (ed), Paper 132 (SEM, Bethel, CT, 2008) ISBN: 0-912053-98-4

1

Introduction

In this short chapter a brief overview of the thesis is presented.

1.1 Background to the project

Vibration measurement is vital in design for reliability and the reduction of noise emission. It is essential to know which modes are excited and the phase of vibration in natural vibration conditions. Established measurement techniques based on conventional sensors require instrumentation using contacting transducers, with concomitantly long measurement times, poor spatial resolution and perturbation of the structure under investigation by the transducer loading. Laser scanning devices have been used as a surface detection tool. However, due to the time-consuming nature of point-by-point measurements, it can take a long time to perform the surface measurement. Traditional full-field interferometers can not provide time-resolved measurements due to their relatively low sampling rate compared to the vibration period.

The work presented in this thesis is the result of an experimental and theoretical investigation into the application of high-speed speckle pattern interferometry (SPI) for vibration measurement. The objective of the work was to extend the measurement range of an existing high-speed SPI system that used a charge coupled device (CCD) line-scan camera in order to measure displacement, velocity and frequency of vibrating test components. As will be described later, the maximum reported surface velocity measured with the existing CCD system was a modest 3.2 mm s^{-1} (or 0.3 of v_{Nyq}). The

existing system also incorporated a second full-field CCD detector to identify the position of the line imaged by the high-speed line-scan CCD detector. A second objective was to use the flexibility of a complementary metal-oxide semiconductor (CMOS) detector readout to identify regions of interest with full-field time-averaged measurements and then to interrogate those regions with high-speed measurements from smaller identified regions of interest.

1.2 Organization of the thesis

Chapter 2 reviews existing optical vibration measurement techniques including the CCD-based inter-frame phase stepping system. Other areas from the literature that are relevant to the work presented in this thesis are also reviewed, specifically spatial phase-stepping approaches and sub-Nyquist interferometry applied to the measurement of surface profiles with large slope.

The experimental work is divided into three chapters. Chapter 3 describes a new high-speed SPI interferometer that was constructed as a starting point for the experimental work. The system incorporated inter-frame phase stepping, fibre or bulk-optics and a compact interferometer head mounted directly to a CMOS camera. The construction and optimization of the interferometer is described, and the first quantitative results with a CMOS camera in high-speed SPI were obtained. The measurement accuracy and the practically achievable measurement range ($\pm 0.3\ v_{Nyq}$) were assessed experimentally and theoretically for the first time.

Once the error sources and surface velocity measurement limit had been identified for inter-frame phase stepping, Chapter 4 describes the introduction of spatial phase stepping to the CMOS SPI system. The experimental system is the first introduction of binary phase gratings for spatial stepping. Spatial phase stepping immediately doubles the potential maximum surface velocity and eliminates the errors associated with the local linear velocity approximation made in inter-frame phase step SPI. Sub-Nyquist theory was then applied to the measured normalised velocity (modulo 2π) obtained from dynamic measurements for the first time. The measurement accuracy and the practically achievable measurement range ($\pm 3.0\ v_{Nyq}$ for continuous wave illumination) were established experimentally and theoretically for the first time. The measurement range of the new interferometer was improved by more than ten times that of inter-

frame phase step SPI, and could be significantly further increased with the use of a pulsed laser to restrict the exposure period further.

Due to spatial variations in speckle intensity, some low-modulating and saturated pixels within the CMOS small regions of interest could not be analysed. In full-field interferometry these lost data points are generally not too troublesome: many neighbouring points are usually available. However, this loss of data is more critical in high-speed applications where the vibration at adjacent pixels may not be continuous and the number of measurement points is already reduced. Chapter 5 describes the use of the nonlinear Linlog^{TM} response of the CMOS camera for the first time in SPI to increase the valid measurement area on the object surface by incorporating pixels that would be below a modulation threshold or saturated if recorded with a linear CCD detector.

Chapter 6 concludes the thesis with a discussion of the techniques proposed. A typical application of the interferometer is presented to measure the modal response of an object of interest to AWE. Potential areas for future development are discussed.

2

Literature Review

This chapter reviews current optical techniques which have been applied to vibration measurement. Techniques capable of measuring single-point or whole-field displacement, velocity and vibration frequencies are reviewed. Spatial phase step and applications of sub-Nyquist theory that extend the measurement dynamic range of spatial measurements are reviewed.

2.1 Single point laser vibrometry

Vibration measurement is often used to analyze the dynamic response of engineering objects under excitation. A complete assessment of vibration usually requires the measurement of amplitude, frequency and phase of the vibration. Traditionally accelerometer based methods have been used in vibration measurement. However, it is often not possible to determine the spatial shape of a vibration mode with an array of accelerometers due to the number of accelerometers and mass they add to the object. Hence a single accelerometer is often moved about the surface in a series of repeated tests. Whilst this approach is successful for many applications, phase information is lost for transient events.

For light structures, the attachment of a contacting transducer may change the dynamic response of the object. This is even more significant when measurements are to be taken from several points, since the dynamic response may change due to the relocation of the transducer. For such situations, optical techniques are well suited for vibration

measurement and can be traced to the earliest days of optical methods. The development of laser Doppler vibrometers (LDV) [1, 2,] for use in engineering testing was stimulated by the abilities of easily detecting sub-nm amplitudes vibrations over a frequency range from static to MHz. The technique utilizes the fact that light scattered from a moving object is frequency shifted with respect to a reference beam. A secondary illumination on the target at a different angle can also be used for in-plane measurement.

In rotating machinery, the most common measurement is that of the vibration transmitted into a non-rotating component using a contacting transducer. But in some situations, low vibration transmission can make this unreliable. Therefore, a non-contacting transducer capable of measuring at any location along the rotor is desirable. One of the earliest reported applications of LDV in this field was for axial vibration measurement directly from a rotating turbine blade[3]. Some work has also gone into developing portable instruments which have been demonstrated in analyzing the vibration levels of a rotating diamond-impregnated circular saw blade to design a suitable noise control damping pad for the saw[4].

In addition to the point-by-point operation of the LDV, it has been reported that the instrument can function in a continuous scanning mode for modal testing by Ewins [5, 6, 7]. The measurement beam was continuously swept over the surface of the object to give vibration measurements over the surface of a sinusoidally excited structure. The LDV vibration output was an amplitude-modulated sine wave so that mode shapes defined along the scan line could be retrieved by demodulation. Alternatively, in the frequency domain, the LDV output was a line spectrum, with sidebands centred on the excitation frequency and spaced at the scan frequency. The sideband amplitudes gave series coefficients for the mode shape defined along the scan line. Ewins[8] further extended the scanning LDV technique into measuring the response mode shape of a surface vibrating in a sine wave with excitation at a known specific frequency. Provided the mode shape is smooth within the scanned area, the mode shape could be derived by using a sinusoidal area-scan LDV. LDV is however subject to "speckle drop-out" due to the speckle noise on the surface of the test object. An analysis of the speckle noise was recently performed[9]. A theoretical model of speckle was developed and tested by comparing analytical results with experimental data. It was concluded that when a continuous scanning technique is used, the speckle noise is concentrated at the scan frequency and its harmonics. Therefore the scan speed needs to be chosen carefully so

as to avoid any of its harmonics overlapping with the structural vibration frequency and its sidebands. If this condition is fulfilled, the noise influence on the LDV output can be totally neglected by performing a targeted Fourier transform at the excitation frequency to reduce speckle noise in the sidebands that carry the vibration information.

LDV can offer benefits where high-frequency operation or high-spatial resolution is demanded, or the structure is light or rotating. However, the technique has two limitations: firstly the risk of any temporal changes in the vibration response during the scanning of the whole object; secondly objects need to be vibrating harmonically or rotating at constant frequency, where a periodic synchronization signal can be obtained for the scanning mirror. For example, transient vibrations with a period shorter than the scanning mirror period (typically a few seconds) would be impossible for LDV to measure.

Metro laser Inc[10] has developed a VibroMet^{TM} multiple beam laser Doppler vibrometer (MB-LDV) for simultaneously measuring vibrations at multiple location on a target. In this way, transient events can be measured at, for example 16 points at the same time. This system is superior to single beam scanning methods, especially when measuring temporally non-stationary responses during interrogation is necessary. However, the measurement beams must be well separated so that no interference will be caused between beams. The system has been used to measure objects with well spread regions of interest, including the discrimination of buried mines.

Fleming[11] has developed a multipoint vibrometer to acquire time-dependent structural vibration data at multiple points on an object surface. The system is based on a Doppler vibrometer with different kinds of imagers, such as CMOS cameras, linescan cameras to obtain data. Diffractive optics are used to generate multiple measurement beams and eliminate the necessity of a scanning laser beam. This system suffers a similar limit to Metro laser Inc's system as the measurement points must be discrete.

2.2 Holographic interferometry for vibration measurement

Some solutions for the whole-field measurement of vibration with optical techniques have been proposed. These techniques give displacement and vibration information

over an area without any sort of scanning. Holographic interferometry (HI) was one of the first optical techniques used for full-field vibration measurement.

Holography was invented by Dennis Gabor in 1948 as a method for recording and reconstructing the amplitude and phase of a wavefront [12]. A hologram is the photographically recorded interference pattern of a wavefront scattered from the object and a coherent reference wavefront. Once the hologram is recorded, the object wave can be reconstructed by illuminating the hologram with the reference beam. An observer can see a 3-D image which exhibits all the effects of perspective and depth of focus. Holographic interferometry was developed in the late 1960s by Stetson and Powell[13]. HI enables measurement of displacements of rough surfaces with an accuracy of a fraction of a micrometer. Holograms of an object in different states could also be combined to form an interferogram with fringe patterns indicating the differences between states[14]. However, to calculate the interference phase distribution of a light wave, additional information needs to be recorded. The most commonly used techniques are phase-stepping or phase-shifting method [15]. Three or more interferograms are reconstructed with mutual phase steps. The interference phase can be calculated from these phase-stepped interferograms. Practical limitations of HI include the stability requirement during and between exposures and the accurate film repositioning for real-time viewing. The optical elements used in making the hologram must be stable and even imperceptible motions of the object may completely blur out the recording.

However, Powell and Stetson[16] found that if the motions are not too severe, they will alter the image formed by diffraction from the hologram in a manner that is characteristic of the motion itself. This effect lead to a method for determining the vibration mode shape of a vibrating object. A hologram of the time-average of the coherent wavefronts scattered from a vibrating object was studied as shown in Figure 2.1. The image reconstructed by the hologram was found to contain a system of interference fringes which map contours of vibration amplitude.

Holography was recently combined with a digital camera to eliminate photographic recording and developing process required by conventional holography, which is called digital holography[17]. Digital holography employs a reference beam which is almost collinear with the object beam so that the resolution requirement of the recording medium is greatly reduced. Holograms are directly recorded by the detector (for

example CCD camera) and digitized and reconstructed by a computer. Digital holography is also more convenient and economical than conventional HI because of the elimination of photographic recording. Furthermore, the effective exposure time is much shorter than conventional holography. Zhang *et al.*[18] obtained the time-averaged complex amplitude of the Fresnel diffracted field due to a vibrating object, by using a three-step phase-stepping algorithm.

The phase of the recorded wavefront can be calculated directly from a digital hologram without generating phase-stepped interferograms, giving the possibility of applying digital holography to the measurement of transient events. In this case, image intensifying components are needed due to the light starving nature of dynamic measurement.

A digital holography system for whole-filed measurement of displacement, velocity and acceleration of a vibrating object has been reported[19]. The method was based on a series of digital holograms which were captured by a high-speed CCD camera. Fourier analysis and windowed Fourier analysis in both spatial and temporal domains were used to extract the information. However, the technique based on Fourier analysis did not give an exact reconstruction of the light field but only an approximation. The accuracy depends heavily on the high frequency and narrow spectrum of the fringes. However, in many cases the spectrum is wide due to the nature of the vibration, i.e. non-linear phase change.

2.3 Speckle pattern interferometry

Speckle pattern interferometry (SPI) has become an important diagnostic tool in many applications including the measurement of strain[20], displacement[21], vibration[22] and shape[23]. Laser speckle patterns arise whenever light from a coherent source illuminates an optically rough surface. A surface is optically rough if the local surface height deviations are greater than the wavelength of the light[24]. When light illuminates an optically rough surface, each point in the illuminated region scatters light. If the light is coherent, the light scattered from different points in the illuminated region will combine and produce an interference pattern. The speckle pattern is therefore the sum of the interference from all points in the region. A speckle pattern exists in all of the

surrounding space and can be observed on a viewing screen placed some distance from the illuminated region. The speckle pattern seen on the screen is known as an objective speckle pattern. The average size of an objective speckle, generated from a region with the diameter of D, is given by:

$$\Delta x = \frac{L\lambda}{D} \qquad \textbf{(2-1)}$$

where L is the distance between the viewing screen and object and λ is the wavelength of the light. The speckle is termed "objective", because for a given illumination, the scale of the speckle depends only on the position of the plane where it is viewed.

If such a speckle pattern is imaged onto the screen by a lens, a "subjective" speckle pattern is formed. The spatial distribution of this speckle is determined by the diffraction limit of the imaging system. Subjective speckle size is taken as the separation between the first two minima of the diffraction Bessel function and thus is dependent on the focal length f and lens aperture D_a. The average size of an individual subjective speckle observed at the imaging plane may be expressed as:

$$\sigma \approx \frac{\lambda f}{D_a} \qquad \textbf{(2-2)}$$

Speckles were initially considered as an addition and unwanted effect of the laser. Most of the early research into laser speckle was aimed at its reduction, because the speckle noise deteriorates the quality of holographic reconstruction. Later work to use the information carried in laser speckle became known as speckle metrology. Speckle pattern interferometry (SPI) was developed in the early 1970s[25]. The technique has progressed from photographic recording, through analogue video recording on to its current implementation with digital CCDs. The electronic processing of video and CCD camera signals eliminated the wet processing that had been somewhat problematic in conventional holographic interferometry, whilst the optical setup and subsequent processing are somewhat more straightforward than for digital holographic interferometry.

A typical interferometer for out-of-plane displacement measurement (i.e. sensitive to displacements normal to the object's surface) is shown in Figure 2.2. Light from the laser is collimated and divided by a beam splitter into two beams, which are the object beam and the reference beam. A polarising beamsplitter is shown in the figure, which enables the intensity ratio between the two beams to be varied. Also, highly birefringent (polarisation maintaining) fibre optic cable is drawn, enabling the polarisation state of the two beams emerging from the two fibres to be matched. The reference beam is modulated by a phase modulator to generate phase steps between the two interfering beams. The object beam is expanded to illuminate the object. The scattered light is collected by zoom lens and forms an image of the object that contains a laser speckle pattern. Light from the reference beam interferes with the speckle image and an interferogram is produced on the sensor. For out-of-plane SPI, the intensity of the reference beam recorded at the detector should generally be approximately 3-4 times the mean intensity of the object beam in order to obtain high contrast fringes. Light is scattered from the object and therefore only a small amount of the object beam is returned to the sensor. For this reason typically 90% of the light from the laser goes into the object beam and 10% goes into the reference beam.

The intensity of the interferogram recorded by the sensor[26] can be represented by equation (2-3):

$$I_1(x,y,t) = I_o + I_r + 2\sqrt{I_o I_r}\cos[\psi(x,y) + \phi(x,y,t)] \qquad \textbf{(2-3)}$$

where $I_o(x,y)$ and $I_r(x,y)$ are the intensities of the object and reference beams measured by the detector, and the coordinates x and y describe the pixel position in the plane of the detector. It is assumed that the beams are mutually coherent and have equivalent states of polarization. The phase $\psi(x,y)$ describes the random optical path difference between the object and reference beams due to laser speckle and $\phi(x,y,t)$ is a phase due to the difference in optical path length between the object and reference beams.

For the out-of-plane SPI system of Figure 2.2, the object illumination is approximately collinear with the optic axis of the imaging lens and camera, which is defined as the z-axis. The component of object deformation or displacement resolved in the z-direction produces a change in the optical path length of the object beam, producing a change in

the interferogram phase $\phi(x,y,t)$ and hence interferogram intensity. The phase change for a wavefront that has traveled an extra distance l in the z-direction is given by,

$$\Delta\phi = \frac{2\pi}{\lambda}\int_0^l n_z dz \qquad \textbf{(2-4)}$$

where λ is the wavelength of the laser and n is the refractive index of the object beam medium along the z-direction. For a medium of uniform refractive index, equation (2-4) simplifies to,

$$\Delta\phi = \frac{2\pi}{\lambda} l \qquad \textbf{(2-5)}$$

After the target is deformed, the new interferogram intensity can be expressed by equation (2-6).

$$I_2(x,y,t) = I_o + I_r + 2\sqrt{I_o I_r}\cos[\psi(x,y) + \phi(x,y,t) + \Delta\phi(x,y,t)] \qquad \textbf{(2-6)}$$

where $\Delta\phi$ is the phase change due to the displacement of the target. Due to the random speckle phase, displacement information contained in the change in intensity is not easily discerned without further processing. Therefore the two interferograms I_1 and I_2 are compared, usually by addition or subtraction, as described in the following section.

2.4 Fringe formation in SPI

One of the advantages of SPI is its ability to display a fringe pattern in real-time. Such fringes represent contours of constant displacement resolved in the sensitivity direction of the interferometer. Fringe patterns are generally produced by adding or subtracting the speckle interferograms denoted by equations (2-3) and (2-6). Addition fringe patterns are produced by the double exposure of a photographic or CCD detector (for example with double-pulsed SPI described in Section 2.5.2) and are described by:

$$I_A(x,y,t) = I_2 + I_1 = 2(I_o + I_r) + 2\sqrt{I_o I_r}\,(\cos[\psi+\phi] + \cos[\psi+\phi+\Delta\phi])$$
$$= 2(I_o + I_r) + 4\sqrt{I_o I_r}\cos\left(\psi+\phi+\frac{\Delta\phi}{2}\right)\cos\left(\frac{\Delta\phi}{2}\right) \qquad \textbf{(2-7)}$$

Subtraction fringes are generally produced with continuous wave illumination used for static or harmonic vibration deformations, and are described by:

$$I_S(x,y,t) = I_2 - I_1 = 2\sqrt{I_o I_r}\,(\cos[\psi+\phi] - \cos[\psi+\phi+\Delta\phi])$$
$$= 4\sqrt{I_o I_r}\sin\left(\psi+\phi+\frac{\Delta\phi}{2}\right)\sin\left(\frac{\Delta\phi}{2}\right) \qquad \textbf{(2-8)}$$

For both equations (2-7) and (2-8) the (x,y,t) dependence in terms on the right-hand side have been dropped for clarity. The visibility for addition fringes is lower than for subtraction fringes due to the background intensity term $2(I_o + I_r)$. For subtraction fringes, negative intensity values are usually removed by assigning the absolute value of the intensity difference or squaring the signal. The term $\sin(\psi+\phi+\Delta\phi/2)$ in equation (2-8) represents the high spatial frequency random speckle phase in the image and $\sin(\Delta\phi/2)$ represents a lower spatial frequency modulation i.e. the fringe pattern. The speckle noise can be suppressed with a lowpass filter, reducing the fringe pattern to a form that is proportional to $(1-\cos\Delta\phi)$.

It can be seen that when the interference phase satisfies the condition:

$$\Delta\phi = 2m\pi \qquad m = 0,1,2... \qquad \textbf{(2-9)}$$

the intensity at an individual pixel returns to its original value and the subtraction fringe intensity is zero. Elsewhere, the intensity recorded at a given pixel varies between the two exposures and the absolute or squared intensity difference is non-zero, taking a maximum value whenever the condition

$$\Delta\phi = (2m+1)\pi \qquad m = 0,1,2... \qquad \textbf{(2-10)}$$

is satisfied. Differences between the two speckle interferograms are therefore revealed by alternating bright and dark fringes corresponding to loci of equal phase difference

between the two wavefronts. Similarly for addition fringes, the fringes appear as regions of changing speckle contrast corresponding to loci of equal phase difference between the two wavefronts. The phase difference is related to the optical path difference introduced by the displacement of the object, and for the system shown in Figure 2.2, is given by:

$$\Delta\phi = \frac{2\pi}{\lambda}\eta w \qquad \textbf{(2-11)}$$

where η is the interferometer's sensitivity to object displacement, w, resolved in the observation direction. For collinear illumination and observation directions $\eta = 2$. For observation normal to a plane surface, w is the out-of-plane plane displacement of the object. Then the difference in out-of-plane deformation between adjacent fringes is $w = \lambda/2$.

Addition and subtraction techniques are still commonly used for qualitative real-time fringe visualisation. However, with the development of phase stepping techniques in the 1980s, it is now more common for quantitative fringe analysis to calculate two phase maps from phase-stepped interferograms corresponding to equations (2-3) and (2-6) and to calculate the phase difference directly[27, 28]. These techniques are used in inter-frame phase-stepped high-speed SPI and are described in Section 2.5.3.

2.5 SPI for vibration measurement

There are three general SPI techniques that have been widely used for vibration measurement: a) the time-averaged method, b) pulsed and stroboscopic methods, and c) high-speed phase-stepping methods. These approaches are described in the following sections.

2.5.1 Time-averaged SPI

Butters and Leendertz first employed SPI for measurement of out-of-plane vibration. Provided that the vibration period is significantly shorter than the detector exposure period, and the vibration is harmonic, time-averaged SPI fringes showing regions of equal vibration amplitude can be observed.

By assuming that a complete number of cycles of the harmonic surface motion, $w_n = w_o \cos(\Omega t + \Phi)$, occur during an exposure, equation (2-3) can be evaluated to give the following:

$$I_1(x,y) = I(x,y)[1 + V\cos(\psi) J_0(\frac{2\pi\eta w_o}{\lambda})] \quad \textbf{(2-12)}$$

where $I(x,y) = I_o(x,y) + I_r(x,y)$. $V = \frac{2\sqrt{I_o I_r}}{I}$ is the visibility of the interference and achieves its maximum value (unity) only if the two combining beams are of equal intensity and state of polarization and are mutually coherent. Equation (2-12) contains information on the vibration amplitude w_o, but information on the vibration frequency, Ω, and vibration phase, Φ, has been lost. J_0 is the zeroth-order Bessel function, and it is the term $J_0(\frac{2\pi\eta w_o}{\lambda})$ in equation (2-12) that contains useful information about the vibration amplitude. The signal-to-noise ratio is degraded by the background intensity $I(x,y)$, in a similar way to addition fringes, equation (2-8). To improve fringe visibility, two time-averaged speckle images can be recorded with a π phase step between recordings. The second image, when the object is also vibrating, can be represented by:

$$I_2(x,y) = I(x,y)[1 + V\cos(\psi + \pi) J_0(\frac{2\pi\eta w_o}{\lambda})] \quad \textbf{(2-13)}$$

With sequential subtraction analysis, each frame acts as the reference frame for the next so that the reference frame is constantly refreshed. The advantage of sequential subtraction over static subtraction (in which a single reference frame from the beginning of the sequence is used) is that environmental noise below the detector frame rate is eliminated. Subtraction of the two frames yields,

$$I_1 - I_2 = 2IV\cos(\psi) J_0(\frac{2\pi\eta w_o}{\lambda}) \quad \textbf{(2-14)}$$

As previously described, negative intensity values are usually removed by assigning the absolute value of the intensity difference or squaring the signal. Figure 2.3 shows the

form of the $J_0^2(\eta)$ function, which indicates that the brightest fringe corresponds to an argument of zero. That is, the brightest time-averaged fringe corresponds to a node of the motion. Equation (2-14) also shows that time-averaged fringes contain no information about the phase of the vibration.

Figure 2.4 shows time-average vibration amplitude fringe patterns recorded with a CMOS camera at 25 frames per second for a circular aluminum plate recorded by the author. The plate had a diameter of 14 cm and was vibrating at different natural frequencies. The vibration amplitude for a cross-section of the plate marked in Figure 2.4(b) is plotted in Figure 2.5, calculated from equation (2-14) and Figure 2.3. As can be seen, only the vibration amplitude is obtained: the vibration phase is lost for time-averaged measurements.

The brightest fringes correspond to vibration nodes and the fringe intensity decreases with increasing vibration amplitude. Subsequent fringe orders are of low contrast and calculation of the vibration amplitude is difficult from the Bessel fringes. Hogmoen[29] increased the measurement sensitivity by driving a modulating mirror at a frequency that was slightly different from the vibration of the object. Lokberg[30] proposed that contours of constant vibration phase can be observed by combining the time-averaged SPI with phase modulation. Nakadate[31] used a level-slicing technique to increase the contrast of a fringe pattern. Joenathan[32] developed two digital image processing methods to optimize fringe contrast and quality: a max-min scanning method and a normalized max-min scanning method. The max-min scanning method increases the contrast of the fringe pattern, while the normalized max-min scanning method reduces the speckle noise.

2.5.2 Pulsed and Stroboscopic SPI

Pulsed SPI was first reported in 1978[33] with a double-pulsed laser and a low speed camera was used to record addition and subtraction fringes. Pulsed lasers can provide a number of advantages over continuous wave lasers for vibration measurement. Compared to the time-averaged technique which generates Bessel fringes, pulsed illumination generates fringes with a cosinusoidal profile which are easier to analyze. Moreover, measurements can be made on relatively unstable objects which are subject to rigid body motion or environmental or thermal disturbance. Measurements can

therefore be made away from optical bench. Furthermore, the fringe patterns obtained contain limited information about object vibration amplitude and phase for simple vibration modes. The time-averaged technique can only be used to measure harmonic motion.

With pulsed techniques, it can be arranged that the laser pulses are short compared to the vibration period, so that the object motion is effectively frozen. Therefore even transient surface vibrations can be analyzed, provided that the duration of the laser pulse is significantly shorter than the period of the vibration. One laser pulse is fired to record a reference speckle pattern when the object is at some initial position. Then another laser pulse is fired to record another speckle pattern when the object has deformed. The two speckle patterns recorded correspond to two positions of object vibration'. Comparison of these speckle patterns gives the deformation of the surface between the two pulses. There are three typical modes of operation, namely addition[33, 34], subtracted-addition[34, 35, 36, 37] and subtraction. By the addition method, a double-pulsed laser fires double pulses with a very short pulse separation within a single frame. The resultant addition fringes contain stationary optical noise that reduces the fringe visibility. However, the addition-fringe visibility can be increased by analogue[33, 34] or digitally[38] filtering an addition interferogram. For subtraction pulsed SPI, an interline-transfer CCD cameras has proved to be very effective. Spooren[39] first demonstrated the improvement in fringe visibility compared to addition SPI, whilst maintaining a very short (microsecond) pulse separation. Pedrini[40] also developed a double-pulsed SPI system, in which two separate speckle patterns of an object were recorded within a few microseconds with an interline-transfer camera. The fringes were analyzed quantitatively by the spatial-carrier phase-step method. Using three directions of illumination and one direction of observation, three-dimensional deformation vector could be reconstructed.

For measurement of repeatable transient events, a series of tests under identical loading conditions can be conducted, incrementing the delay between the event start and the laser pulses until a complete composite history of the transient even is synthesized[41]. The reported system was used to obtain both subtraction and addition fringes. The setup was then applied to measurement of propagation of mechanical shock waves in a cantilever specimen and their subsequent diffraction by a crack in the specimen. Experimental results showed that double-pulsed-addition SPI was more attractive because it allowed the deformation in larger areas without exceeding the resolvable

fringe density and it was more insensitive to environmental disturbances. However, subtraction SPI was also of interest due to the improved fringe visibility.

Shellabear[42] developed a three-dimensional pulsed subtraction SPI system to measure the vibration of a turbocharger blade, a thick annular cylinder, and a centre-pinned free square plate. It was shown that the orthogonal displacement components could be measured independently and sequentially by SPI. A dual-beam illumination arrangement was used for in-plane vibration components. Vibration amplitude information was extracted using a single phase step technique for the horizontal and vertical components of in-plane vibration. The results were then combined to yield the total in-plane vibration mode.

With stroboscopic SPI, the object is illuminated by a series of laser pulses at a controlled vibration phase during a single exposure of the detector. As with pulsed illumination, the stroboscopic illumination exposure is short with respect to the vibration period so that integration of the intensity during the exposure produces a cosinusoidal intensity profile. Stroboscopic techniques are restricted to harmonic vibration measurement but do not require the bulky pulsed laser of single and double-pulsed approaches. Furthermore, techniques for measuring both vibration amplitude and phase have been developed with stroboscopic SPI. To show this, consider stroboscopic pulses are synchronised to the vibration corresponding to a phase difference between the object and reference beams from equation (2-3) of $\phi = \frac{2\pi\eta w_o}{\lambda}\cos(\phi_1 + \Phi)$. The intensity recorded is therefore:

$$I_1(x,y) = I\left\{1 + V\cos\left[\psi(x,y) + \frac{2\pi\eta w_o}{\lambda}\cos(\phi_1 + \Phi)\right]\right\} \quad \textbf{(2-15)}$$

A second speckle interferogram is then recorded, in which the laser pulses occur at some different phase with respect to the object vibration, and the intensity is then:

$$I_2(x,y) = I\left\{1 + V\cos\left[\psi + \frac{2\pi\eta w_o}{\lambda}\cos(\phi_2 + \Phi)\right]\right\} \quad \textbf{(2-16)}$$

Subtraction of equations (2-15) and (2-16) gives the following:

$$I_2 - I_1 = 2IV\sin(\psi')\sin\left\{\frac{2\pi\eta w_o}{\lambda}\sin\left[\frac{1}{2}\left(2\Phi+\phi_1+\phi_2\right)\right]\sin\left[\frac{1}{2}\left(\phi_2-\phi_1\right)\right]\right\} \quad \textbf{(2-17)}$$

where ψ' incorporates the high-spatial-frequency (speckle) phase term. For simplicity of expression, we assume that $\phi_1 = 0$ and $\phi_2 = \pi$, so that equation (2-17) becomes:

$$I_2 - I_1 = 2IV\sin(\psi')\sin\left(\frac{\Delta\phi}{2}\right) \quad \textbf{(2-18)}$$

where:

$$\Delta\phi(x,y) = \frac{2\pi\eta w_o}{\lambda}\sin\Phi \quad \textbf{(2-19)}$$

To achieve the maximum sensitivity, the laser pulses at ϕ_1 and ϕ_2 are chosen to coincide with vibration maxima and minima. As described previously for subtraction fringe formation, it can be assumed that the signal corresponding to equation (2-18) is first squared, in order to avoid negative values, and then low-pass filtered. The term $\sin(\psi')$ varies much more rapidly with position than $\sin(\Delta\phi/2)$; the low-pass filter reduces the fringe pattern to a form that is proportional to $(1-\cos\Delta\phi)$. Compared to time-averaged technique, stroboscopic measurements retain information regarding the phase of the object vibration, which appears in the term $\Delta\phi$. Thus, provided that the pulse phase ϕ_1 and ϕ_2 are known for the experiment, the phase of the object deformation can be measured.

Figure 2.6 shows stroboscopic SPI images of a circular plate vibrating at different natural frequencies obtained by the author. Figure 2.6(a) shows phase maps calculated by phase stepping subtraction SPI fringe patterns corresponding to equation 2-18, to obtain the phase shown by equation (2-19). A second phase map (not shown) was then recorded with the laser pulses shifted by π/2 radians with respect to the vibration phase, i.e. $\frac{2\pi\eta w_o}{\lambda}\cos\Phi(x,y)$. These two phase maps enable the vibration amplitude and vibration phase to be calculated[43]. Figure 2.6(b) shows the vibration amplitude scaled

between zero (black) and maximum (white). Figure 2.6(c) shows the vibration phase scaled between zero (black) and π radians (white). The rows of the figure show the vibration amplitude increasing and then decreasing as the excitation frequency scans through a natural frequency of the plate. Similarly the phase of vibration changes by π radians as the excitation frequency scans through the natural frequency.

2.5.3 High-speed inter-frame phase-stepping SPI

A high-speed CCD camera can be used to record many distinct instances of a transient event[44], enabling the study of non-repeatable events with respect to time. A schematic of that experimental system is in Figure 2.7. A 10-mw laser and single-mode fibre illumination was used with a 40-kHz CCD camera (64 × 64 pixels) to record transient deformation sequences. Vibration with microsecond temporal resolution was also measured as shown in Figure 2.8. Although the system incorporated a fibre-wound piezoelectric (PZT) cylinder for phase stepping, its bandwidth was insufficient for dynamic inter-frame phase stepping.

The optical phase changes due to the deformation of an object during the exposure time. For a vibrating object, the intensity recorded by the camera at pixel (x, y) during an exposure of duration t_e, centered at time t_n can be written as:

$$I_n(x,y,t_n) = I\left(1 + V\frac{1}{t_e}\int_{t_n - t_e/2}^{t_n + t_e/2} \cos\left[\psi + \frac{2\pi\eta w_o}{\lambda}\cos(\Omega t_n + \Phi)\right]dt\right) \qquad \textbf{(2-20)}$$

For camera short exposure periods with respect to the vibration period, we can approximate the deformation by a linear expansion, i.e. the surface velocity w_n' is assumed to be continuous. A sinc function arises because the integration time is relatively long compared to that of pulsed and stroboscopic illumination. Equation (2-3) can be rewritten as:

$$I_n(x,y,t_n) = I\left(1 + V\mathrm{sinc}\left[\frac{2\pi\eta}{\lambda}w_n'\frac{t_e}{2}\right]\cos\left[\psi + \frac{2\pi\eta w_o}{\lambda}\cos(\Omega t_n + \Phi)\right]\right) \qquad \textbf{(2-21)}$$

The instantaneous visibility of the recorded speckle pattern, $V\text{sinc}\left[\frac{2\pi\eta}{\lambda} w_n' \frac{t_e}{2}\right]$, depends on the relative phase change between the object and reference beam that occurs during the exposure, $\Delta = \frac{2\pi\eta}{\lambda} w_n' t_e$ for out-of-plane SPI. For maximum fringe visibility to be achieved, the argument of the sinc function should approach zero, requiring a low test-surface velocity and a short exposure time. The system was used to study brake disc and car door panel vibrations [45, 46].

Kilpatrick *et al.*[47] introduced inter-frame temporal phase modulation in high-speed SPI to produce a multi-point vibrometer. The system is shown schematically in Figure 2.9. An 80 mw laser diode, highly birefringent optical fibres and a lithium-niobate waveguide phase modulator were used. The detector was a line-scan camera (256 × 1 pixels) operating at 100 kHz, and vibration amplitude and phase were measured up to audio acoustic frequencies and for surface velocities up to 3.2 mm s^{-1}. Due to the small field of view of the detector, a second array detector was included to identify regions of interest (ROI). For the same overall data transfer rate (256 × 100 kHz = 25.6 MHz), fewer channels can provide a velocity limit that is sufficient for most engineering applications, e.g. 16 channels yields a surface velocity limit of ~160 mm s^{-1}.

For simplicity, equation (2-21) can be rewritten as:

$$I_n(x,y,t_n) = I\left(1 + V\text{sinc}\left[\frac{\Delta}{2}\right]\cos\left[\Phi_O - \Phi_R\right]\right) \qquad \textbf{(2-22)}$$

The object phase, $\Phi_O(x,y,t_n)$, comprises the random speckle phase, ψ, plus the phase due to out of plane deformation of the target, $\frac{2\pi\eta}{\lambda} w_n$. The reference phase, $\Phi_R(t_n)$, includes a phase-stepped increment with respect to the previous frame of $2\pi n/N$, where N is the number of steps per period. For $N = 4$, the argument of the cosine term in equation (2-22) can be recovered from the image by Carré's algorithm[48], where:

$$\Phi_O(x,y,t_n) - \Phi_R(x,y,t_n) = \tan^{-1}\left(\frac{\{[3(I_{n+1} - I_{n+2}) - (I_n - I_{n+3})][I_n - I_{n+3}) + (I_{n+1} - I_{n+2})]\}^{1/2}}{(I_{n+1} + I_{n+2}) - (I_n + I_{n+3})}\right) \qquad \textbf{(2-23)}$$

It is assumed that the frame rate is sufficiently high that the surface velocity is linear during any four consecutive frames and that the phase at a given pixel can be calculated from I_n to I_{n+3}. The speckle phase $\psi(x,y)$ can be eliminated and the out-of-plane deformation obtained at time $t_n = T$ relative to the deformation at $t = 0$, by summation of the incremental phase differences at the corresponding pixels between adjacent frames, where:

$$w(x,y,T) = \frac{\lambda}{4\pi}\sum_{n=0}^{T-1}[\Phi_O(x,y,t_{n+1}) - \Phi_O(x,y,t_n)] \qquad \textbf{(2-24)}$$

One advantage of processing each pixel independently in this way is that spatial unwrapping may fail if adjacent pixels are vibrating out of phase with each other i.e. there are discontinuities in the surface motion. When the data implicitly include some known or stationary reference, recovery of the absolute spatiotemporal profile is possible, equation (2-24). For the general case of continuous anharmonic motion with unknown initial deformation, it is best to present the phase changes between frames as surface velocity; i.e. the instrument can be considered to be a multipoint vibrometer.

The Nyquist condition, that the cumulative phase change be sampled at least twice per fringe, leads to a maximum working surface velocity for an out of plane system of with inter-frame phase stepping of:

$$v_{Nyq,PS} = \pm\frac{\lambda}{2\eta t_s}\left(1 \mp \frac{2}{N}\right) \qquad \textbf{(2-25)}$$

where t_s is detector frame period (i.e. $t_e \le t_s$). The upper and lower velocity limits correspond to the sense of the surface displacement relative to the phase step imposed on the reference beam. Unless the surface displacement is unidirectional and of known sense, the lower value sets the practical velocity limit for the system, which is maximized for $N = 4$.

Other implementations of moderately high-speed SPI include the measurement of uni-directional deformation with a moderately high-speed camera[49] (360 frames per second). The time-dependent speckle modulation due to optical path difference changes was tracked during the measurement and the Fourier transform method[50, 51, 52] was then used

to obtain the phase values of each pixel. The drawback of the Fourier transform technique is that the phase reconstruction is approximate. Relatively low-speed (25 μm s^{-1}) deformations were recorded using dynamic phase stepping at 1 kHz[53] and analysed by the temporal phase step method[54, 55, 56]. Neither of these two systems was intended for dynamic vibration measurements, which would require a substantial increase in bandwidth and change in data processing strategy.

For the temporal phase stepping approach for measuring surface deformation, the optimum phase re-referencing rate was investigated numerically for the case of linear deformations measured with respect to an initial deformation state. Local speckle averaging introduces errors in the accumulated phase due to speckle decorrelation that decrease as the number of frames between successive re-references of the phase decreases. Conversely, errors due to linear deformation changes and random camera intensity noise increase as the number of frames between successive re-references decreases. It was concluded that the optimum frame re-referencing rate, when these error sources are present simultaneously, corresponds to speckle translation in the pupil plane of 8%. It is shown in the following chapter that the accumulated errors are not of primary interest when the interferometer is acting as a multi-point vibrometer, when the effect of surface acceleration (i.e. non-linear surface motion) dominates. A method to reduce this kind of non-linear error is spatial phase stepping, in which the required images are recorded simultaneously with an appropriate fixed phase step between each of the images.

Ruiz and Huntley[57] raised the point that the camera framing rate and the carrier frequency of the system, which is equal to the ratio of the camera framing rate and the number of phase steps per cycle of the carrier, impose restrictions on the maximum specimen surface velocity that can be measured. The conclusion was that, for a relatively low vibration amplitude (for example λ/10), vibration frequencies up to 30% of the carrier frequency can be measured with an rms phase change error less than 10% of the vibration amplitude.

Kauffmann and Tiziani[58] have developed a temporal speckle pattern interferometry (TSPI) system for measuring the displacement of rough technical surfaces. The time-dependent speckle modulation due to optical path difference changes was tracked during the displacement of the surface and then evaluated pointwise. A sequence of images was acquired and evaluated by the Fourier transform method. The signal was

Fourier transformed and one side of the spectrum was filtered with a bandpass filter. By using inverse Fourier transform of the filtered spectrum, a complex signal was obtained and the phase component of the displacement could be extracted. The feasibility of time-resolved vibration measurements was demonstrated. Pedrini[59] also developed a system based on digital holographic interferometry and Fourier transform method for the measurement of vibration. The system used a high power CW laser (10 W) and a high-speed CCD camera. The phase of the wavefront is calculated from the holograms by a 2-D Fourier transform. However, this technique didn't give an exact reconstruction of the wavefront but only an approximation. Also the low-amplitude signals and sub-sampled signal could be problematic.

2.6 Spatial phase step SPI

Spatial phase stepping is an alternative to inter-frame phase stepping for calculating the phase in an interferometer. Spatial phase stepping records two or more phase stepped images simultaneously and is therefore immune to time-related instabilities, although it is more susceptible to image alignment errors. Spatial phase steps are typically introduced by gratings[60, 61], polarizing elements[62, 63] or zone plates[64]. For example, Kwon[65, 66] reported a stroboscopic system based on a pair of gratings and three cameras to measure the surface deformation of a sonically activated pellicle mirror in a time-sliced fashion at 50-μsecond intervals, where steps of $2\pi/3$ radians were generated by lateral translation between the gratings.

Specifically for speckle interferometry, Frankena [67, 68] developed an interferometer to record three phase-stepped speckle interferograms simultaneously. The proposed system used Glan-Thompson polarizing prisms to direct the combined beams onto three cameras and introduce phase steps between them. The system was evaluated for measurements of the out-of-plane rotation of a flat surface.

Upton[69] developed a calibrated multichannel interforemtry system to perform phase shifting of a transient flow visualization. The system was based on the use of a pair of diffraction gratings to produce three phase-shifted interferograms. The interferograms were aligned and pixel correspondence was determined. The multichannel

interferometer was calibrated by the use of piezoelectric phase shifting. The phase, modulation and bias of the optical system were determined. The system was then used to study the transient behaviour of a 2-D buoyant thermal plume at 82Hz. The development of the plume and the transition from radial conduction to convection as the air accelerates due to buoyancy was clearly showed

A spatial phase step system based on both grating and polarizing elements was used to measure the surface deviation of an array of small protruding cylinders[70]. In that system, the grating was used to divide the wavefront on to one CCD camera and separate polarizing optics were used to introduce the phase step.

Another implementation of spatial phase stepping used a computer generated holographic optical element (HOE) to simultaneously separate the image and to produce $\pi/2$ phase steps between diffracted orders[71, 72]. The system is shown schematically in Figure 2.10. The HOE was a modified crossed phase grating that introduced a known phase change between the ±1 diffracted orders without relative translation to a grating in the reference beam. The two exposures required in speckle interferometry (made before and after deformation) were recorded, enabling dynamic deformation and refractive index measurements in a thermal plume to be made with a pulsed interferometer. Carré's algorithm was used to calculate the phase of the progressive propagation of transient mechanical waves with an rms precision of $2\pi/30$. However, the phase step introduced was found to be dependent on the tilt of the HOE and required a mount for rotation of the element.

Millerd.[73] developed a polarization sensitive Twyman-Green interferometer which used a pixelated phase mask to introduce spatial phase stepping. The system was made commercially available by 4-D Technologies. The pixelated phase mask consists of a micropolarizer array which is divided into unit cells. Each unit cell consists of four pixels, each containing a wire grid polarizer orientated such that a relative phase step of $\pi/2$ is induced between each pixel. The phase mask consists of a combination of a half-wave plate and a quarter-wave plate to achieve quarter-wave retardation over a broad range of wavelengths. The images recorded by the CCD camera were then processed to calculate the phase. An earlier version of the Twyman-Green interferometer was described by Wyant[74], which used a HOE for beam division with the phase step being applied by a birefringent phase mask.

2.7 Sub-Nyquist interferometry

To measure the phase of a wavefront, a sequence of phase-stepped interferograms is recorded. The phase is calculated as the arctangent whose argument is a function of the intensities at that point. Then the measured phase can be scaled to give measurand of the optical system, e.g. displacement or surface shape. However, as a result of the arctangent, the calculated phase gives values between 0 and 2π, valid solutions must be found by adding multiples of 2π to the phase. The wavefront then needs be unwrapped to determine the proper multiple of 2π to be used.

By unwrapping the wavefront in this way, it is assumed that the sensor samples the fringe pattern at a spatial frequency at least twice the highest spatial frequency present in the pattern. Hence the absolute phase change between two neighbouring points should be less than π radians. Exceeding this range produces an ambiguity due to undersampling the wavefront. This sampling requirement limits the measurable wavefront slope to a half-wave per pixel. Therefore, if a scene is band limited to the Nyquist frequency, then the scene can be perfectly recovered from the sampled image.

If the scene is not band limited to the Nyquist frequency, fringes that occur beyond the Nyquist frequency are aliased and appear as low frequencies in the recorded image. Grievenkamp[75, 76] stated that, by using a priori information about the wavefront being measured, the aliased fringe pattern can be recovered by sub-Nyquist theory. It is assumed that the reconstructed slope is continuous to give a correct wavefront reconstruction. In contrast, the traditional spatial unwrapping methods recover the wavefront by assuming that the surface is continuous. Grievenkamp introduced sub-Nyquist theory into measurement of surface profiles with large aspheric departures. When large asphericity is measured, a reasonable assumption, such as the continuity of the surface derivatives, was used in data analysis to yield dramatic increases in the measurement range of the interferometer.

Grievenkamp noted that the physical limitations of the Nyquist limit were merely due to the reconstruction (unwrapping) algorithm, if the wrapped phase values were calculated accurately. For sub-Nyquist theory to be applicable, the interferometer must measure accurately the phase (modulo 2π). The effect of a large pixel area is to average the intensities over this active area. When one fringe fits inside one pixel, no information can be recovered as there will be no modulation. Therefore sub-Nyquist interferometry

was implemented with a reduced active pixel area in order to obtain reasonable modulation of the high-spatial frequency fringes. It was claimed that a sensor with a pixel pitch-to-width ratio of 0.1 enables the system to respond to spatial frequencies up to twenty times the sensor Nyquist frequency.

To exceed the Nyquist limit, Servin[77] proposed to calculate the temporal phase variation by calculating spatial phase gradient across the test surface. Displacement of the surface was obtained by summing up the variation of spatial phase gradient. The maximum surface velocity that could be measured may exceed the Nyquist limit. This method is limited to surfaces with slow spatial phase change and needs to take two orthogonal interferograms simultaneously by two cameras.

Munoz[78] utilized sub-Nyquist theory to phase recovery from a single undersampled interferogram. Two low-fringe-density synthetic interferograms corresponding to the phase differences along orthogonal directions were calculated from neighboring pixels of the aliased measured data. The only assumption was that the illumination background, the modulation intensity, and the searched phase were smooth and continuous functions. By using a least-squares method, the phase was then recovered by integration of the phase differences. Ferraro[79] combined lateral-shearography interferometry with sub-Nyquist theory to obtain a profile even in extreme cases where the phase profile changes very rapidly. Falldorf[80] presented a method that allows the reconstruction of smooth phase distributions from their laterally-sheared representation.

2.8 Summary

This chapter has reviewed the literature on full-field optical techniques for vibration measurement. Specifically for speckle pattern interferometry, the time-averaged method has the typical advantage of optical techniques, i.e. non-contact measurement, but is restricted to the measurement of harmonic events and the vibration phase is lost. Similarly, stroboscopic and pulsed techniques are most suited to harmonic events due to the requirement of synchronization. High-speed phase-step SPI is a promising technique for measuring general transient and anharmonic deformations. However, the widely used inter-frame phase step technique implemented to date offers a relatively

low measurement range due to the Nyquist limit [81] imposed on sampling the intereference pattern.

In this thesis, CMOS detectors, the spatial phase step technique and sub-Nyquist interferometry are investigated as possible methods to extend the measurement range of SPI.

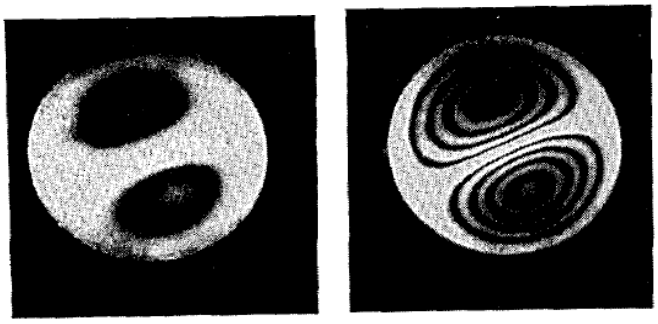

Figure 2.1 Photographs of the reconstructions of two holograms of a film-can bottom with increasing vibration amplitude at the second resonance

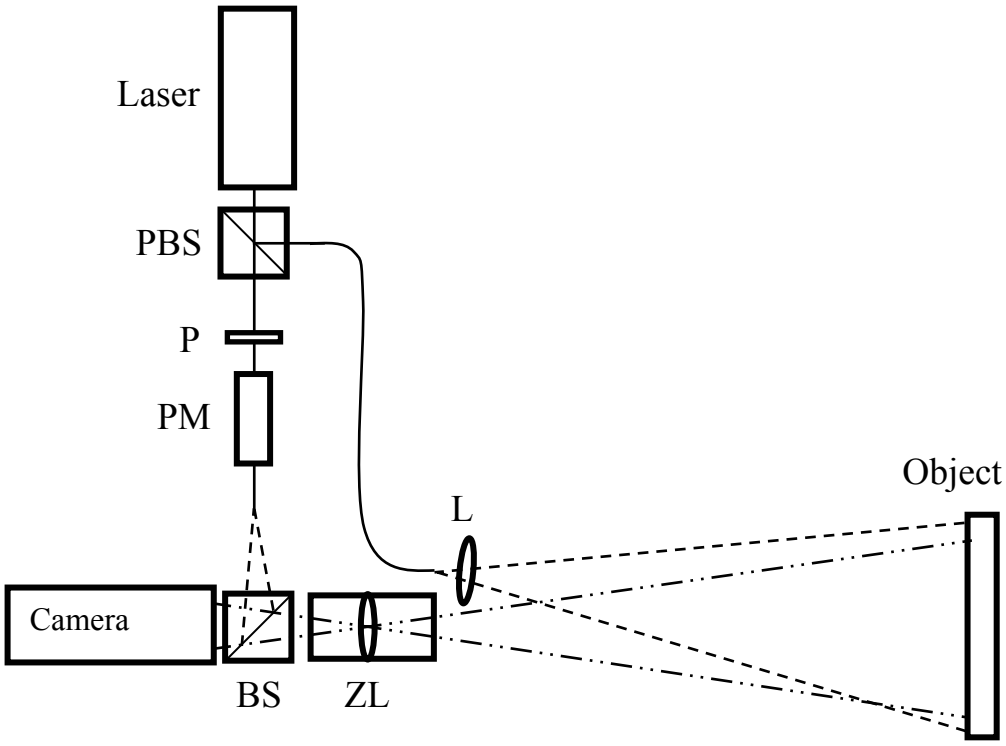

Figure 2.2 Schematic of out-of-plane SPI setup. PBS – Polarising beamsplitter; P – Polariser; PM – Phase modulator; BS – Beam combiner; ZL – Zoom lens; L1 – Beam expanding lens

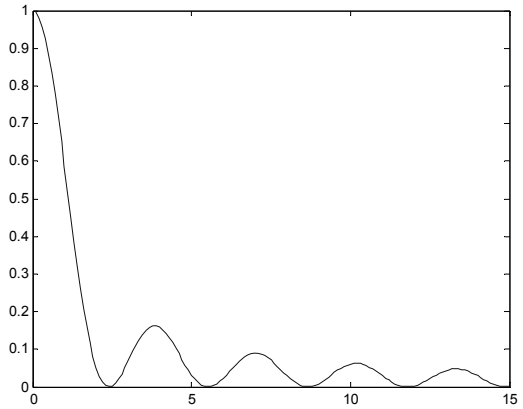

Figure 2.3 The function $J_0^2(\eta)$

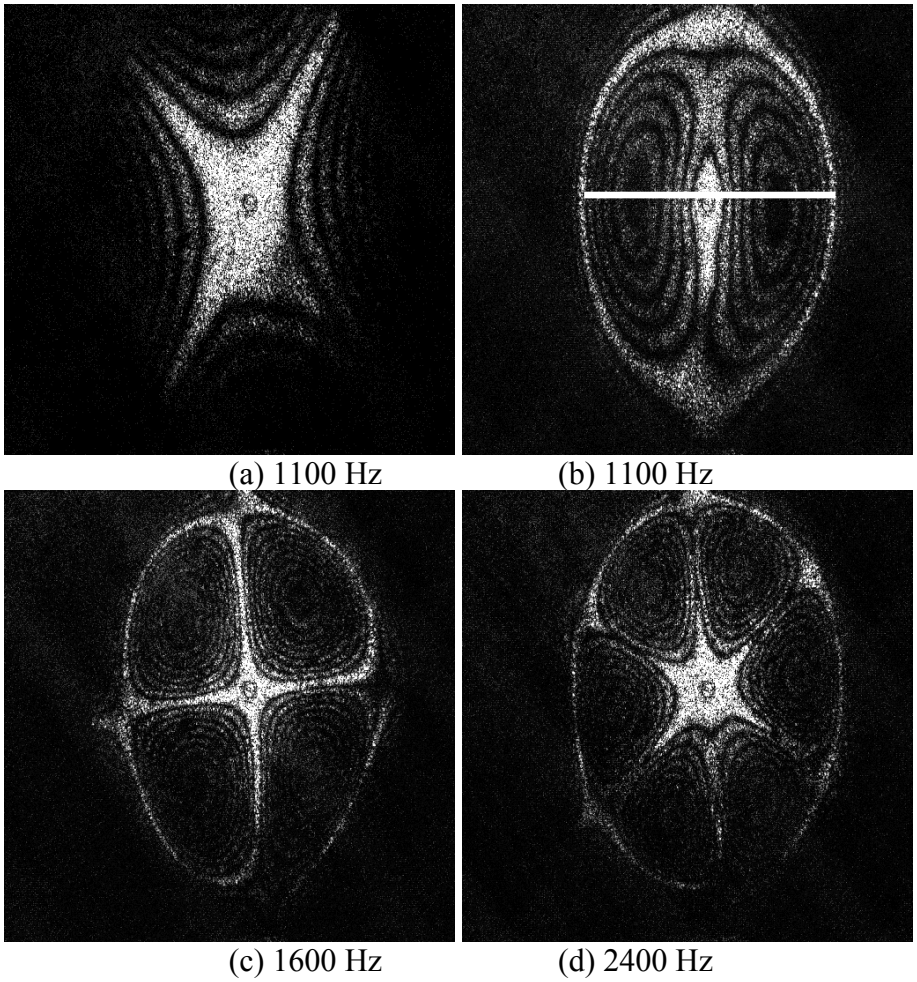

(a) 1100 Hz (b) 1100 Hz

(c) 1600 Hz (d) 2400 Hz

Figure 2.4 Time-averaged subtraction fringe patterns for a circular disk vibrating at different natural frequencies. Line in (b) denotes position of section for Figure 2.5

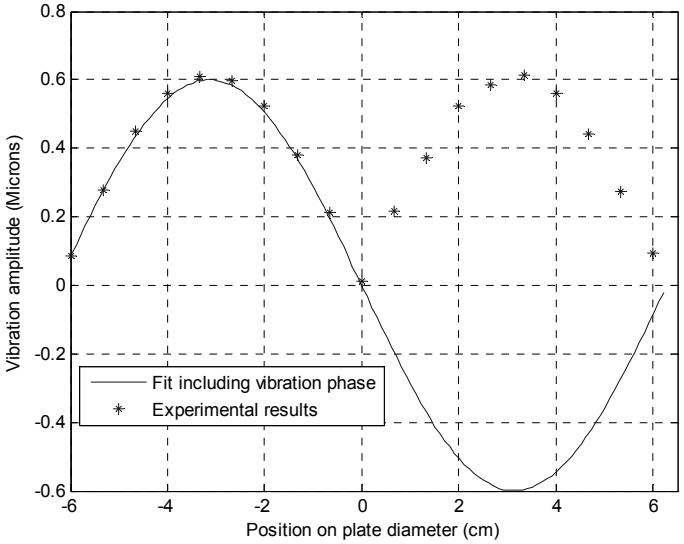

Figure 2.5 Vibration amplitude of a cross-section of the vibrating plate of Figure 2.4.

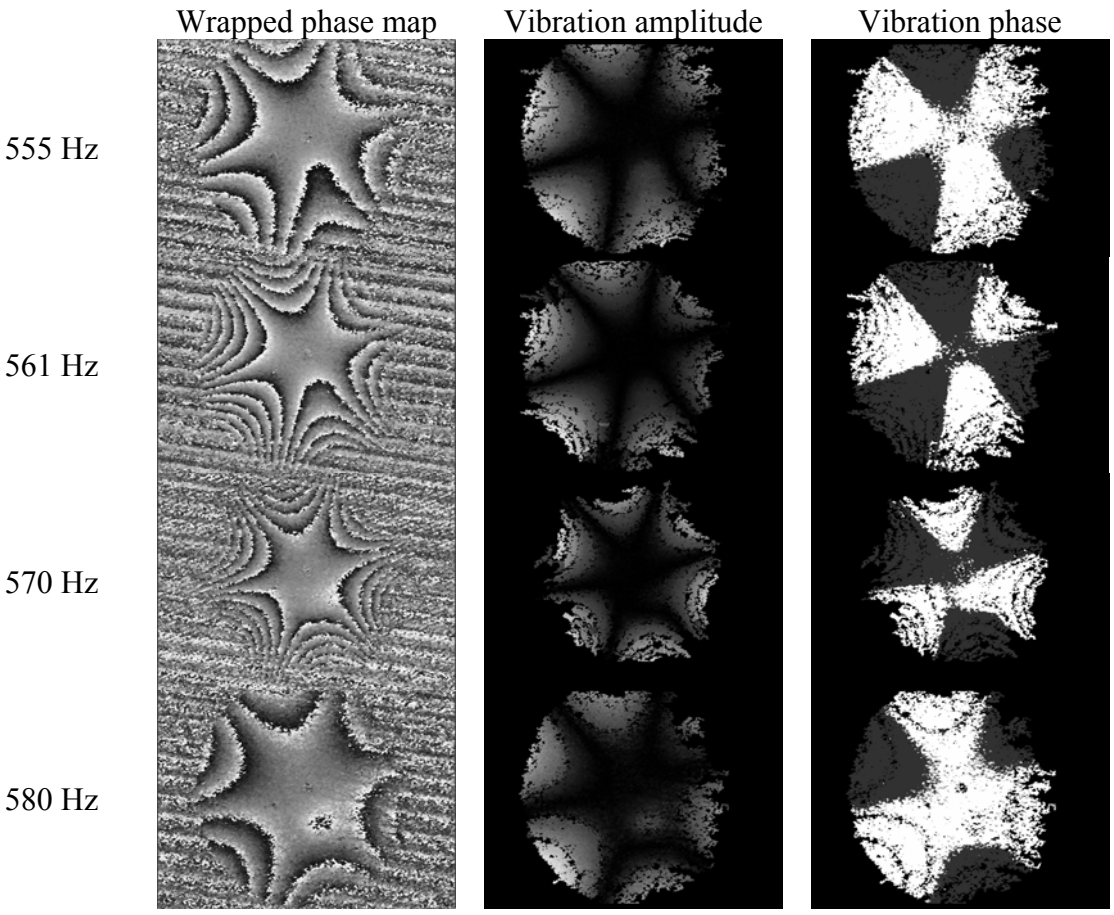

Figure 2.6 Experimental results for a stroboscopic sequence of excitation frequencies that span a natural frequency of the object.

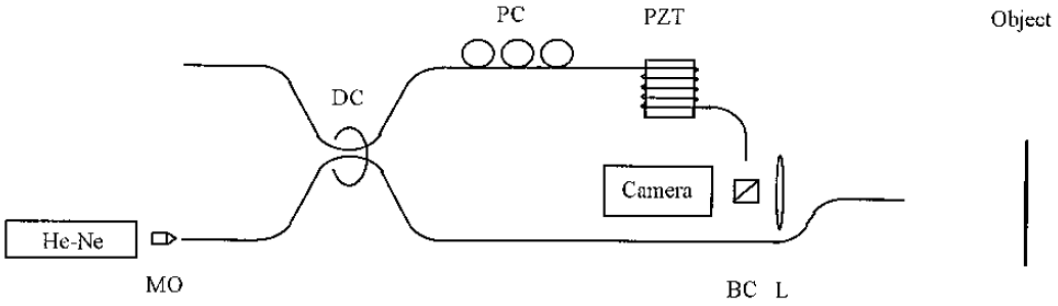

Figure 2.7 Schematic of the first high-speed fibre-optic SPI arrangement.[44]

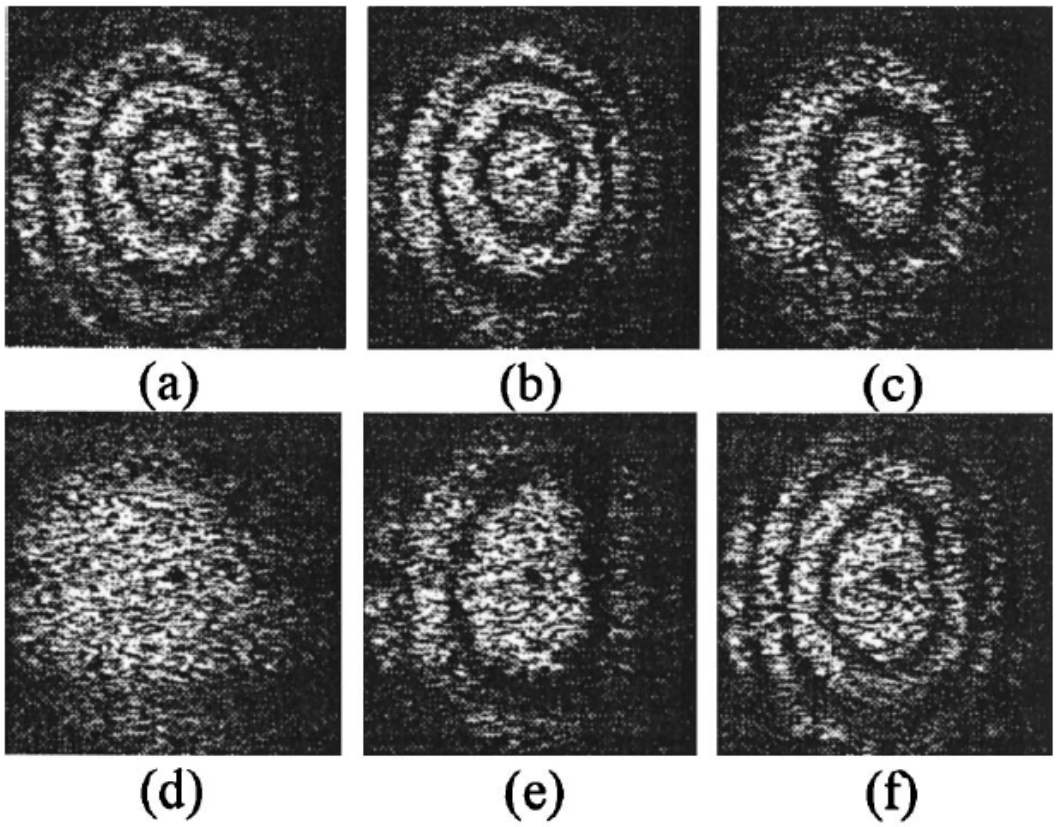

Figure 2.8 Temporally resolved vibration fringes for a circular test plate vibrating at 198 Hz.

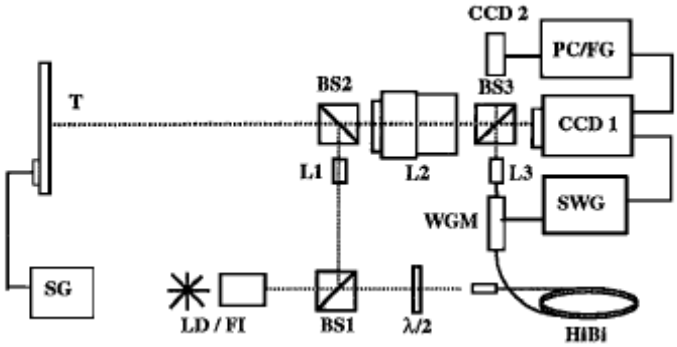

Figure 2.9 Schematic of a high-speed inter-frame phase-stepped SPI. SG – Signal generator; T- Target; LD/FI – Laser diode and Faraday isolator; BS1, BS2, BS3 – 50/50 nonpolarizing beamsplitters; L1, L3 – Cylindrical lenses; L2 – Zoom lens; CCD1 – High-speed line-scan camera; CCD2 – Auxiliary array detector; λ/2 – Half waveplate; HiBi – Optical fibre; WGM – Waveguide phase modulator; SWG – Staircase waveform generator.

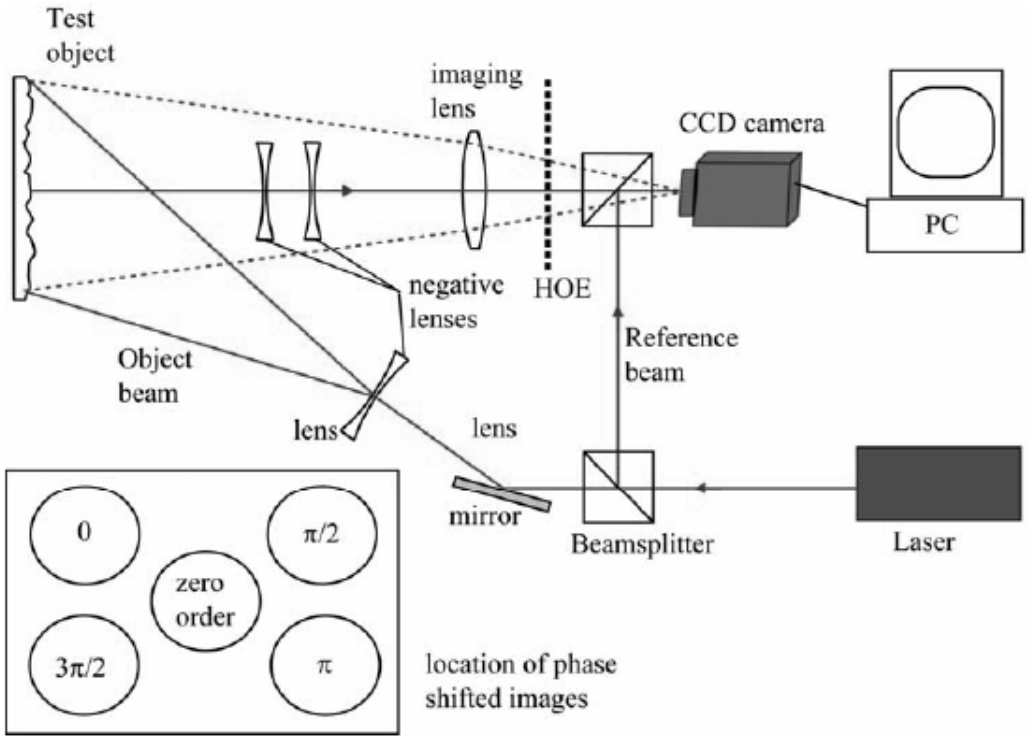

Figure 2.10 Schematic of the spatial phase stepping SPI system based on a HOE developed by Barrientos Garcia *et al.*[71, 72] The four phase stepped images on the CCD are shown. The central image corresponds to the zero order that was not used in the phase calculation.

3

Surface Velocity Limit of High-speed Phase-stepped SPI

An inter-frame phase-stepped SPI system based on a high-speed CMOS camera was constructed. A numerical and analytical error analysis for the system was performed in order to determine the maximum surface velocity that could be reliably measured with inter-frame phase stepping. The flexibility of the CMOS detector readout was used to identify regions of interest with full-field time-averaged measurements and then to interrogate those regions with time-resolved measurements sampled at up to 70 kHz.

3.1 Experimental system for initial experiments

The experimental system on which the work of this thesis is based was initially developed using the experience of the two high-speed systems which had already been at Heriot-Watt University, as reviewed in Section 2.5.3 (Figure 2.7 from reference 44 and Figure 2.9 from reference 47). Several improvements over these previous sytems were incorporated:

- A CMOS camera permitting random pixel access and therefore any region of interest on the object to be selected (instead of separate high-speed line-scan detector and low speed full-field array detector).
- A more powerful laser source for larger area illumination at high speed.

- A compact interferometer design which would help align the optics to combine reference beam and object beam more easily and accurately.
- An electro-optic phase modulator which could provide higher modulation bandwidth.
- A polarizing beam-splitter (PBS) which could provide variable ratio of reference beam and object beam.

A schematic of the system was shown in Figure 2.2. Figure 3.1 shows a photo of the experimental setup. The output from a diode-pumped, frequency doubled Nd:YVO4 laser (single-frequency CW output at 532 nm at power levels up to 5W) was divided by a polarizing beams-splitter (PBS) into orthogonally linearly polarized object and reference beams.

Each beam was then launched into the fast axis of separate highly birefringent optical fibres. The output power of the laser was restricted to 500 mW so as not to damage the proximal fibre ends, particularly of the object beam fibre. The beam to be launched was focused to form a waist on the fibre core, so that the spot and core sizes were closely matched. The beam-splitter (PBS) and fibre-launches could be rotated together as a unit about the axis of the laser beam in order to vary the intensity ratio between the object and reference beams. Typically, 60% of the laser's output was launched in the object beam fibre. Bulk optics were bought for using with the laser when operating in the range 500 mW to 5 W, but were not used during the course of the PhD.

Light from the object fibre illuminated the test object directly, or through a cylindrical lens (L), depending on the surface area under test. The distal end of the object fibre was rotated by 90° about its optical axis in order to align its fast axis (and hence the linear polarization of the emerging light) with that of the reference fibre. The test object was a centrally pinned 14-cm-diameter circular aluminum plate with retro-reflective coating, driven by a piezoelectric element attached to its rear face. The object was imaged by a photographic zoom lens (ZL) on to the 1024×1024 element array of a CMOS camera (Photonfocus, MV-D1024, 8-bit resolution). Note that a Kodak 4540 high-speed CCD camera is shown in Figure 3.1. Due to the pixel sensor architecture, the physical characteristics of the CMOS camera permit random pixel access. Therefore any region on the object could be easily picked up, and lowering the spatial resolution would allow a higher temporal resolution as seen in Table 3.1. Recorded images were transferred to a computer at up to 70,000 frames per second via a Camera Link interface.

Region of interest size (Pixels)	Maximum frame rate (Frames per second)
1024 ×1024	74
512 ×512	293
256 ×256	1,100
128 ×128	4,100
128 ×16	23,000
128 ×1	70,000

Table 3.1 Maximum camera frame rate for different sized regions of interest for the CMOS camera

Light from the reference fibre was collimated, passed through an electro-optic phase modulator (PM) and was then re-launched in to more optical fibre to path match the object beam. The phase modulator generates a phase step by utilizing the fact that the refractive index of the electro-optic material depends on the electric field applied to it. Up to 20 GHz modulation bandwidths have been reported, so it is suitable for high-speed measurement. A camera frame synchronization signal was passed from the PC controlling the CMOS camera to a staircase waveform generator (SWG) that generated a staircase voltage with N equal steps, each step synchronized to the camera frame rate. When the CMOS camera started recording, a signal at the start of each frame was sent to the SWG. The SWG then converted the frame pulses into a staircase voltage, which was passed to the phase modulator amplifier to produce inter-frame phase steps in the reference beam. The gain of the SWG was adjusted to produce phase steps of $\pi/2$ radians in the reference beam during the blanking period between frames. The phase step size was calibrated using the procedure described later in this section. The SWG was originally made for the system reported in in reference 47, Figure 2.9. For the CMOS system reported in this thesis, the SWG was modified slightly to incorporate a variable delay between the incoming frame signal and the output staircase waveform. This modification will be discussed later this section.

Light emerging from the reference fibre was directed to the combining beamsplitter (BS) inside the compact interferometer, as shown in Figure 3.1(b), the reflected component of which provided a diverging on-axis reference beam on the CMOS camera. The beamsplitter sat on a small block inside the compact interferometer head which could rotate (tilt control was unnecessary due to the fabrication tolerances for the head). The compact interferometer could be screwed directly on to any camera. The reference

beam fibre connected directly to the compact interferometer with a FC-type fibre connector. Similarly, the object fibre was mounted on to the top of the compact interferometer as shown in Figure 3.1 (a) to provide on-axis illumination.

Initial experiments revealed that the intensity of the reference beam fluctuated considerably when different voltages were applied to the phase modulator. Figure 3.2(a) shows the mean intensity in an image of the reference beam only recorded for a sequence of frames with an applied staircase voltage. The error bars show plus and minus three standard deviations about the mean for each image. This intensity fluctuation was attributed to leakage of an orthogonally polarized component from the polarizing beamsplitter PBS propagating in the slow axis of the reference fibre. A linear polarizer (P) was inserted in the collimated output from the fibre before the phase modulator (shown in Figure 2.2 but not visible in the photograph of Figure 3.1) in order to eliminate the leaked component of the object beam. The collimated beam was aligned carefully to the optic axis of the phase modulator and fluctuations in the intensity of the reference beam during phase stepping were reduced to less than 1%, Figure 3.2(b).

Due to delays introduced by the electronics of the SWG and the phase modulator amplifier, the applied phase step might not occur exactly during the period between frames. Therefore the position of the phase step with respect to the camera frame signal was validated by measuring the interference modulation amplitude introduced by the phase steps, calculated at each pixel using the equation:

$$VI(x,y,t_n) = \frac{\left\{\left[\left(I_n - I_{n+1}\right) + \left(I_{n-1} - I_{n+2}\right)\right]^2 + \left[\left(I_n + I_{n+1}\right) - \left(I_{n-1} + I_{n+2}\right)\right]^2\right\}^{1/2}}{2\sqrt{2}} \qquad \textbf{(3-1)}$$

The modulation amplitude is a maximum when the phase steps occurred in the period between exposures, and a minimum when the steps occur mid-exposure. Figure 3.3 shows the variation in measured mean modulation amplitude (calculated over all pixels modulating at greater than 5% of the maximum theoretical value) plotted against a variable delay between the camera synchronization signal and the SWG phase steps. The delay is expressed as a fraction of the camera frame period, t_s. Due to signal delays in the SWG and the phase modulator drive electronics, the maximum modulation amplitude does not necessarily occur when the step signal is in phase with the camera

frame signal. All results were captured with the computer-generated delay chosen to produce the maximum modulation.

The SWG gain was adjusted to produce phase steps of π/2 radians in the reference beam by calculating the phase step size at each pixel using the equation:

$$\Phi_R(x,y,t_n) = 2\tan^{-1}\frac{3(I_n - I_{n+1}) - (I_{n-1} - I_{n+2})}{(I_n - I_{n+1}) + (I_{n-1} - I_{n+2})} \quad \textbf{(3-2)}$$

Figure 3.4 (a) shows the variation in mean phase step size (calculated over all pixels modulating at greater than 5% of the maximum theoretical modulation) for a sequence of phase-stepped frames recorded with the test object stationary. The error bars show plus and minus one standard deviation about the mean. Over all frames in the sequence, a mean phase step of 90.20° with a standard deviation of 9.85° was obtained, Figure 3.4(b). The periodic nature of the phase fluctuation is emphasized by using a different symbol for every fourth point. This phase fluctuation is discussed further in Section 3.4, and is characteristic of a miscalibration in the staircase voltage applied. In our current arrangement, the adjustment of the SWG voltage was too coarse to enable this small error to be eliminated entirely. The phase difference calculated between successive frames is given by,

$$\Phi_O(x,y,t_n) - \Phi_R(x,y,t_n) - \left[\Phi_O(x,y,t_{n-1}) - \Phi_R(x,y,t_{n-1})\right] = \Delta\Phi_O(x,y,t_n) + \frac{\pi}{2} \quad \textbf{(3-3)}$$

where at a given pixel $\Delta\Phi_O(t_n) = \Phi_O(t_n) - \Phi_O(t_{n-1})$ represents the change in phase due to the surface deformation between frames and $\frac{\pi}{2} = \Phi_R(t_n) - \Phi_R(t_{n-1})$ is the change in the reference beam phase between frames, i.e the applied phase step. Figure 3.4(c) shows the mean phase difference between successive frames (calculated over all pixels modulating at greater than 5% of the maximum theoretical modulation) for the same sequence of phase-stepped frames recorded with the test object stationary. Over the whole sequence, a mean phase difference of -0.002° with a standard deviation of 3.06° was obtained, Figure 3.4 (d).

3.2 Vibration measurement

Figure 3.5 shows a time-averaged fringe pattern recorded with the CMOS camera working at 70 frames per second (1024 × 1024 pixels) for the circular test target vibrating at a natural frequency at 250 Hz. The time-averaged fringe pattern was used to identify two ROIs for time-resolved measurements with the same CMOS detector, marked in Figure 3.5. The cylindrical lens L1 was inserted into the object beam using a connectorized mount on the end of the object fibre in order to illuminate the two ROIs.

For the horizontal line across the vertical vibration node, the maximum vibration amplitude was estimated from the Bessel fringe order to be 0.7 μm, corresponding to a maximum surface velocity of 1.1 mm/s. The relative vibration phase between points on the line is not measured directly from the time-averaged measurement, although it can be inferred for this simple test target.

Figure 3.6 shows a composite spatiotemporal phase-stepped speckle interferogram, with each row corresponding to a single frame of 128 × 1 pixels transferred to the PC at 33 kHz frame rate. The phase at each pixel was calculated from the recorded intensity from four consecutive frames using equation (2-23). As discussed in section 2.5.3, it is assumed that the interferogram at each pixel is sampled within the Nyquist limit, i.e. there are at least two samples per fringe period. The Nyquist condition imposes a maximum phase change of $\pm\pi$ in Φ_O between any two frames, corresponding to a velocity limit of:

$$v_{Nyq} = \pm\frac{\lambda}{2\eta t_s} \qquad \textbf{(3-4)}$$

where η is the interferometer sensitivity factor (equal to 2 for the out-of-plane configuration used throughout this thesis). Note that v_{Nyq} is the maximum velocity imposed by the sampling limit assuming that the full bandwidth of the detector is available for deformation measurement. The velocity limit with phase stepping, $v_{Nyq,PS}$ in equation (2-25), was introduced in reference 47. For the subsequent error analysis, and the spatial phase stepping analysis of Chapter 4, it is more convenient to use v_{Nyq}. The relation between v_{Nyq} and $v_{Nyq,PS}$ is discussed in Section 3.3. The phase difference

between adjacent rows is wrapped into the range -π to π radians and the surface velocity is calculated from the relation:

$$w'(x,y,t_n) = \frac{\lambda}{2\pi\eta t_s}\Delta\Phi_O(x,y,t_n) \quad \textbf{(3-5)}$$

Rearranging equation (3-5) yields:

$$\frac{w'(x,y,t_n)}{|v_{Nyq}|} = \frac{\Delta\Phi_O(x,y,t_n)}{\pi} \quad \textbf{(3-6)}$$

i.e. the surface velocity normalized by the magnitude of the Nyquist velocity limit. It can be seen from equation (3-4) that for a given wavelength and interferometer sensitivity, the Nyquist velocity limit is determined by the camera frame rate. Normalizing the surface velocity in this way gives an immediate indication of the interferometer performance without needing to refer back continuously to equation (3-4).

A further numerical difference between adjacent rows of phase differences can be calculated, and the surface acceleration calculated from the relation:

$$w''(x,y,t_n) = \frac{\lambda}{2\pi\eta t_s^2}\Delta^2\Phi_O(x,y,t_n) \quad \textbf{(3-7)}$$

where at a given pixel $\Delta^2\Phi_O(t_n) = \Delta\Phi_O(t_{n+1}) - \Delta\Phi_O(t_n)$ represents the rate of change in phase difference between frames. Rearranging equation (3-7) yields:

$$\frac{w''(x,y,t_n)}{2\pi f|v_{Nyq}|} = \frac{1}{2\pi^2 f t_s}\Delta^2\Phi_O(x,y,t_n) \quad \textbf{(3-8)}$$

i.e. the surface acceleration normalized to the magnitude of the maximum acceleration present for harmonic vibration at the Nyquist velocity limit. For harmonic vibration, the normalized velocity of equation (3-6) and the normalized acceleration of equation (3-8) lie between the same limits. Figure 3.7(b) shows the measured normalized surface acceleration, $\Delta^2\Phi_O / 2\pi^2 f t_s$, for the horizontal ROI.

A similar analysis was performed for the vertical ROI positioned across a horizontal vibration node indicated in Figure 3.5. The maximum vibration amplitude was estimated from the Bessel fringe order to be 0.16 μm, corresponding to a maximum surface velocity of 0.25 mm/s. Single frames of 16 × 64 pixels were transferred to the PC at 10 kHz frame rate. A composite spatiotemporal phase-stepped speckle interferogram, with each row corresponding to one 1 × 64 pixel column from the ROI, was analyzed as described above. Figure 3.7(c) and (d) show the normalized velocity and normalized acceleration respectively.

3.3 Error analysis for inter-frame phase-stepped SPI

The introduction of an inter-frame phase step reduces the measurement range because the cumulative phase change associated with the argument of the cosine term in equation (2-22) must be sampled at twice per fringe (at least) to fulfil the Nyquist condition. From equation (2-25) the phase step can be considered to introduce a pseudo velocity of $v_{PS} = \lambda/(\eta t_s N)$. The upper and lower velocity limits correspond to the sense of the surface displacement relative to the phase step imposed on the reference beam. Unless the surface displacement is unidirectional and of known sense, the lower magnitude value of $v_{Nyq,PS}$ (corresponding to the surface velocity and v_{PS} occurring in the same sense) sets the practical velocity limit. The corresponding minimum and maximum surface velocities are given by:

$$\begin{aligned} v_{\min} &= -v_{PS} \\ v_{\max} = v_{Nyq,PS} &= v_{Nyq} - v_{PS} \end{aligned} \qquad \textbf{(3-9)}$$

Hence the velocity measurement range is maximized when $v_{PS} = \pi/2$ radians, corresponding to N=4.

However, it is clear that these bounds do not set the practical velocity measurement limit for inter-frame phase stepped SPI. Firstly $v_{\min}$ corresponds to zero cumulative phase change between frames and $v_{\max}$ corresponds to a phase change of π radians per frame i.e. two interference fringe periods for N=4 sequential measurements, for which the phase calculated by equation (2-23) will be significantly in error. Furthermore, inter-frame phase stepping assumes that surface velocity (and hence interference phase change) can be approximated as linear during the N sequential measurements. Therefore, even before the $v_{\min}$ and $v_{\max}$ bounds are reached, measurement errors

depend on the surface velocity and acceleration (i.e. frequency and amplitude of vibration) and the camera frame rate, and cannot be determined without a priori knowledge of the vibration to be measured. To model the effects of surface velocity, surface acceleration and camera frame rate on measurement accuracy, a 256 × 1 pixel fringe pattern was generated using equation (2-22). Two phase distributions were considered. The first phase distribution was similar to the horizontal ROI of Figure 3.5 and represented a central node and two regions vibrating harmonically out-of-phase, and was calculated using the expression:

$$\Phi_O(x,t_n) = \frac{2\pi\eta}{\lambda} w_0 \sin(2\pi f t_n)\sin(2\pi x) + 2\pi x \qquad \textbf{(3-10)}$$

where $0<x<1$, $\Omega = 2\pi f$, f is the object vibration frequency and I=127.5 and V=1 in equation (2-22). The vibration amplitude was defined in terms of the maximum normalized surface velocity for a given interferometer arrangement (λ, η and t_s, defining v_{Nyq}) and vibration frequency (f):

$$w_0 = \left(\frac{v_{\max}}{|v_{Nyq}|}\right)\frac{|v_{Nyq}|}{2\pi f} \qquad \textbf{(3-11)}$$

where $-0.5 \le (v_{max}/|v_{Nyq}|) \le 0.5$ for the Nyquist condition to be met.

A composite spatiotemporal image was constructed by calculating the intensity for $0 < t_n < 2/(ft_s)$, i.e. the number of rows required for two vibration periods at the chosen frequency. The surface velocity at each t_n was also calculated, and used to calculate the reduction in fringe visibility for an exposure of $t_e=0.1t_s$.

The second phase distribution studied represented a uniform surface motion at constant velocity, given by,

$$\Phi_O(x,t_n) = \pi\left(\frac{v_{\max}}{|v_{Nyq}|}\right)\frac{t_n}{t_s} + 2\pi x \qquad \textbf{(3-12)}$$

The second term in both (3-10) and (3-12) represents an arbitrary starting phase in the range 0 to 2π radians, varying linearly with position. A uniform phase step of $\Phi_R(t_n)=(t_n/t_s)(\pi/2)$ was applied in both cases.

The normalized velocity was calculated from the simulated interferograms using the procedure described in the previous section. The maximum error between the calculated normalized velocity and the value used to calculate the phase distribution is shown in Figure 3.8(a) for a range of normalized velocities. The equivalent phase error is also shown on the second vertical axis. It is the maximum error (that occurs at the maximum surface velocity) that is of interest, rather than the root mean square error over the whole vibration period. The linear phase change introduced in the case of constant surface velocity is akin to a linear miscalibration of the phase modulator. Carré's algorithm, equation (2-23), is relatively insensitive to this type of phase step error and the velocity error is small for $-0.45 \leq (v_{max}/|v_{Nyq}|) \leq 0.45$, (a). For the case of harmonic vibration, an error in the recovered velocity arises due to the non-linear surface motion during the four frames used for phase stepping. The non-linearity is not significant for a large number of frames per vibration period, e.g. $1/(ft_s)=1000$. However, the velocity error increases as the number of frames per vibration period falls, e.g. $1/(ft_s)=100$ and 10 in Figure 3.8(a).

The effect of non-linear surface motion on the recovered surface velocity can be modelled. In the presence of a non-linear phase step error, the actual phase step, α', is given by:

$$\alpha' = \alpha(1+\varepsilon\alpha) \qquad \textbf{(3-13)}$$

where α is the desired phase step and ε is a constant. Equation (3-8) gives the phase change due to surface acceleration, from which the phase step between frames (ignoring any linear component) is given by:

$$\alpha' = \frac{\pi}{2} + 2\pi^2 ft_s\left(\frac{v_{max}}{|v_{Nyq}|}\right) = \frac{\pi}{2}\left\{1 + 8\,ft_s\left(\frac{v_{max}}{|v_{Nyq}|}\right)\frac{\pi}{2}\right\} \qquad \textbf{(3-14)}$$

It is well known that phase step errors produce a periodic phase error at twice the frequency of the fringe pattern[82]. A mean phase error dominates the periodic term, although it is usually ignored in full-field interferometry because it is removed by spatial phase unwrapping. However, the mean phase error will be interpreted as a velocity error in inter-frame phase stepping. The maximum normalized velocity error, based on this mean phase error, is given by:

$$\frac{\Delta\phi}{\pi} = \frac{1}{\pi}\tan^{-1}\frac{1}{N}\sum_{n=1}^{N}\varepsilon\alpha^2 = \frac{1}{\pi}\tan^{-1}\left\{3\pi^2 ft_s\left(\frac{v_{\max}}{|v_{Nyq}|}\right)\right\} \quad \textbf{(3-15)}$$

Equation (3-15) is plotted in Figure 3.8(a) for the three values of ft_s considered, and shows good agreement with the points obtained from the simulation.

Figure 3.8(b) shows the maximum normalized velocity error plotted against maximum normalized surface velocity using the well known four-frame phase step algorithm to recover the phase[83]:

$$\Phi_O(x,y,t_n) - \Phi_R(x,y,t_n) = \tan^{-1}\frac{-(I_n - I_{n+2})}{(I_{n-1} + I_{n+1})} \quad \textbf{(3-16)}$$

This algorithm is sensitive to linear miscalibration phase step errors, and Figure 3.8(b) shows that the linear component of surface velocity produces the same error in the simulation irrespective of the number of frames per period of vibration.

The effect of linear surface motion on the recovered surface velocity can also be modelled using the mean phase step error. In the presence of a linear phase step error, the actual phase step, α', is given by:

$$\alpha' = \alpha(1+\varepsilon) \quad \textbf{(3-17)}$$

where ε is a constant. Equation (3-6) gives the phase change due to surface velocity, from which the phase step between frames (ignoring any non-linear component) is given by:

$$\alpha' = \frac{\pi}{2} + \pi\left(\frac{v_{\max}}{|v_{Nyq}|}\right) = \frac{\pi}{2}\left\{1 + 2\left(\frac{v_{\max}}{|v_{Nyq}|}\right)\right\} \quad \textbf{(3-18)}$$

The maximum normalized velocity error is approximated by:

$$\frac{\Delta\phi}{\pi} = \frac{1}{\pi}\tan^{-1}\frac{1}{N}\sum_{n=1}^{N}\varepsilon\alpha = \frac{1}{\pi}\tan^{-1}\left\{\frac{3}{2}\pi\left(\frac{v_{\max}}{v_{Nyq}}\right)\right\} \quad \textbf{(3-19)}$$

which is independent of ft_s as expected from the simulation. Equation (3-19) is plotted in Figure 3.8(b) and shows good agreement with the points obtained from the simulation. This four frame algorithm is not considered further.

Figure 3.8(c) shows the maximum normalized velocity error plotted against maximum normalized surface velocity using the well known five-frame phase step algorithm to recover the phase:

$$\Phi_O(x,y,t_n) - \Phi_R(x,y,t_n) = \tan^{-1}\frac{2(I_{n-1} + I_{n+1})}{(2I_n - I_{n-2} - I_{n+2})} \quad \textbf{(3-20)}$$

The figure shows that the algorithm is insensitive to linear miscalibration errors for a very restricted surface velocity range of $-0.05 \le (v_{max}/|v_{Nyq}|) \le 0.05$. Beyond that, the algorithm is sensitive to linear miscalibration errors, although slightly less so than the four-frame algorithm of equation (3-16). The simulation shows that the error does not vary significantly with the number of frames per vibration period, because it is due to the constant velocity component. A theoretical line based on 0.5 times the error due to the four-frame algorithm, equation (3-16), has been plotted.

Figure 3.9 shows the maximum normalized velocity error plotted against the number of frames per surface vibration period for the harmonic vibration. For Carré's algorithm, Figure 3.9(a) shows that the maximum error from the simulation and the value predicted theoretically by equation (3-19) agree well for $v_{max}/|v_{Nyq}| \le 0.3$.The surface non-linearity due to acceleration, and therefore the maximum normalized surface velocity, decrease as the number of frames per vibration period increases. For the five frame algorithm, Figure 3.9(b) shows that the maximum normalized velocity error is independent of the number of frames per vibration period. There is a small range of

frames per vibration period for $v_{max}/|vN_{yq}| \geq 0.3$ at which it gives lower errors than Carré algorithm. However, for general anharmonic testing where a range of frequencies are present, the errors at low frequencies would quickly outweigh this advantage. We currently restrict analysis to $v_{max}/|vN_{yq}| \leq 0.3$ using Carré's algorithm, but two-stage processing that switches between the two algorithms depending on the surface velocity recovered in the first stage is a future possibility.

Figure 3.10 shows the effect of intensity noise on the maximum normalized velocity error obtained with Carré's and the five-frame algorithms. Zero-mean, Gaussian-distributed noise up to a maximum of 3 bits (7 grey levels) was added to the calculated speckle interferograms prior to phase calculation. Intensity values less than or greater than the limiting values (0 and 255 grey levels) were set to the respective limit. For the camera used, the intensity noise was measured as 2 bits (3 grey levels). For Carré's method, Figure 3.10(a) shows that the maximum normalized velocity error does not decrease continuously with increasing number of frames per vibration period (although the standard deviation does). The five-frame method is more robust against high levels of intensity noise than Carré's algorithm, although neither the maximum normalized velocity error, Figure 3.10(b), nor its standard deviation decrease with increasing numbers of frames per vibration period. For the levels of intensity noise encountered with a scientific-quality CMOS camera, Carré's algorithm is preferred.

The analysis for Figure 3.8-Figure 3.10 assumed that a continuous, incremental phase step, $\Phi_R(t_n)=(t_n/t_s)(\pi/2)$, was applied. Known continuous, incremental phase steps of size $(1+\varepsilon)\pi/2$, equation (3-17), cause the measurement range to be reduced, as discussed at the beginning of this section, but introduce no significant error with Carré's algorithm. If the actual phase step size is not known, then a systematic normalized velocity offset error of $\varepsilon/2$ arises. However, it is convenient to drive the phase modulator with a staircase waveform generator (SWG) so that the voltage does not increase without limit. In this case, the incremental phase steps of $(1+\varepsilon)\pi/2$ apply to the first three frames, but the fourth step is $(1-3\varepsilon)\pi/2$ as the voltage returns to its start value. Figure 3.11(a) shows the calculated normalized velocity error from the simulation with this staircase-type phase step error (i.e. phase steps of 86). The form of the phase error matches that seen in the experimental data in Figure 3.4(c). The normalized velocity error for constant surface velocity is non-zero for $v_{max}/|v_{Nyq}| = 0$ and increases asymmetrically for positive and negative normalized surface velocity. Figure 3.11(b) shows the effect of staircase-type phase error for three different phase step sizes. The corresponding errors for a

staircase phase step of 90° to 94° for three phase steps produce smaller errors than for range 86° to 90° plotted. Improvements to our experimental system should enable this type of error to be reduced further. Alternatively, a phase step algorithm using the calibrated size of the individual phase steps could be implemented.

3.4 Discussion

The experimental results demonstrated the flexibility of the CMOS detector to record time-averaged subtraction fringes, from which ROIs were identified for temporally-resolved measurements. Unlike earlier systems[44, 47], there was no need to change between detectors to make the two types of measurement, and it was straightforward to identify the corresponding position of the ROIs on the time-averaged subtraction fringe pattern. It was equally straightforward to change the orientation of the ROI, which previously would have required the object or interferometer to be rotated, or further optical components to be incorporated. Inter-frame phase stepping was applied to implement the first quantitative analysis with SPI using a CMOS camera. Surface acceleration plots were presented for the first time with high-speed SPI. For the experimental plots, exposures of t_e=10 μs were used, corresponding to t_e/t_s=0.33 and 0.1 for the horizontal and vertical ROIs respectively. An exposure of t_e/t_s=0.1 was used for all the numerical simulations. Figure 3.12 shows that the errors in maximum normalized velocity are substantial when an exposure of t_e/t_s=1 is used, but that there is little practical difference between t_e/t_s=0.1 and t_e/t_s=0.01.

The particular CMOS camera used can be programmed to enable up to 70 ROIs of minimum length 4 pixels to be defined, all aligned vertically. Future models will apparently have the vertical alignment requirement of the ROIs removed. In our current implementation, the ROIs are limited to 16 pixels wide by the Camera Link software (as used for the vertical ROI). The software also currently imposes a frame rate limit of 70 kHz for a 256 × 1 pixel ROI, i.e. 17.9 Mpixels/s, which is below the 40 Mpixel s^{-1} maximum rate of the camera. Even without achieving the full camera bandwidth, it should be possible to obtain MHz frame rates for 4 × 1 pixel ROIs in future

implementations. A lower overall bandwidth was used for the experimental results presented (128 × 1 pixel at 33 kHz or 4.2 Mpixel s^{-1}).

The normalized velocity error plots against surface velocity, Figure 3.8, and number of frames per vibration period, Figure 3.9 show the first systematic error analysis for the high-speed SPI acting as a multipoint vibrometer. The numerical simulation and theoretical evaluation of these errors were found to be in good agreement. It provides the possibility to set a vibration velocity and frequency limit for the maximum camera frame rate in order to restrict errors to within a certain threshold.

We use $v_{max}/|v_{Nyq}| \leq 0.3$ and Carré's algorithm to maintain optimum operation over the largest frequency range. As mentioned earlier, there is scope for a two-pass processing strategy where the five-frame algorithm is used to reduce the errors slightly at small numbers of frames per period. However, these errors are relatively large, and could be avoided entirely by the use of spatial phase stepping at the expense of increased experimental complexity.

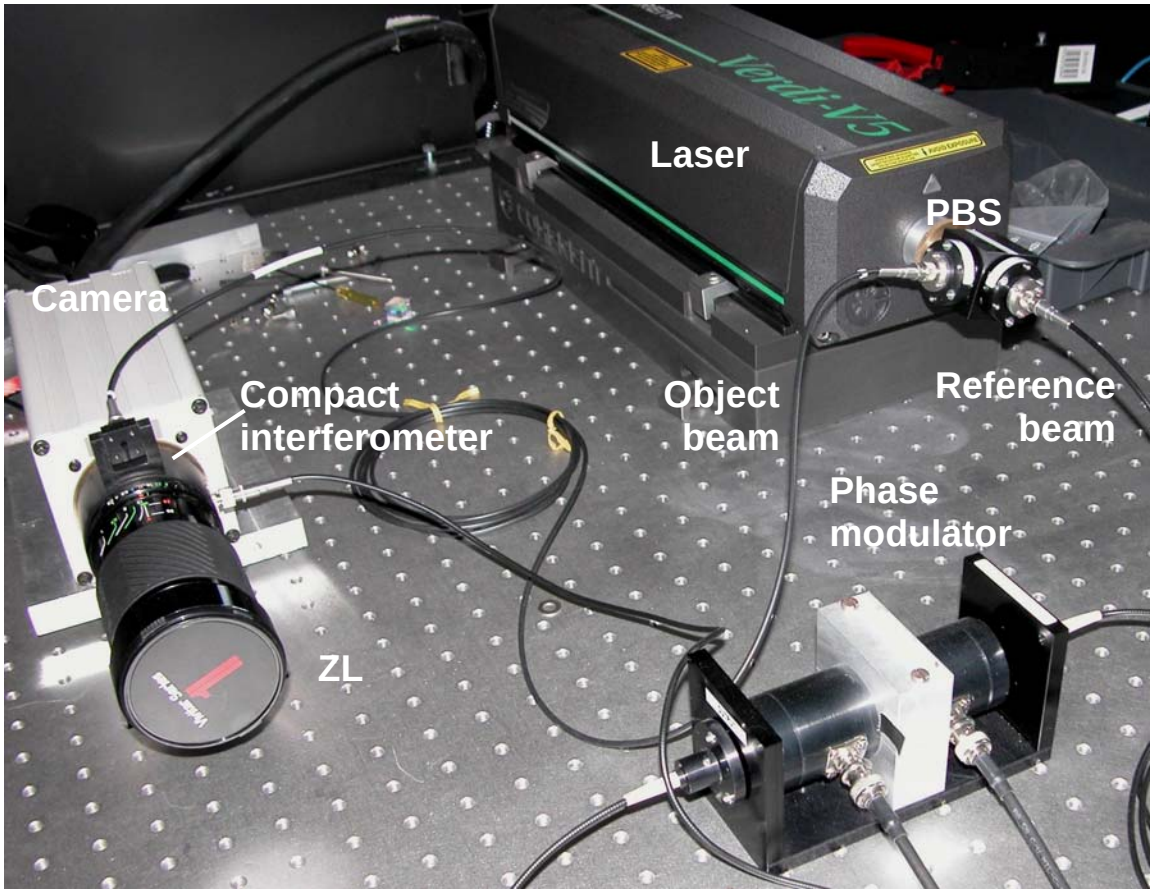

(a)

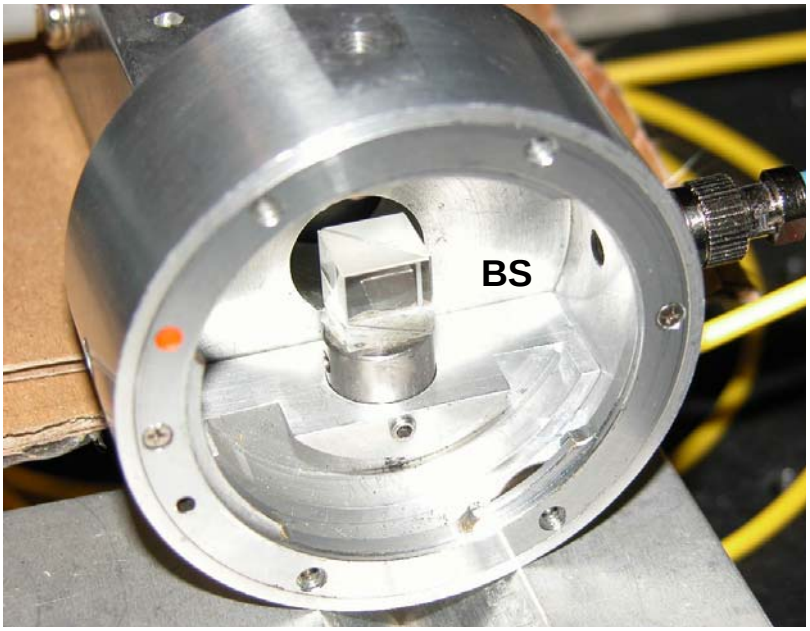

(b)

Figure 3.1 (a) Photo of out-of-plane SPI experimental setup. PBS – Polarising beamsplitter; ZL – Zoom lens. (b) Close-up of compact interferometer with ZL removed; BS – Beam combiner.

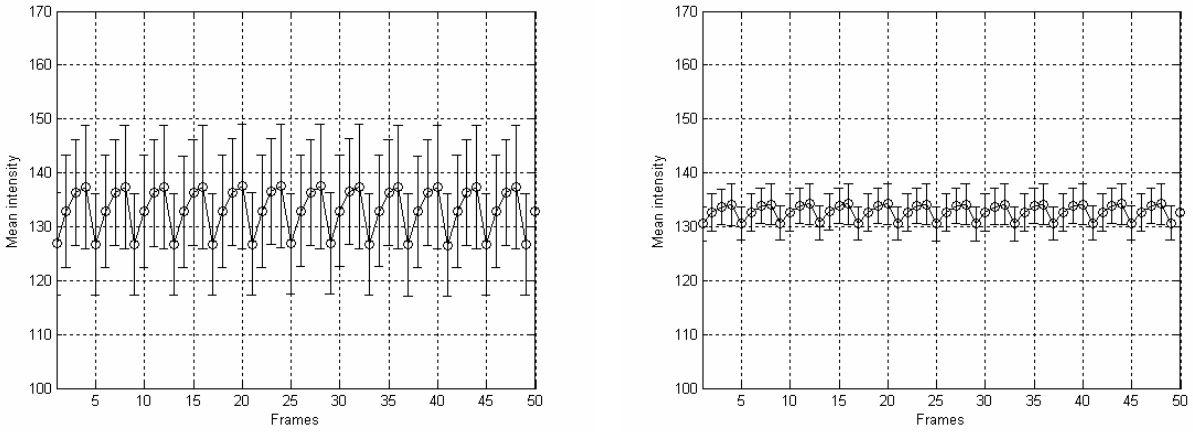

(a) (b)

Figure 3.2 Reference beam intensity variation due to leakage of a component of the orthogonally polarized object beam. (a) without polarizer and (b) with polarizer between fibre and phase modulator.

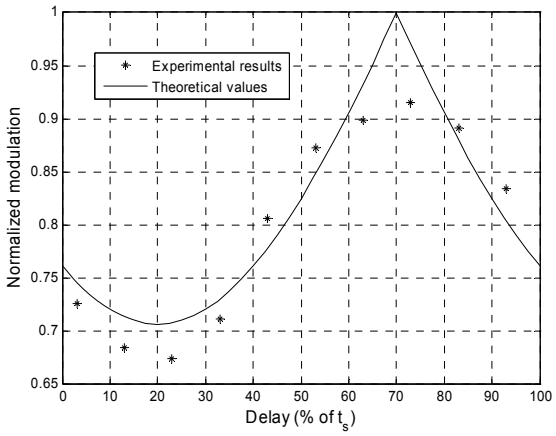

Figure 3.3 Variation in mean modulation amplitude plotted against delay between frame signal and the applied $\pi/2$ phase steps for images recorded at 70 Hz. The line is a numerical simulation, where the delay has been offset to approximately match the experimental points.

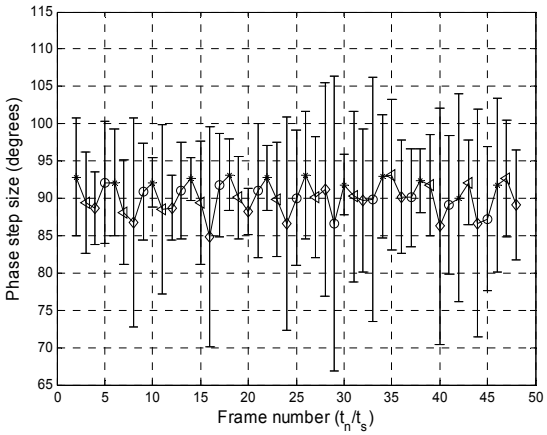

(a)

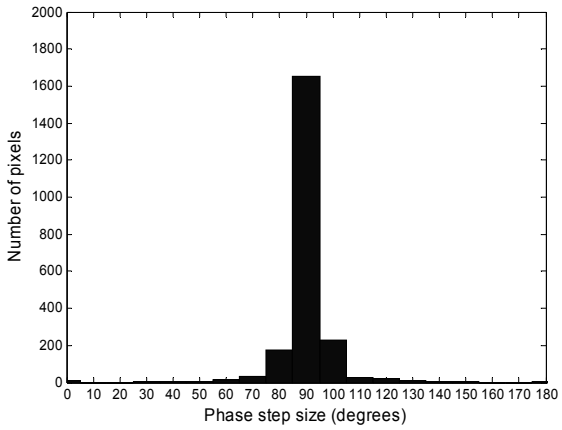

(b)

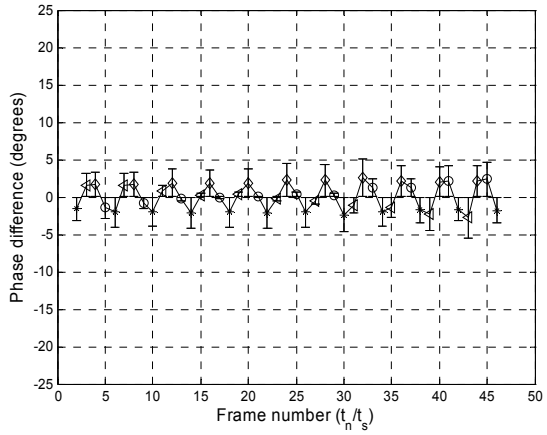

(c)

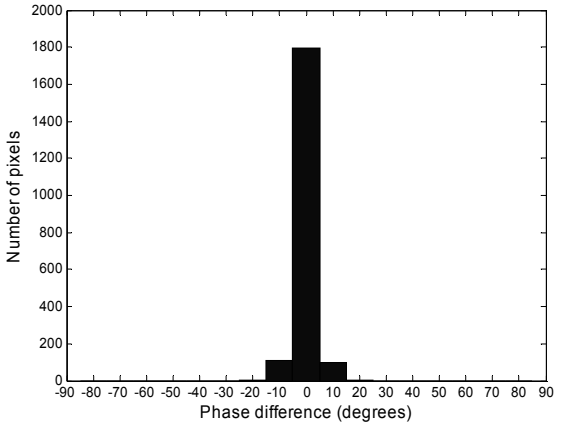

(d)

Figure 3.4 (a) Inter-frame phase step size plotted against frame number and (b) phase step size distribution for all frames recorded for a stationary object with a frame rate of 33 kHz. (c) Inter-frame phase difference plotted against frame number and (d) phase difference distribution, for the same image sequence as (a) and (b). In (a) and (c), a different symbol is used for every fourth point to emphasize the periodic phase fluctuation. The error bars show plus and minus one standard deviation about the mean.

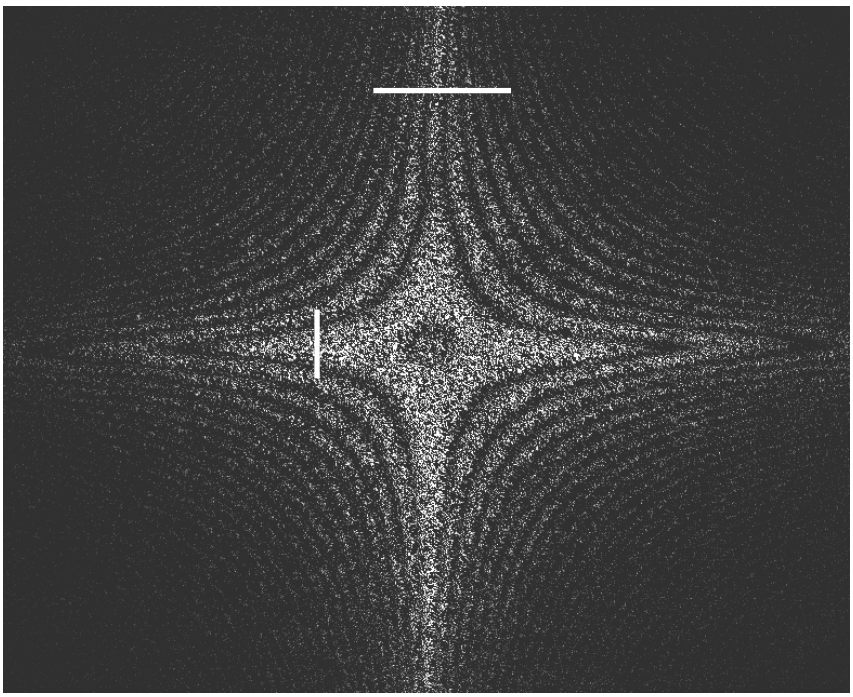

Figure 3.5 Time-averaged subtraction fringe pattern recorded at 70 frames per second showing the target vibrating at 250 Hz. The horizontal ROI was interrogated at 33 kHz, corresponding to a maximum normalized velocity of 0.25 (maximum surface velocity of 1.1 mm/s, λ=532 nm and η=2). The vertical ROI was interrogated at 10 kHz, corresponding to a maximum normalized velocity of 0.19 (maximum surface velocity of 0.25 mm/s, λ=532 nm and η=2).

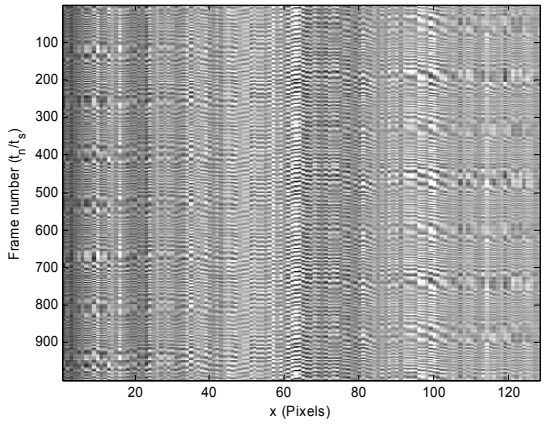

Figure 3.6 Spatio-temporal speckle pattern showing intensity variation for the horizontal ROI (128 × 1 pixels) recorded at 33 kHz for object vibrating harmonically at 250 Hz.

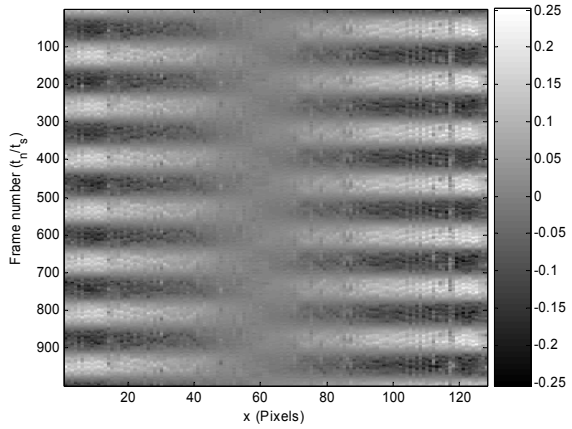

(a)

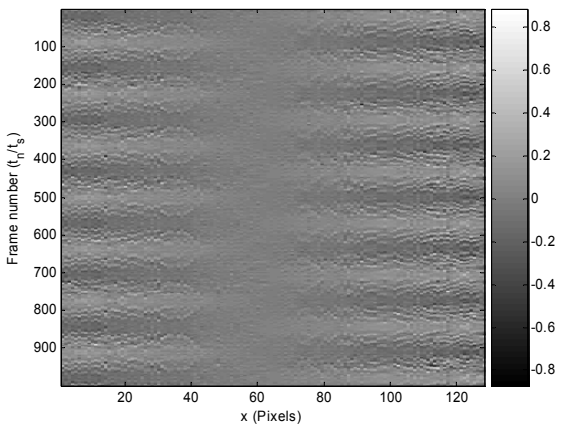

(b)

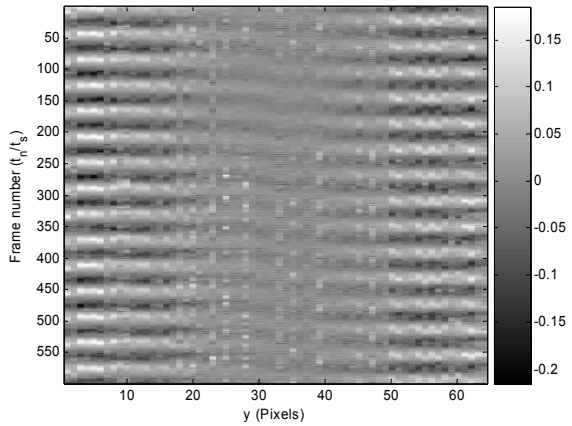

(c)

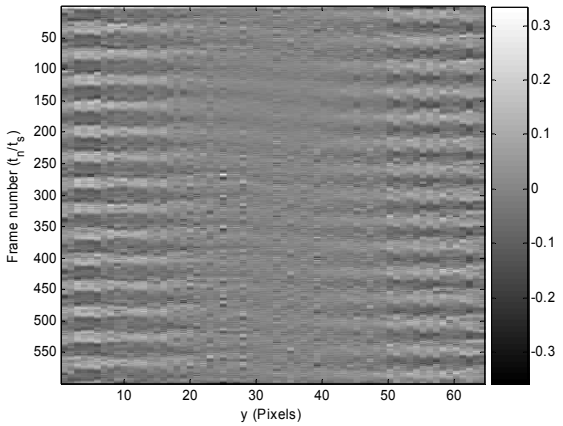

(d)

Figure 3.7 (a) Normalized velocity, $\Delta\Phi/\pi$, and (b) normalized acceleration $\Delta^2\Phi/(2\pi^2 fts)$ for the horizontal ROI (camera operating at 33 kHz). (c) Normalized velocity and (d) normalized acceleration for the vertical ROI (camera operating at 10 kHz), rotated to show y-axis horizontal.

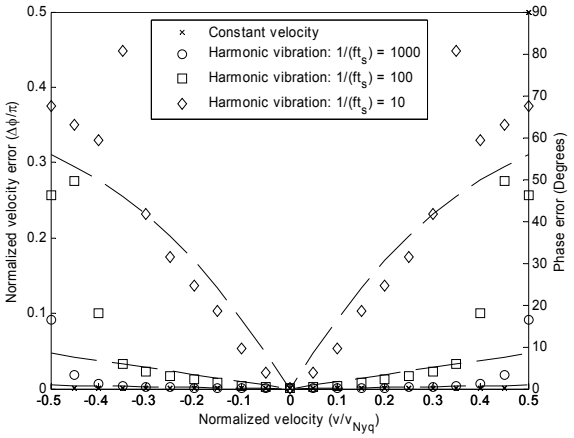

(a)

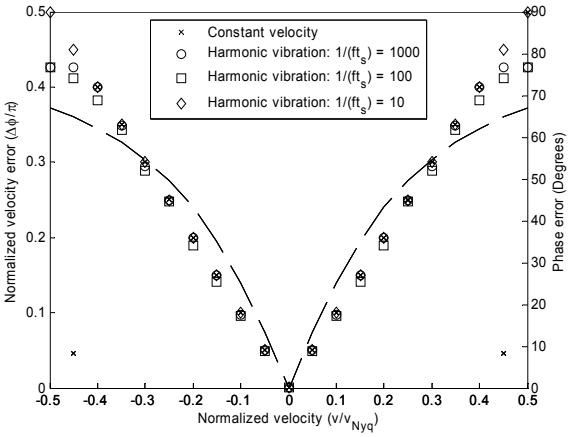

(b)

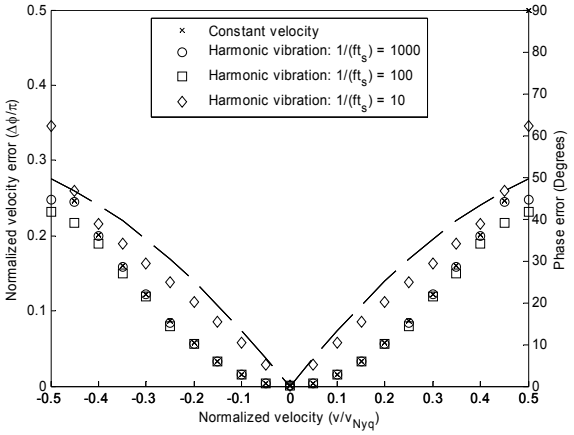

(c)

Figure 3.8 Maximum normalized velocity error plotted against normalized surface velocity for (a) Carré's algorithm (b) 4-frame algorithm and (c) 5-frame algorithm.

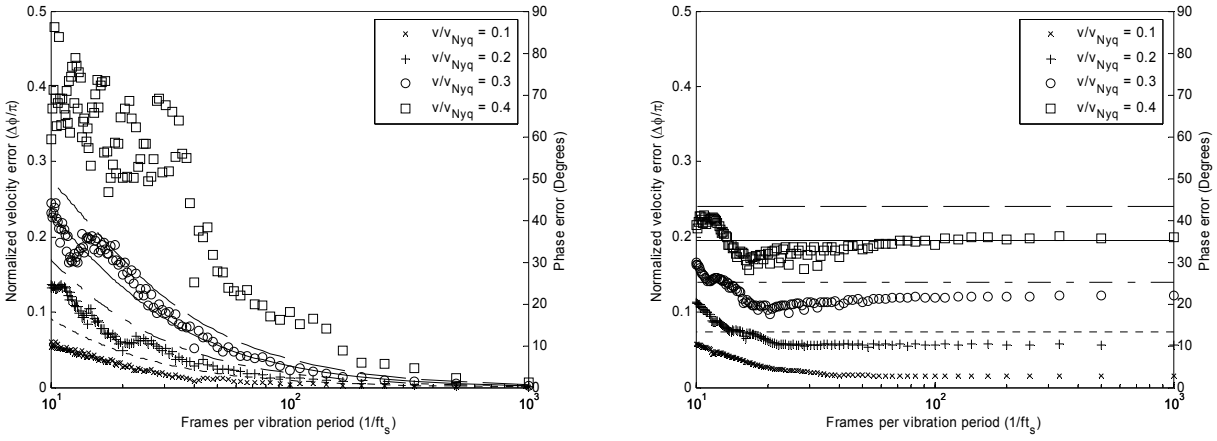

(a) (b)

Figure 3.9 Maximum normalized velocity error plotted against number of frames per vibration period for (a) Carré's algorithm, and (b) the 5-frame algorithm. Influence of maximum normalized surface velocity.

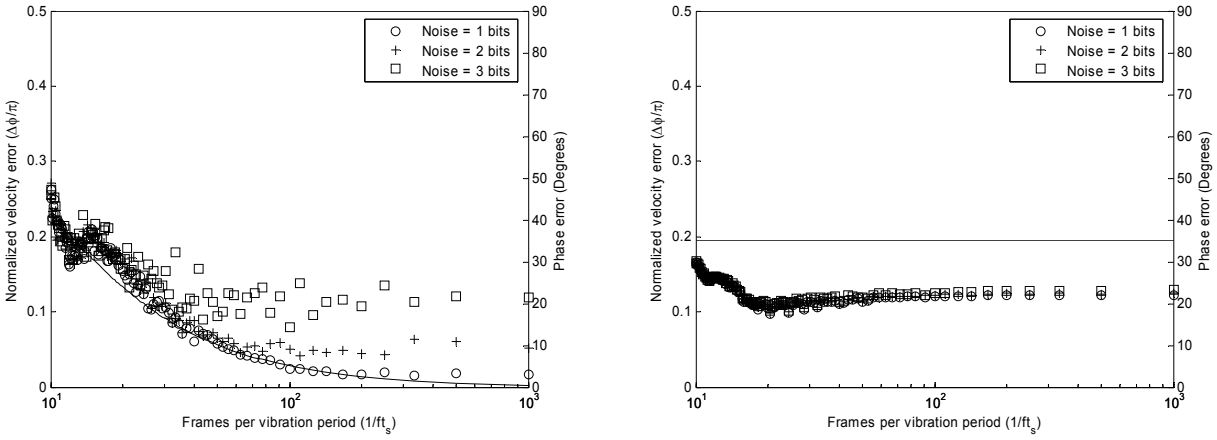

(a) (b)

Figure 3.10 Maximum normalized velocity error plotted against number of frames per vibration period for (a) Carré's algorithm, and (b) the 5-frame algorithm. Influence of intensity noise for $v_{max}/|v_{Nyq}| = 0.3$.

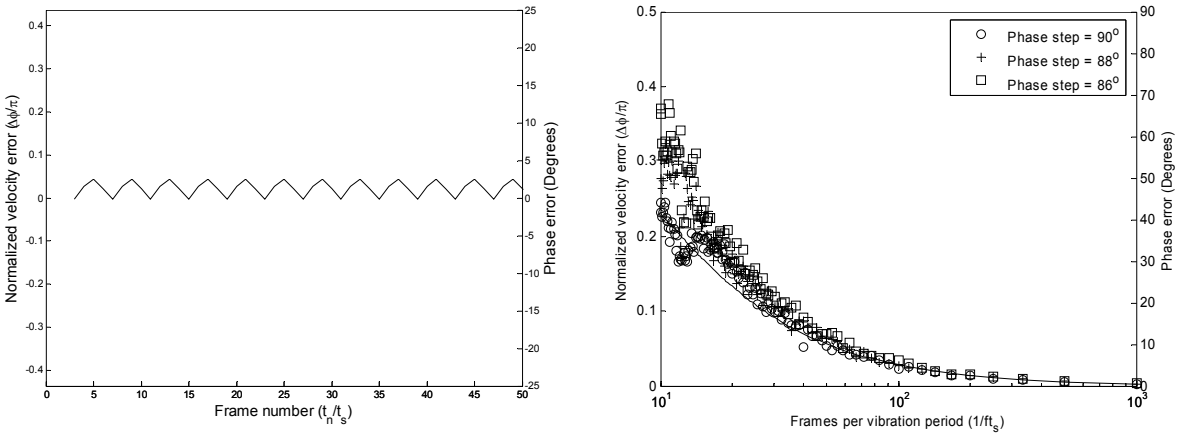

(a) (b)

Figure 3.11 (a) Normalized velocity error plotted against frame number for staircase phase step error of 86º and $v_{max}/|v_{Nyq}| = 0$. (b) Maximum normalized velocity error plotted against number of frames per vibration period for Carré's algorithm. Influence of staircase phase step error for $v_{max}/|v_{Nyq}| = 0.3$.

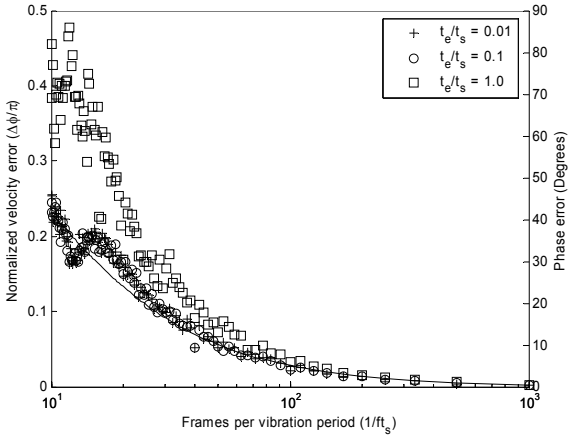

Figure 3.12 Maximum normalized velocity error plotted against number of frames per vibration period for Carré's algorithm. Influence of exposure for $v_{max}/|v_{Nyq}| = 0.3$.

4

High-Speed Sub-Nyquist Spatial Phase-stepped SPI

A spatial phase-stepped SPI system based on the high-speed CMOS camera was constructed. The system used a pair of binary gratings to introduce double-channel sensing and fixed phase step between the two channels. The spatial phase step size was calibrated by inter-frame phase stepping. A numerical and analytical error analysis for the system was performed and compared to that of the inter-frame phase-stepped system to demonstrate the increased dynamic range. The maximum surface velocity was increased to $\pm 1.0v_{Nyq}$. Sub-Nyquist theory was implemented for dynamic measurements and the measurement range with a continuous-wave laser illumination was increased by an order of magnitude with respect to inter-frame phase stepping to $\pm 3.0v_{Nyq}$. With reduced exposure, for example from pulsed laser illumination, the surface velocity could theoretically be recovered to $\pm 15.9v_{Nyq}$ and the surface acceleration to $\pm 253.3v_{Nyq}$ with the current set-up.

4.1 Simulation of spatial phase-stepped SPI

As discussed in Chapter 2, an alternative to inter-frame phase modulation is to spatially separate images onto one or multiple detectors and to introduce fixed phase steps between the images. The simultaneous acquisition of the phase-stepped interferograms eliminates errors due to phase changes that might occur during the acquisition of

multiple images, although the requirements for system alignment become more stringent. Specifically for dynamic measurements with SPI, the assumption made for inter-frame phase-stepping that the surface velocity is linear during the acquisition of four frames is no longer required. However, the reduction in interference visibility due to surface motion during a single exposure still applies.

In order to understand the expected differences in operation between inter-frame and spatial phase-stepped high-speed SPI, a simulation was undertaken. For inter-frame phase-stepped SPI, the model described in Section 3.3 for error analysis calculated a 256 × 1 pixel fringe pattern using equation (2-22) for an object phase distribution $\Phi_O(x,t_n)$ representing a central node and two regions vibrating harmonically out-of-phase, equation (3-10).

Figure 4.1(a) shows the composite spatiotemporal image that was constructed by calculating the intensity for $0 < t_n < 2/(ft_s)$, i.e the number of rows required for two vibration periods at the chosen frequency. A maximum surface velocity of $v_{max}/|v_{Nyq}| = 0.2$ was used. The surface velocity at each t_n was also calculated, and used to calculate the reduction in fringe visibility for an exposure of $t_e=0.1t_s$. A uniform inter-frame phase step of $\Phi_R(t_n)=\frac{t_n}{t_s}\frac{\pi}{2}$ was applied. The random speckle phase in $\Phi_O(x,t_n)$ was set to zero in order to visualize the process more clearly.

The advantage of using the maximum surface velocity normalized to the Nyquist velocity limit is that specific interferometer parameters do not need to be known. However, for completeness, the assumed values were: detector sampling period $t_s=10\mu s$ (i.e. a camera frame rate of 100 kHz); $\lambda=532$ nm; $\eta=2$. These values enable v_{Nyq} to be defined, from which the required maximum surface velocity is determined, in this case $0.2v_{Nyq}$. The object vibration period was f=1 kHz, enabling the number of frames required for two vibration periods to be determined.

Figure 4.1(b) shows the wrapped phase calculated using Carré's algorithm, equation (2-24). In our implementation for all phase stepping algorithms, the phase at a pixel is marked as invalid (NaN in Matlab) if the intensity takes a value 0 or 255 (for an 8-bit image) at that pixel in any one of the phase stepped images. Additionally, the phase is also marked invalid if the modulation amplitude calculated from the intensity values is less than 5% of the maximum value (127.5 for an 8-bit image). For the simulated data, the intensity of the fringes was in the range 1 to 254 and all pixels modulate with the

maximum value. The marked pixels in Figure 4.1(b) arise due to the additional checks in Carré's algorithm, specifically that values inside the square root in the numerator are not negative. The non-uniform surface motion causes these pixels to be marked. Figure 4.1(c) shows the normalized velocity calculated from phase differences between adjacent frames (rows) of Figure 4.1(b) and is in the defined range $\pm 0.2 v_{Nyq}$. Finally Figure 4.1(d) shows the error between the theoretical and calculated normalized velocity. Errors arise due to the non-uniform surface motion and are greatest where the surface velocity is highest.

Figure 4.2 shows the equivalent simulation for spatial phase stepping for a vibration amplitude of $0.2 v_{Nyq}$. The intensity of N images, equally sampled on x_N (by N separate regions of a single detector or N separate detectors) were calculated at time t_n using the relation:

$$I_{n,N}(x,t_n) = I\left(1 + V\text{sinc}\left[\frac{\Delta}{2}\right]\cos\left[\Phi_O - \Phi_R\right]\right) \qquad \textbf{(4-1)}$$

where the random speckle phase in $\Phi_O(x,t_n)$ was again set to zero. Instead of an inter-frame phase step, $\Phi_R(t_n) = \frac{t_n}{t_s}\frac{\pi}{2}$, a constant phase step of $\Phi_R = (N-1)\frac{\pi}{2}$ was introduced between each image. All other parameters remained the same as for the inter-frame phase-step simulation of Figure 4.1.

Figure 4.2(a) shows the composite spatiotemporal image (i.e. for increasing t_n) that was calculated for two vibration periods. Figure 4.2(b) shows the wrapped phase calculated using the four-frame algorithm, equation (3-16). Clearly, with the four interferograms representing the same time instant, there is no advantage to using Carré's algorithm. No invalid phase pixels were marked. Figure 4.2(c) shows the normalized velocity calculated from wrapped phase differences between adjacent frames and is in the defined range $\pm 0.2 v_{Nyq}$. Finally Figure 4.2(d) shows the error between the theoretical and calculated normalized velocity. As expected, this error is significantly smaller than for the corresponding inter-frame phase-stepped simulation, Figure 4.1(d), because errors due to the velocity non-linearity have been eliminated.

Spatially separating images on to multiple detectors is not practical for most high-speed applications, where the additional hardware cost can quickly become prohibitive.

Spatially separating the images on to separate regions of a single detector is an alternative, although the resolution of each image is then reduced. For high-speed applications, the number of pixels available is reduced and therefore it is advantageous to restrict the number of separate images recorded on a single detector. If N=2 images are recorded at times t_n and t_{n+1} the phase difference can be calculated from the resulting four images using the relation[84]:

$$\Delta\Phi_O(x,t_n)-\frac{\pi}{2} \quad = 2\tan^{-1}\frac{I_{n,N+1}-I_{n+1,N}}{I_{n,N}-I_{n+1,N+1}} \tag{4-2}$$

where at a given pixel $\Delta\Phi_O(t_n)=\Phi_O(t_{n+1})-\Phi_O(t_n)$ represents the change in phase due to the surface deformation between frames.

Figure 4.3(a) shows the composite spatiotemporal image (i.e. for increasing t_n) that was calculated for two vibration periods. Figure 4.3(b) shows the phase difference calculated using the single step algorithm, equation (4-2). Note that compared to Figure 4.2(b) the phase difference between frames is calculated directly, and so does not need to be performed as a separate step. The marked pixels in Figure 4.3(b) arise due to the modulation amplitude check for the single step algorithm: it can be shown that the modulation amplitude contains a term proportional to $\sin\left(\psi+\frac{\Delta\Phi_O}{2}+\frac{\pi}{4}\right)$, i.e. the modulation amplitude is zero at certain values of the random speckle phase, ψ, and deformation of the target. Figure 4.3(c) shows the normalized velocity and is in the defined range $\pm 0.2v_{Nyq}$. Finally Figure 4.3(d) shows the error between the theoretical and calculated normalized velocity. Again, the error is smaller than for the corresponding inter-frame phase-stepped simulation, Figure 4.1(d), because errors due to the velocity non-linearity have been eliminated. However, the errors are larger than those obtained with the four-image algorithm, Figure 4.2(d). The single step algorithm uses fewer phase-stepped images to calculate the phase difference and is therefore more sensitive to the phase change during the exposure. If the exposure is further reduced, e.g. $t_e=0.01t_s$, the error in normalized velocity equals that obtained with the four-image algorithm: the effects of exposure and surface velocity on accuracy are explored in Section 4.4.

The errors in inter-frame phase-stepped SPI become unacceptable above a maximum surface velocity of $0.3v_{Nyq}$, and the approach fails completely before the Nyquist fringe sampling limit of $0.5v_{Nyq}$. Grievenkamp introduced sub-Nyquist interferometry to measure large aspheric profiles in which the magnitude of the phase difference between adjacent pixels exceeded π radians. Provided that the phase was measured accurately, the Nyquist limit was due entirely to the reconstruction (spatial unwrapping) algorithm. A large increase in the measurement range of the interferometer was achieved by assuming that the spatial derivative of the aspheric surface shape (i.e. its slope) was continuous. By analogy, the magnitude of the phase difference between adjacent frames in high-speed SPI could exceed π radians if the temporal derivative of the deformation (i.e. velocity) is continuous. Spatial phase-stepped SPI is immune to non-linear surface motion, so the phase is measured accurately and the reconstruction algorithm (temporal unwrapping) enables the Nyquist limit to be exceeded.

Figure 4.4 shows the simulation for spatial phase-stepped sub-Nyquist SPI for a vibration amplitude of $2v_{Nyq}$ and the four step algorithm, N=4. Figure 4.4(a) shows the composite spatiotemporal image is sub-sampled in the regions of highest surface velocity, which is repeated in the wrapped phase map, Figure 4.4(b). Figure 4.4(c) shows the wrapped phase differences between adjacent frames (rows) of Figure 4.4(b) which are wrapped in the range $\pm 1.0v_{Nyq}$. Figure 4.4(d) shows the normalized velocity calculated by unwrapping each column of Figure 4.4(c) which is in the defined range $\pm 2.0v_{Nyq}$. In order to extract the correct velocity, the assumption of continuous surface velocity is used to add the correct multiple of $2v_{Nyq}$ to the normalized velocity, i.e:

$$\frac{\overline{\Delta\Phi_O(x,t_n)}}{\pi} = \frac{\Delta\Phi_O(x,t_n)}{\pi} \pm k2v_{Nyq} \qquad \textbf{(4-3)}$$

or

$$\overline{\Delta\Phi_O(x,t_n)} = \Delta\Phi_O(x,t_n) \pm k2\pi v_{Nyq}$$

where $\overline{\Delta\Phi_O(x,t_n)}/\pi$ is the correct normalized velocity, $\Delta\Phi_O(x,t_n)/\pi$ is the measured normalized velocity modulo $2v_{Nyq}$ and k is an integer. Hence the assumption of continuous velocity is used to unwrap the normalized velocity through t_n. Figure 4.4(e) shows the wrapped and unwrapped normalized velocity for column 64. Finally, Figure 4.4(f) shows the error in the normalized velocity is larger than for the case of $\pm 0.2v_{Nyq}$,

Figure 4.2, but can be reduced if a smaller exposure is used. The effects of exposure and surface velocity on the accuracy are explored in Section 4.4.

Figure 4.5 shows the simulation for spatial phase-stepped sub-Nyquist SPI for a vibration amplitude of $2v_{Nyq}$ and the single step algorithm, N=2. Figure 4.5(a)-(d) correspond directly to Figure 4.4. Marked pixels arise in the phase, Figure 4.5(b), with the single step algorithm due to zero modulation amplitude at pixels where the term $\sin\left(\psi + \frac{\Delta\Phi_O}{2} + \frac{\pi}{4}\right)$ is zero. As noted previously, the single step algorithm calculates directly the phase difference between frames, and so the difference does not need to be performed as a separate step. The normalized surface velocity, Figure 4.5(c), is wrapped in the range $\pm 1.0v_{Nyq}$, i.e. modulo 2 v_{Nyq}. Figure 4.4(d) shows the normalized velocity calculated by unwrapping each column of Figure 4.4(c) which is in the defined range $\pm 2.0v_{Nyq}$. The assumption of continuous surface velocity is used to add the correct multiple of $2v_{Nyq}$ to the normalized velocity, i.e. to unwrap the normalized velocity through t_n. Figure 4.4(e) shows the wrapped and unwrapped normalized velocity for column 64. Finally, Figure 4.4(f) shows the error in the normalized velocity is slightly larger than for the case of $0.2v_{Nyq}$, Figure 4.3. The effects of exposure and surface velocity on the accuracy are explored in Section 4.4.

Finally for this section, just as the displacement that produces a π radians phase change between frames determines the Nyquist velocity limit, so the sub-Nyquist velocity that produces a π radians phase change in normalized velocity between frames determines the acceleration limit. Setting $\Delta^2\Phi_O = \pi$ in equation (3-8) yields a sub-Nyquist velocity unwrapping limit of:

$$w'(x,y,t_n) < \frac{1}{2\pi f t_s}\left|v_{Nyq}\right| \qquad \textbf{(4-4)}$$

Thus for the values used in the current simulation, f=1 kHz and t_s=10μs, unwrapping the normalized velocity is successful for velocities up to $15.9v_{Nyq}$ which was verified in the simulation.

For velocities that exceed the limit of equation (4-4), the measured velocity will be sub-sampled but can be recovered if it is assumed that the surface *acceleration* is continuous. The surface jerk (rate of change of acceleration) is given by the relation:

$$w'''(x,y,t_n)=\frac{\lambda}{2\pi\eta t_s^3}\Delta^3\Phi_O(x,y,t_n) \tag{4-5}$$

where at a given pixel $\Delta^3\Phi_O(t_n)=\Delta^2\Phi_O(t_{n+1})-\Delta^2\Phi_O(t_n)$ represents the rate of change in the rate of change in the phase difference between frames. Rearranging equation (4-5) yields:

$$\frac{w'''(x,y,t_n)}{(2\pi f)^2\left|v_{Nyq}\right|}=\frac{1}{\pi(2\pi f t_s)^2}\Delta^3\Phi_O(x,y,t_n) \tag{4-6}$$

i.e the surface jerk normalized to the magnitude of the maximum jerk present for harmonic vibration at the Nyquist velocity limit. Setting $\Delta^3\Phi_O=\pi$ in equation (4-6) yields a sub-Nyquist acceleration limit of:

$$w''(x,y,t_n)<\frac{1}{(2\pi f t_s)^2}\left|v_{Nyq}\right| \tag{4-7}$$

Thus for the values used in the current simulation, f=1 kHz and t_s=10μs, unwrapping the normalized acceleration will be successful for velocities up to $253.3v_{Nyq}$ which was verified with the simulation. Clearly it is not required that the surface jerk, $\Delta^3\Phi_O$, is determined experimentally: it is used to set the surface acceleration unwrapping limit.

Figure 4.6 shows the simulation for spatial phase-stepped sub-Nyquist SPI for a vibration amplitude of $40v_{Nyq}$ and the single step algorithm, N=2. Hence in this case, for the values used in the current simulation, f=1 kHz and t_s=10μs, the continuous velocity limit of $15.9v_{Nyq}$ has been exceed, but it is within the continuous acceleration limit of $253.3v_{Nyq}$. Figure 4.6(a) and (b) show that both the composite spatiotemporal image and the phase difference between frames (calculated directly by the one step algorithm) are sub-sampled. Figure 4.6(c) shows the normalized surface acceleration and is in the range $\pm1.0v_{Nyq}/(2\pi ft_s)$. Figure 4.6(d) shows the normalized acceleration for column 64, where the discontinuities are clearly visible. In order to extract the correct acceleration, the assumption of continuous surface acceleration is used to add the correct multiple of $2v_{Nyq}/(2\pi ft_s)$ to the normalized acceleration, i.e:

$$\frac{\overline{\Delta^2\Phi_O(x,t_n)}}{2\pi^2 ft_s} = \frac{\Delta^2\Phi_O(x,t_n)}{2\pi^2 ft_s} \pm k\frac{2v_{Nyq}}{2\pi ft_s} \qquad \textbf{(4-8)}$$

or

$$\overline{\Delta^2\Phi_O(x,t_n)} = \Delta^2\Phi_O(x,t_n) \pm k2\pi ft_s v_{Nyq}$$

where $\overline{\Delta^2\Phi_O(x,t_n)}/2\pi^2 ft_s$ is the correct normalized acceleration, $\Delta^2\Phi_O(x,t_n)/2\pi^2 ft_s$ is the measured normalized acceleration modulo $2v_{Nyq}/2\pi ft_s$ and k is an integer. Hence the assumption of continuous acceleration is used to unwrap the normalized acceleration through t_n. In principle, the surface velocity could be recovered by summation of the incremental velocity differences at a pixel (column). When the data implicitly include some known or stationary reference, recovery of the absolute spatiotemporal velocity profile would be possible. For the general case of continuous anharmonic motion with unknown initial velocity, it would be best to leave the velocity changes between frames as surface acceleration; i.e., the instrument could be considered to be a multipoint accelerometer. That approach would be analogous to the present use of the system as a multi-point vibrometer.

Sub-Nyquist interferometry assumes that the phase is measured accurately so that the Nyquist limit is due entirely to the reconstruction (spatial unwrapping) algorithm. In order to achieve accurate phase reconstruction in the presence of a high spatial phase gradient, Grievenkamp covered the CCD with a mask to reduce the lateral extent of each pixel and hence reduce the phase variation across each pixel. By analogy, in order to achieve accurate phase reconstruction in the presence of a high temporal phase gradient, the exposure, t_e, must be restricted. If an appropriate exposure is not chosen, the fringe visibility is reduced because the fringes are 'smeared out' by the phase change during the exposure. Hence for Figure 4.6 only, an exposure of $t_e=0.001t_s$ was used, equivalent to an exposure of 10 ns for a detector frame rate of 100 kHz ($t_s=10$ μs). The effects of exposure and surface acceleration on accuracy are explored in Section 4.4.

4.2 Experimental system for spatial phase-stepped SPI

A pair of binary diffraction gratings were used to double the wavefront and introduce a $\pi/2$ phase step by introducing a lateral shift between the gratings. The binary gratings were designed with a phase modulation depth chosen to eliminate the even diffracted

orders for the wavelength of the YAG laser, so that the zero order was suppressed and the +1 and -1 diffracted orders were dominant. Both diffracted orders were imaged on to the CMOS camera. The spatial resolution is reduced compared to multiple cameras but the optical arrangement is simpler and more stable. Because only two diffracted order are present on the sensor, the spatial resolution is maximized for high speed detectors. To the best of our knowledge, it is the first time binary gratings have been used to both separate the images and to introduce phase steps for phase measurement.

The experimental system was based on the high-speed inter-frame phase-stepped system described in Section 3.1. Introducing the binary gratings required a change to the imaging system, which is described in Section 4.2.1. Alignment of the spatially separated images is crucial for accurate phase stepping, and is described in Section 4.2.2.

4.2.1 Design of the imaging system

Two identical binary gratings with a nominal pitch of 38 μm were used. The phase modulation depth of the gratings was originally designed to suppress the 0, ±2, ±4, etc. diffracted orders at 532 nm for a shape measurement illumination system that projected interference fringes between the +1 and -1 diffracted orders[85]. The pitch of the grating was verified, Figure 4.7, using the equation:

$$\zeta_0 = \frac{m\lambda}{\sin A \pm \sin B} \qquad \textbf{(4-9)}$$

where ζ_0 is the pitch of the grating, m is the diffraction order, λ is the wavelength of the laser used, A is the incident beam angle as measured from the grating normal ($A=0^o$ in this setup) and B is the diffracted beam angle as measured from the grating normal. The designed pitch of the grating was 38 μm and the measured value was 37.8 μm. In the same experiment, the leakage (efficiency) of the zero order was measured as 1.3 % of the total input, compared to 31% and 32% for the +1 and -1 orders, respectively.

A schematic of the high-speed spatial phase-stepped SPI system is shown in Figure 4.8. The significant changes with respect to the inter-frame phase stepped CMOS system of Figure 2.2 were in the imaging system. An aperture, A1, and the first binary grating, G1, were placed in the object beam, in order to generate two spatially separated images

on the CMOS camera detector, Figure 4.9. The zoom lens of the original system was replaced with bulk-optics mounted in Microbench to enable greater flexibility for adjusting the optical components. The object was imaged by two lenses, L1 and L2 of focal lengths f_1=100 mm and f_2=50 mm respectively, on to the 1024×1024 element array of the CMOS camera (Photonfocus, MV-D1024, 8-bit resolution).To choose the distance between the detector and L2, the magnification of the system, Figure 4.10(a), was calculated as,

$$M = M1 \times M2 = \frac{i1}{o1} \times \frac{i2}{o2} = \frac{50 \times 198}{1840 \times 220} = 0.24 \qquad \textbf{(4-10)}$$

where M is the overall magnification of the system, M1 and M2 are the magnifications of L1 and L2 respectively. The relationship between the overall magnification and the L2-detector distance is shown in Figure 4.10(a) and the maximum size of test object is inferred as shown in Figure 4.10(b). For the CMOS detector size of 10.9 x 10.9 mm^2, the focal lengths chosen for L1 and L2 and a nominal measurement region diameter of 140 mm, the distance between the sensor and the grating should be approximately 200 mm. The image size of a test object of 140-mm-diameter circular plate is 270 pixels by 270 pixels (corresponds to approximately 2.9 mm). The separation between the two diffracted images is proportional to the distance between G1 and the image plane. Figure 4.10(c) shows the relationship between grating-to-L2 distance and the separation of +1 and -1 diffracted orders. G1 was positioned with a grating-to-L2 distance of 8 mm (equivalent to grating-to-detector distance of 192 mm) to separate the ±1 diffracted orders without overlapping. Figure 4.10(d) shows examples of overlapped images.

Figure 4.11(a) shows a photograph of the experimental set-up of the imaging system, with the main features identified. Figure 4.11(b) shows a close-up of grating G1. It identifies that the grating could be rotated in its plane about the optical axis of L1 and L2, and translated in the z-direction with a micrometer for fine control of the magnification, to ensure equal sampling of the two diffracted images by the pixel array of the detector. Also, the grating could be translated in the x-direction in order to introduce a phase step between the diffracted orders, as described below.

A second aperture, A2, and the second phase grating, G2, were positioned in the collimated reference beam. The two diffracted reference beams were then combined

with the object beam by the beam combiner. G2 could also be rotated in its plane and translated perpendicular and parallel to its plane, as for G1.

For a unit-magnification imaging system, lateral translation of an amplitude grating by quarter of its pitch will result in $\pi/2$ phase steps. Hence alignment of the imaging system required, firstly ensuring that the two diffracted object images were sampled equally by the pixel array of the detector, and secondly ensuring that the relative phase step between the diffracted orders was $\pi/2$ radians at each pixel. The alignment process, critical for the accuracy of spatial phase stepping, is described in the following two sections.

4.2.2 Sub-pixel image alignment

In spatial phase-stepped systems where multi-channels are used, it is important that the interferograms are well aligned to each other. This is not a trivial task: if the speckle size is of the order of pixel size, each interferogram has to be aligned with sub-pixel accuracy with respect to the other phase-stepped interferograms. There are two issues that need be considered when combining phase stepped speckle interferograms from the two channels: translation of the grating for alignment of the image in x- and y- direction and the relative rotation between the object and reference gratings.

The alignment procedure comprised the following:

- Sub-pixel translation alignment for the (x,y) position of the object beam.
- Matching the reference beam to the object beam.
- Sub-pixel translation alignment for the (x,y) position of the reference beam.
- Alignment for the relative rotation of the object and reference gratings.

For the translation alignment of the object beam, an image correlation technique was used to quantify alignment errors between the two images of the object with sub-pixel accuracy. A correlation coefficient was calculated by the equation:

$$r = \frac{\sum_x \sum_y (A_{xy} - \overline{A})(B_{xy} - \overline{B})}{\sqrt{(\sum_x \sum_y (A_{xy} - \overline{A})^2)(\sum_x \sum_y (B_{xy} - \overline{B})^2)}} \quad \textbf{(4-11)}$$

where A and B represent the two diffracted images, and $\overline{A}$ and $\overline{B}$ are the mean intensities in the window of interest. An output of 1 represents the best correlation and 0 the poorest. As seen in Figure 4.11(b), the object grating was rotated to get a good match in y. Then the grating is translated in z-axis to adjust magnification until the images of the object are sampled equally by the detector pixel array. The highest value of correlation coefficient would indicate the best positioning of the object grating.

As shown in Figure 4.12, when the grating moves along z-axis towards to the best position, the correlation coefficient increases. When the grating moved away from the optimal position, the value decreases. Figure 4.13 shows a 2-D cross-correlation of the diffracted orders for the best position in Figure 4.12. The 2-D cross-correlation used 3 pixel by 3 pixel windows. The two darker regions at either side of the correlation are caused by the leakage of the zero diffracted order.

The alignment of reference beam grating is more straightforward than for the object grating because the intensity does not vary spatially as rapidly. So the object beam grating was aligned first and the reference beam grating matched to it. The x- and y-shifts that correspond to the best alignment of object beam were used for the reference beam. Then the sub-pixel alignment procedure is repeated for the reference grating: the grating was rotated to get a good match in y and then was translated in z-axis for best magnification. The correlation coefficient for best position was 0.98 compared to 0.9 for object beam.

After combining the two beams, the relative rotation between the two gratings needed to be aligned. A small relative rotation between the two gratings introduces a large phase gradient across the image. It can be seen in Figure 4.14 that a relative rotation of small angle α between the gratings produces a phase gradient of approximately $\frac{\alpha 2\pi}{\zeta_0}$ radians per pixel in the y-direction. For example, in the current setup, a relative rotation of α = 1 degree between the gratings leads to a phase difference of 8π radians between the top and bottom of the image (~ 270 pixels). In order to reduce the phase difference

introduced by the relative rotation of the reference with respect to the object grating, and to validate the size of the spatial phase step introduced by a relative translation in the x-direction of the reference grating with respect to the object grating, inter-frame phase stepping was used. The phase was calculated from four consecutive phase-stepped frames with the object stationary, and with thermal interference reduced to a minimum by appropriate shielding around the interferometer. The phase in both diffracted orders could be calculated, and the difference (modulo 2π) plotted. Figure 4.15(a) and (b) show the phase distribution and its histogram when the relative rotation between the gratings was approximately 3 degrees. As the angle reduces, Figure 4.15(c) and (d), the phase difference between the quadrants becomes more uniform, until the best achievable position is reached, Figure 4.15(e) and (f). The phase difference between quadrants with the minimum relative rotation between the gratings, is effectively the spatial phase step size achieved at each pixel, Figure 4.15 (e) and (f). For this rotation of the reference grating, Figure 4.16 shows the spatial phase step size achieved for x-translations of the reference grating at intervals of 10 μm. The plotted points are the mean over all pixels and the error bars show plus and minus three standard deviations. The gradient of the best fit line is $9^{o}/\mu m$, corresponding to 10 μm translation for a 90^{o} phase step i.e. a quarter of the pitch of the grating).

Following the above alignment procedure of the two gratings, a qualitative impression of the quality of the alignment could be obtained from SPI fringes, even though subtraction fringes were not used for dynamic measurements. Phase-referenced speckle patterns of a test object before and after an out-of-plane deformation are shown in Figure 4.17(a) and (b). Direct subtraction of corresponding pixels between the two images does not require any alignment of the diffracted orders: excellent quality subtraction fringes are obtained but there is no relative phase step between them, Figure 4.17(c). Cross-subtraction does require sub-pixel alignment of the two diffracted orders: slightly reduced fringe visibility was obtained due to small errors in the alignment, but the relative phase step between the diffracted orders was maintained, Figure 4.17(d). The relative phase step of approximately 115^{o} between the orders is seen by the shift in the fringe position between Figure 4.17

4.3 Vibration measurement

Figure 4.18 shows a time-averaged fringe pattern recorded with the spatial phase stepped system with the CMOS camera recording at 25 frames per second (1024 × 1024 pixels) for the centre-clamped circular test target vibrating at a natural frequency at 518 Hz. The time-averaged fringe pattern was used to identify the ROI for time-resolved measurements with the same CMOS detector, marked in Figure 4.8. The maximum vibration amplitude was estimated from the Bessel fringe order in the full-field time-averaged interferogram to be 0.36 μm, corresponding to a maximum surface velocity 1.25 mm/s or approximately 0.3 times the Nyquist velocity limit when the horizontal ROI indicated was interrogated at 20,000 frames per second, equation (3-4). The cylindrical lens L1 was inserted into the object beam using a connectorized mount on the end of the object fibre to illuminate the ROI.

A series of measurements were made with the spatial phase stepped system with the vibration amplitude varied for surface velocities between 0.5 and 4.0 times Nyquist limit. Additionally, for surface velocities between 0.10 and 0.5 times the Nyquist limit, inter-frame phase steps of 90^{o} were introduced in order to calibrate the system. For each surface velocity, a composite spatiotemporal speckle interferogram, with each row corresponding to a single frame of 656 by 1 pixels was transferred to the PC at 20 kHz frame rate.

Figure 4.19(a) shows a composite spatiotemporal speckle interferogram recorded with the spatial phase stepped system at a nominal surface velocity of $0.1v_{Nyq}$, but incorporating inter-frame phase stepping. The phase at each pixel modulating at above the 5% threshold was calculated from the recorded intensity from four consecutive frames using Carré's algorithm, equation (2-23), Figure 4.19(b). The two diffracted images are two independent measurements of velocity, although the measured phase is $\pi/2$ out of phase due to the spatial phase step. The phase difference between adjacent frames (rows) was calculated, and scaled to display the normalized velocity, Figure 4.19(c). The surface velocity calculated by inter-frame phase stepping is the same for each image. However, the phase difference between the corresponding pixels of each image gives an estimate of the phase step introduced by the relative lateral shift of the reference grating for the line ROI. A similar process was used to calibrate the size of the applied spatial phase with the object stationary, above, for the full image and at a lower frame rate. Figure 4.19(d) shows the mean phase difference for at each pixel over

the recorded frames (columns) with the error bars showing plus and minus one standard deviation about the mean. The mean is close to 90º at many pixels, and a typical standard deviation of 30º is comparable to that calculated with the target stationary for phase step size calibration, Figure 4.15(f). The standard deviation in the phase step error for the inter-frame phase stepped system was approximately 10º, Figure 3.4. The additional error is attributed to differences in the sampling of the diffracted speckle patterns, i.e. an image mismatch between the diffracted orders introduces an error in the phase difference between corresponding pixels. This conclusion is reached because, firstly, the lateral shift of the grating itself does not produce a rapid spatial variation in the phase step. Secondly, the mean phase difference between corresponding pixels for the same test target at a higher surface velocity of $0.15v_{Nyq}$ is included in Figure 4.19 (d) and lies within the error bound of the inter-frame phase step approach, showing that the difference is repeatable between data sets.

Figure 4.20(a) shows the normalized surface velocity calculated for the same data set using a modified version of the spatial phase step algorithm. The new, compensating spatial phase step algorithm uses the actual phase step recorded at each pixel, Figure 4.19(d). If the actual phase step between diffracted orders is α, incorporating a phase term due to the image mis-sampling between the diffracted orders, the phase difference can be calculated from N=2 images recorded at times t_n and t_{n+1} using a novel algorithm which was developed by the author :

$$\Delta\Phi_O(x,t_n) = 2\tan^{-1}\frac{\left(I_{n,N} - I_{n+1,N+1} + I_{n+1,N} - I_{n,N+1}\right)/\cos(\alpha/2)}{\left(I_{n,N} - I_{n+1,N+1} - I_{n+1,N} + I_{n,N+1}\right)/\sin(\alpha/2)} \qquad \textbf{(4-12)}$$

Prior to phase calculation, the intensity at corresponding columns between quadrants was scaled to obtain the same mean intensity and modulation amplitude. Figure 4.20(b) shows one column from the normalized surface velocity calculated by both spatial phase stepping and temporal phase stepping (left hand image) for column 207, for direct comparison. The difference between the normalized velocity calculated with spatial phase stepping and that calculated by inter-frame phase stepping is shown in Figure 4.20(c). The mean difference for each pixel (column) is shown in Figure 4.20(d), with the error bars showing plus and minus one standard deviation.

Figure 4.20(e) shows the equivalent difference between the normalized velocity calculated with the *standard* spatial phase stepping algorithm and that calculated by inter-frame phase stepping. Again, the mean difference for each pixel (column) for

column 207 is shown, Figure 4.20(f), with the error bars showing plus and minus one standard deviation. It is evident that the compensating algorithm produces a considerable improvement in the calculated velocity compared to the standard algorithm. At the best pixels, the mean velocity difference between the two approaches is zero, with a standard deviation of approximately 0.03.

Notice that when applying both the standard and compensating spatial phase step algorithms, equations (4-2) and (4-11) respectively, to data that incorporates an inter-frame phase step of $\pi/2$ radians, the actual phase change is $\Delta\Phi_O(x,t_n)+\frac{\pi}{2}$. Therefore the inter-frame phase step of $\pi/2$ radians must be subtracted from the calculated phase distribution.

Figure 4.21 shows the results from four data sets taken with inter-frame phase steps recorded with increasing nominal surface velocity. Figure 4.21(a) shows the same data set of Figure 4.19 and Figure 4.20, but plotted at the common x-axis scale used in Figure 4.21. Clearly the errors in the inter-frame phase stepped data become increasingly large, until eventually the approach fails completely by the theoretical limit of $0.5v_{Nyq}$. The spatial phase step approach still works at this surface velocity. There is no inter-frame phase data with which to compare at higher speeds, but the noise in the normalized surface velocity measured by spatial phase stepping remains at the same level, or in fact slightly less, than at the lower surface velocities.

Figure 4.22 and Figure 4.23 show data recorded with the spatial phase step system for nominal surface velocities beyond $0.5v_{Nyq}$, for all pixels and a single pixel respectively. Once the Nyquist limit is exceeded, the normalized velocity is obtained modulo $2v_{Nyq}$. The correct velocity is obtained by unwrapping the normalized velocity by adding the correct multiple of $2v_{Nyq}$. Although results were recorded up to a nominal velocity of $4v_{Nyq}$, unwrapping was only successful on the data set at $3.0v_{Nyq}$, Figure 4.22(d) and Figure 4.23(d). The pixel with the highest surface velocity that unwrapped successfully is shown in Figure 4.23(d), and is different from the other three plots. This apparent limit is due to the relatively long exposure period of the detector, $t_e/t_s=0.1$, and is discussed in the following section. However, a velocity of approximately $\pm 3.0v_{Nyq}$ was achieved, approximately an order of magnitude larger than achieved with the inter-frame phase step system.

4.4 Error analysis for sub-Nyquist spatial phase-stepped SPI

For spatial phase stepping, the measurement errors depend on the surface acceleration (i.e. the frequency and amplitude of vibration) and the camera frame rate, and cannot be determined without a priori knowledge of the vibration to be measured. The model described in Section 4.1, representing a phase distribution of a central node and two regions vibrating harmonically out of phase, equation (3-10) was used to determine the effect of these parameters on the measurement accuracy. Simulations at *specific* surface velocities and for particular phase algorithms were shown in Figure 4.2 through to Figure 4.6.

The maximum error between the calculated normalized velocity and the value used to calculate the simulated interferograms is shown in Figure 4.24 for a range of normalized velocities. Due to the significantly extended normalized velocity range analysed compared to that of the error analysis for inter-frame phase stepped system, an exposure of $t_e=0.001t_s$ was used for all subsequent plots unless stated otherwise. The other parameters in the simulation remained the same as for Section 4.1. It is the maximum error (that occurs at the maximum surface velocity) that is of interest, rather than the rms error over the whole vibration period. The equivalent phase error is shown on the second vertical axis of Figure 4.24.

The scale of the error is an order of magnitude less than for the equivalent plots for inter-frame phase stepping, Chapter 3, and significantly smaller than the experimentally determined difference between the temporal and spatial phase stepped results of the order of $0.1v_{Nyq}$. For sufficiently small t_e, the phase difference between frames (rows) will be measured accurately from the intensities recorded at two discrete times. The velocity is calculated from the phase difference assuming continuous acceleration. For the case of harmonic vibration, the nonlinear surface motion between frames leads to an error in the recovered velocity. The error is significantly smaller for spatial phase stepping compared to inter-frame phase stepping because the nonlinear motion over only two frames (rather than four) is considered, and it is the acceleration that introduces a systematic error (rather than the surface velocity introducing a measurement error via phase step miscallibration). The motion nonlinearity is not significant for a large number of frames per vibration period, e.g. $1/(ft_s) = 1000$ in Figure 4.24, and the normalized velocity error is negligible. However, the velocity error increases as the number of frames per vibration period falls, e.g. $1/(ft_s) = 100$ and 10 in

Figure 4.24 , and the error is larger. The spatial phase step approach is intrinsically insensitive to linear phase changes introduced by a continuous surface velocity, and therefore this surface motion was not considered in the simulation (as it was for the inter-frame phase step error analysis of Chapter 3).

For $v/v_{Nyq} > 1$, the normalized velocity is wrapped modulo $2v_{Nyq}$. The normalized velocity error was calculated by comparing the wrapped velocity distributions so that the error was not dependent on the unwrapping algorithm. For each number of frames per vibration period considered, the sub-Nyquist velocity unwrapping limit of equation (4-4) represents a limit beyond which the surface velocity cannot be determined uniquely, without summing the acceleration for a known initial velocity profile as discussed above. Therefore the sub-Nyquist velocity unwrapping limits of $(ft_s)/2\pi$ are marked by vertical lines at velocities of $1.6v_{Nyq}$ and $15.9\ v_{Nyq}$ beyond which no further calculations were performed.

The effect of the nonlinear surface motion on the recovered velocity can be modelled. Errors arise in the recovered phase due to non-linearity in the surface acceleration between frames. Replacing the normalized surface jerk with the normalized surface velocity in equation (4-6) , and including an empirically determined scaling factor of 1/25 gives the maximum normalized velocity error:

$$\frac{\Delta\Phi}{\pi} = \frac{1}{25}(2\pi f t_s)^2\left(\frac{v_{\max}}{|v_{Nyq}|}\right) \qquad \textbf{(4-13)}$$

Equation **(4-12)** is plotted in Figure 4.24 for the three values of ft_s considered and shows good agreement with the points obtained from the simulation. The figure shows that all the algorithms behave in the same way: the error due to jerk is systematic for algorithms.

Figure 4.25 shows the maximum normalized velocity error plotted against the number of frames per surface vibration period, for a range of surface velocities. Again, all the algorithms show the same error, due to the systematic nonlinearity in surface acceleration. The errors decrease as the number of frames per vibration period increase and as the surface velocity decreases, as the effect of surface jerk on the calculated velocity reduce. The sub-Nyquist velocity unwrapping limit of $2\pi v_{max}/|v_{Nyq}|$, equation (4-4) are marked by vertical lines at frames per vibration period of $1/(ft_s)= 31.4$ and 94.2 for velocities of $v_{max}/|v_{Nyq}|= 5$ and 15 respectively, below which no further

calculations were performed. The maximum error from the simulation and the value predicted theoretically by equation **(4-12)** agree well.

Figure 4.26 shows the effect of exposure on the maximum normalized velocity error for $v_{max}/|vN_{yq}|=3$, comparable to the maximum normalized velocity achieved experimentally. Figure 4.26(a) shows that the four frame algorithm is not sensitive to the exposure time, because the phase is calculated within a single frame. However, both the single-step algorithm and compensating single-step algorithm show significant errors for an exposure of $t_e/t_s=0.1$, used experimentally. The predicted maximum normalized velocity error at $1/(ft_s)=38.6$ (i.e. camera frame rate 20 kHz and object vibration frequency 518 Hz) is approximately 0.3. Errors due to the exposure are larger than the other error sources considered.

Figure 4.27 shows the effect of intensity noise on the maximum normalized velocity error for $v_{max}/|vN_{yq}|=3$. Zero-mean, Gaussian-distributed noise up to a maximum of 3 bits (seven grey levels) was added to the calculated speckle interferograms prior to phase calculation. The intensity values less than or greater than the limiting values (0 and 255 grey levels) were set to the respective limit. The maximum intensity noise is equal to the maximum experimentally recorded intensity difference between corresponding pixels (shifted by one row to compensate for the $\pi/2$ radian phase step). The four-frame algorithm is less sensitive to intensity noise than the single frame algorithms, because twice the number of images is used. The error level is comparable with those seen at low surface velocities, approximately $0.1v_{Nyq}$, where the errors due to the long exposure are a minimum.

Figure 4.28 shows the effect of phase step error on the maximum normalized velocity error for $v_{max}/|v_{Nyq}|=3$. In this case, the velocity errors for both the four-frame and single-step algorithms are the same. However, the compensating single-step algorithm is immune to phase step errors because it is based on the actual phase step at each pixel.

4.5 Discussion

The experimental results again demonstrated the flexibility of the CMOS detector to record time-averaged subtraction fringes, from which a ROI was identified that covered the two diffracted orders for spatial phase stepping. There was no need to change

between detectors to make the two types of measurement, and it was straightforward to identify the corresponding position of the ROIs on the time-averaged subtraction fringe pattern.

Spatial phase stepping was implemented with a binary phase grating for the first time, enabling the maximum spatial resolution to be obtained for the system. Spatial phase stepping immediately doubles the potential maximum surface velocity and eliminates the errors associated with the local linear velocity approximation made in inter-frame phase step SPI, but at the expense of a more complicated experimental system.

The performance of the spatial phase stepped system was compared to inter-frame phase stepping for surface velocities up to $0.5v_{Nyq}$. At low surface velocities, a maximum difference between the two measurements of $0.1v_{Nyq}$ was observed, attributed mainly to intensity noise and phase step errors due to imperfect image separation between the diffracted images. These errors were reduced by the introduction of a new compensating single-step spatial phase stepping algorithm. The inter-frame phase stepped analysis failed at approximately $0.3v_{Nyq}$, as seen in the previous chapter. Spatial phase stepping continued to work successfully up to the Nyquist limit.

High-speed sub-Nyquist interferometry was implemented for the first time to measure normalised velocity (modulo 2π) beyond the Nyquist velocity limit. At higher velocities, the exposure became the dominant factor restricting the accuracy of the measured phase, and the highest surface velocity achieved with continuous wave illumination was approximately $\pm 3.0v_{Nyq}$. However, this range represents an order of magnitude extension compared to the inter-frame phase stepped system, and could be significantly further increased with the use of a pulsed laser to restrict the exposure period further.

The normalized velocity error plots against surface velocity and number of frames per vibration period show the first systematic error analysis for spatial phase stepped SPI acting as a multipoint vibrometer beyond the Nyquist limit. The analysis in terms of normalized surface velocity introduced in Chapter 3 for inter-frame phase stepping could be extended to the spatial phase-stepped case. The numerical simulation and theoretical evaluation of these errors were found to be in good agreement. It provides

the possibility to set a vibration velocity and frequency limit for the maximum camera frame rate in order to restrict errors to within a certain threshold.

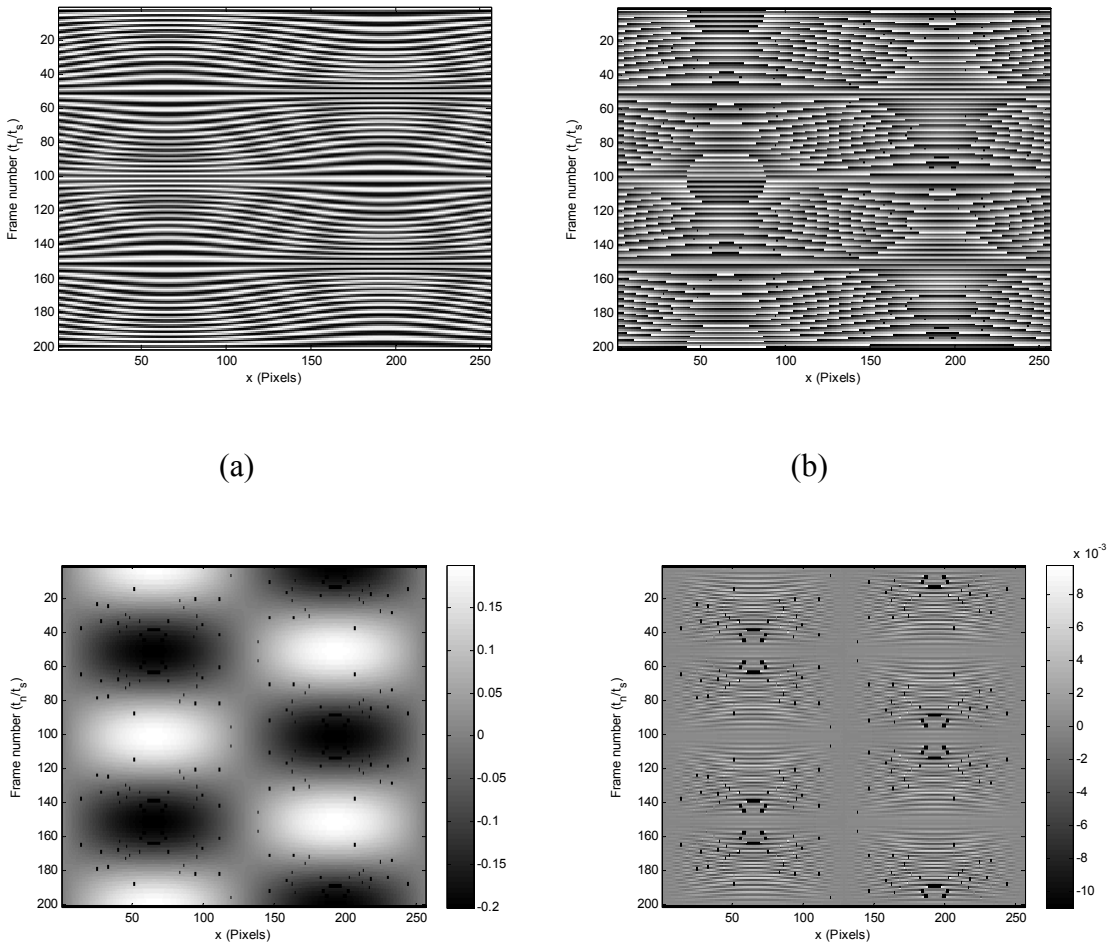

Figure 4.1 Simulation of inter-frame phase stepped SPI, with random speckle phase suppressed. Vibration amplitude 0.2 v_{Nyq}. (a) Intensity (I_n); (b) Wrapped phase (I_O-I_R); (c) Normalized velocity ($\Delta\Phi/\pi$); (d) Error in normalized velocity.

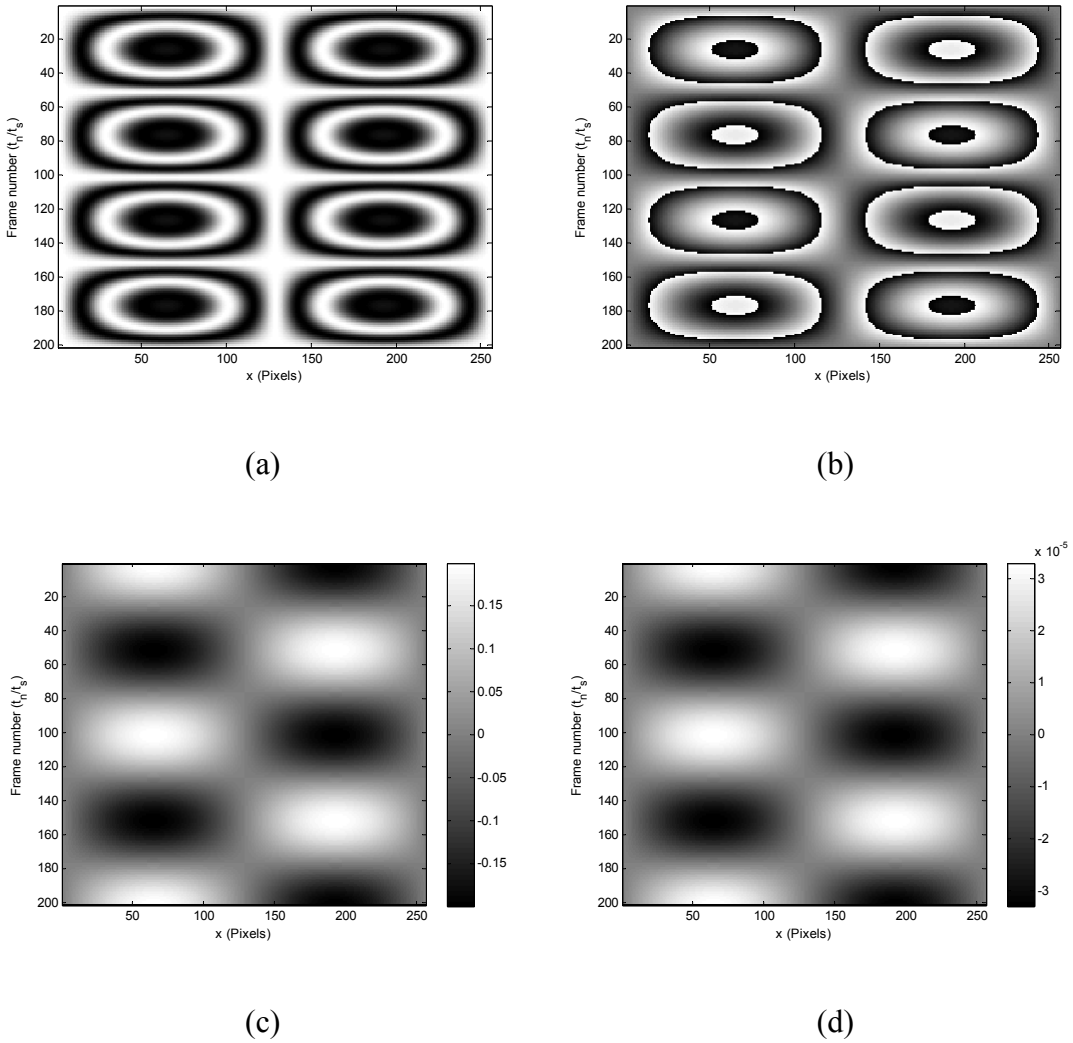

Figure 4.2 Simulation of spatial phase stepped SPI, with random speckle phase suppressed: N=4, vibration amplitude $0.2v_{Nyq}$. (a) Intensity (I_n); (b) Wrapped phase (I_O-I_R); (c) Normalized velocity ($\Delta\Phi/\pi$); (d) Error in normalized velocity.

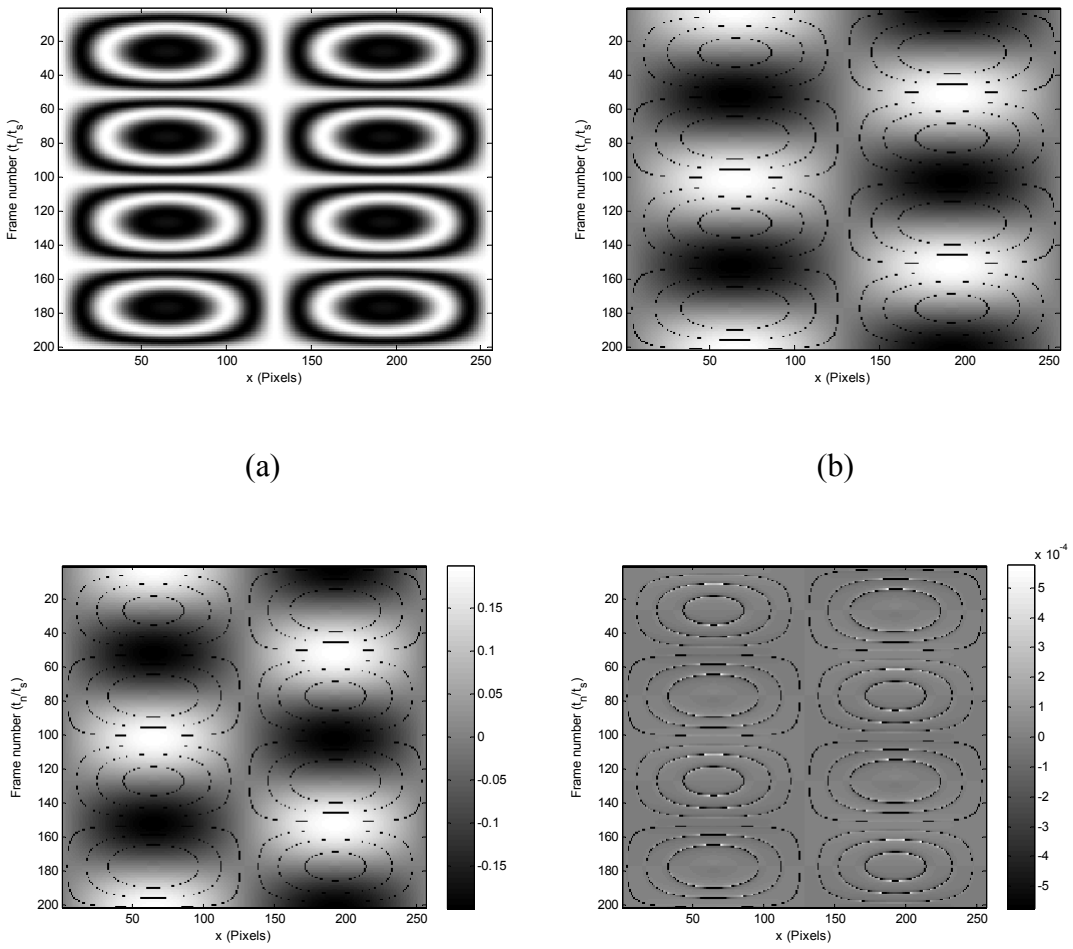

Figure 4.3 Simulation of spatial phase stepped SPI with random speckle phase suppressed: N=2, vibration amplitude $0.2v_{Nyq}$. (a) Intensity (I_n); (b) Phase difference (ΔI_O); (c) Normalized velocity ($\Delta\Phi/\pi$); (d) Error in normalized velocity.

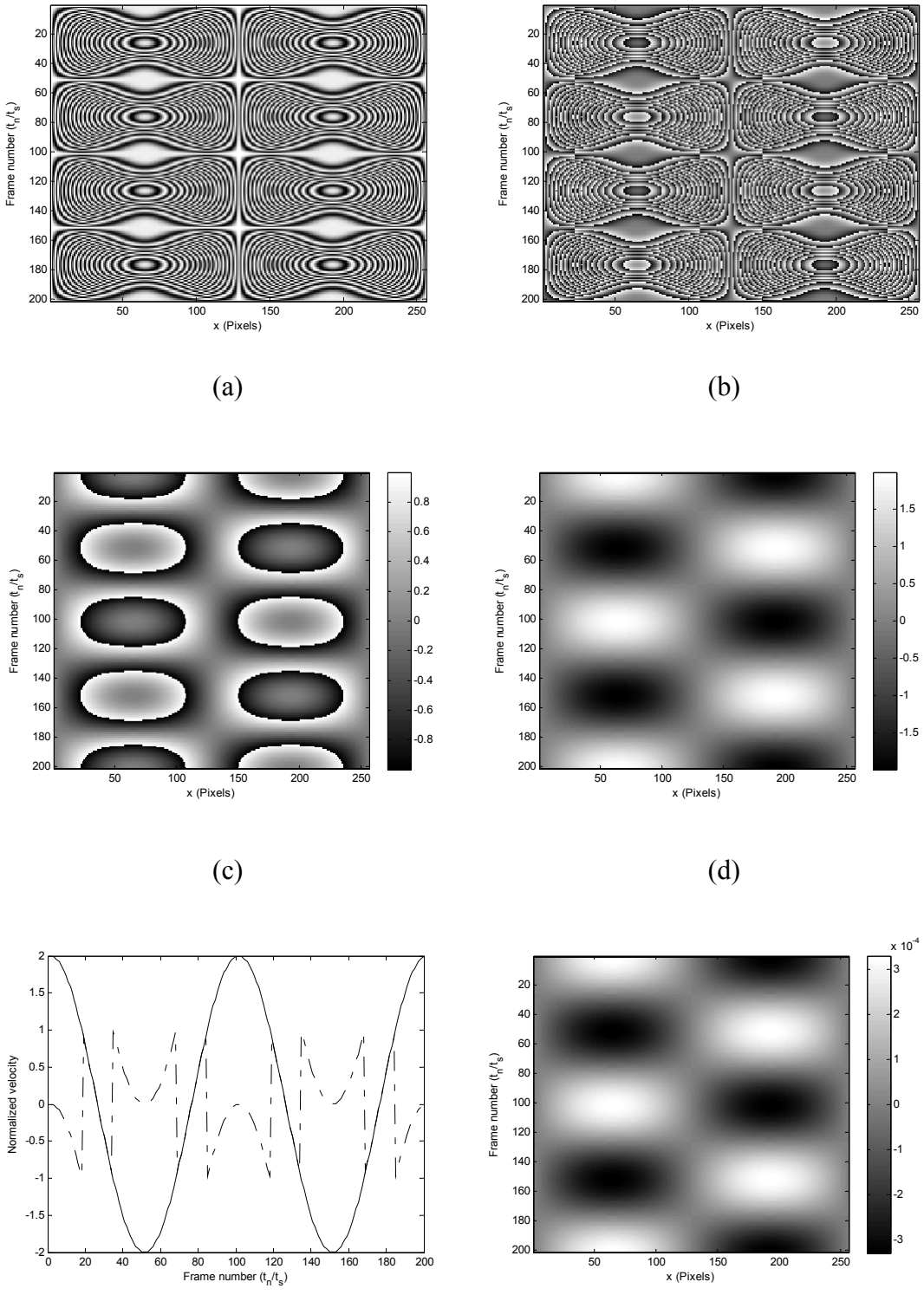

Figure 4.4 Simulation of spatial phase stepped SPI, with random speckle phase suppressed: N=4, vibration amplitude $2v_{Nyq}$. (a) Intensity (I_n); (b) Wrapped phase (I_O-I_R); (c) Normalized velocity ($\Delta\Phi/\pi$); (d) Unwrapped normalized velocity; (e) Wrapped and unwrapped normalized velocity for column 64; (f) Error in normalized velocity.

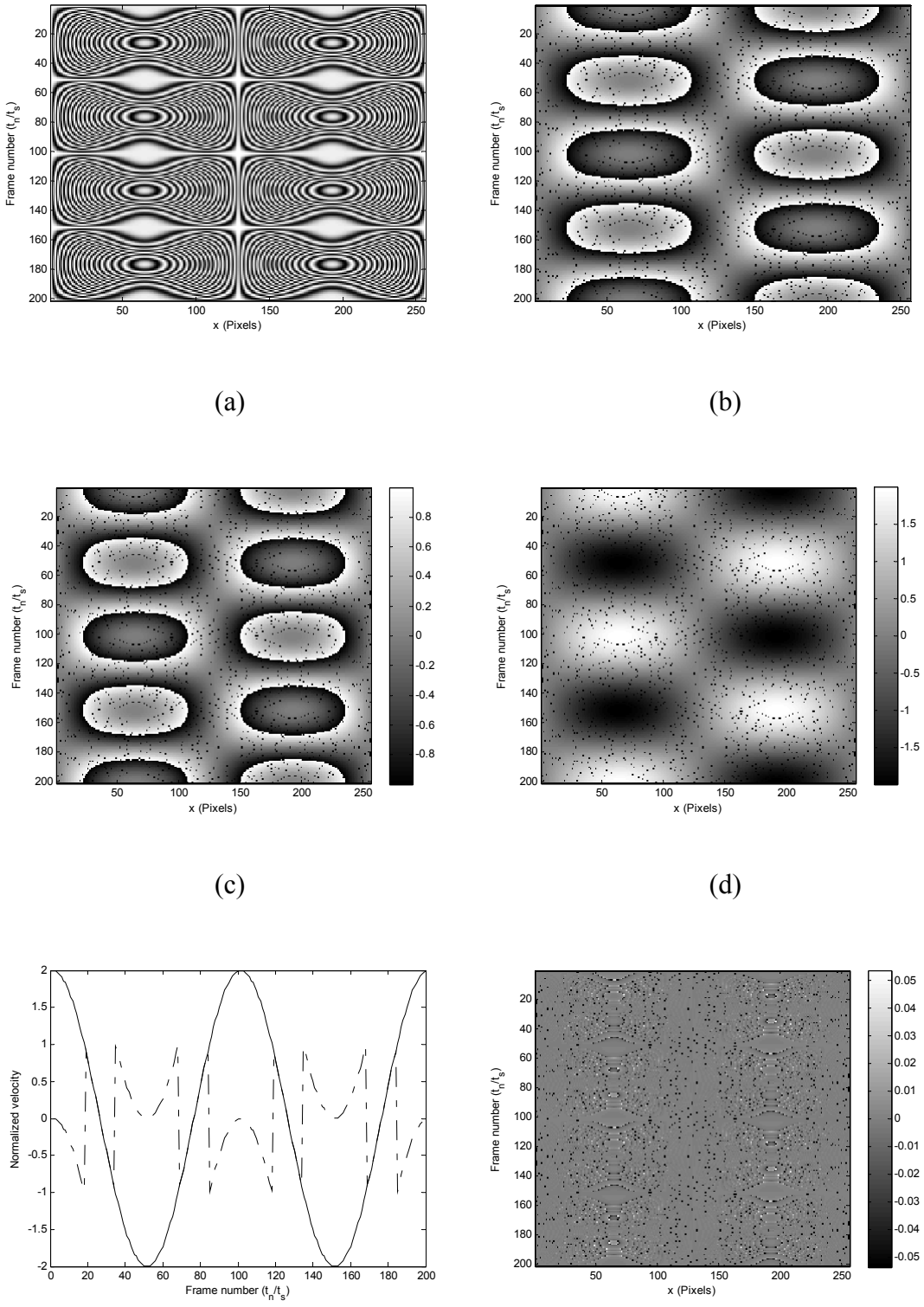

(a) (b)

(c) (d)

(e) (f)

Figure 4.5 Simulation of spatial phase stepped SPI with random speckle phase suppressed: N=2, vibration amplitude $2v_{Nyq}$. (a) Intensity (I_n); (b) Wrapped phase difference (ΔI_O); (c) Normalized velocity ($\Delta\Phi/\pi$); (d) Unwrapped normalized velocity; (e) Wrapped and unwrapped normalized velocity for column 64; (f) Error in normalized velocity.

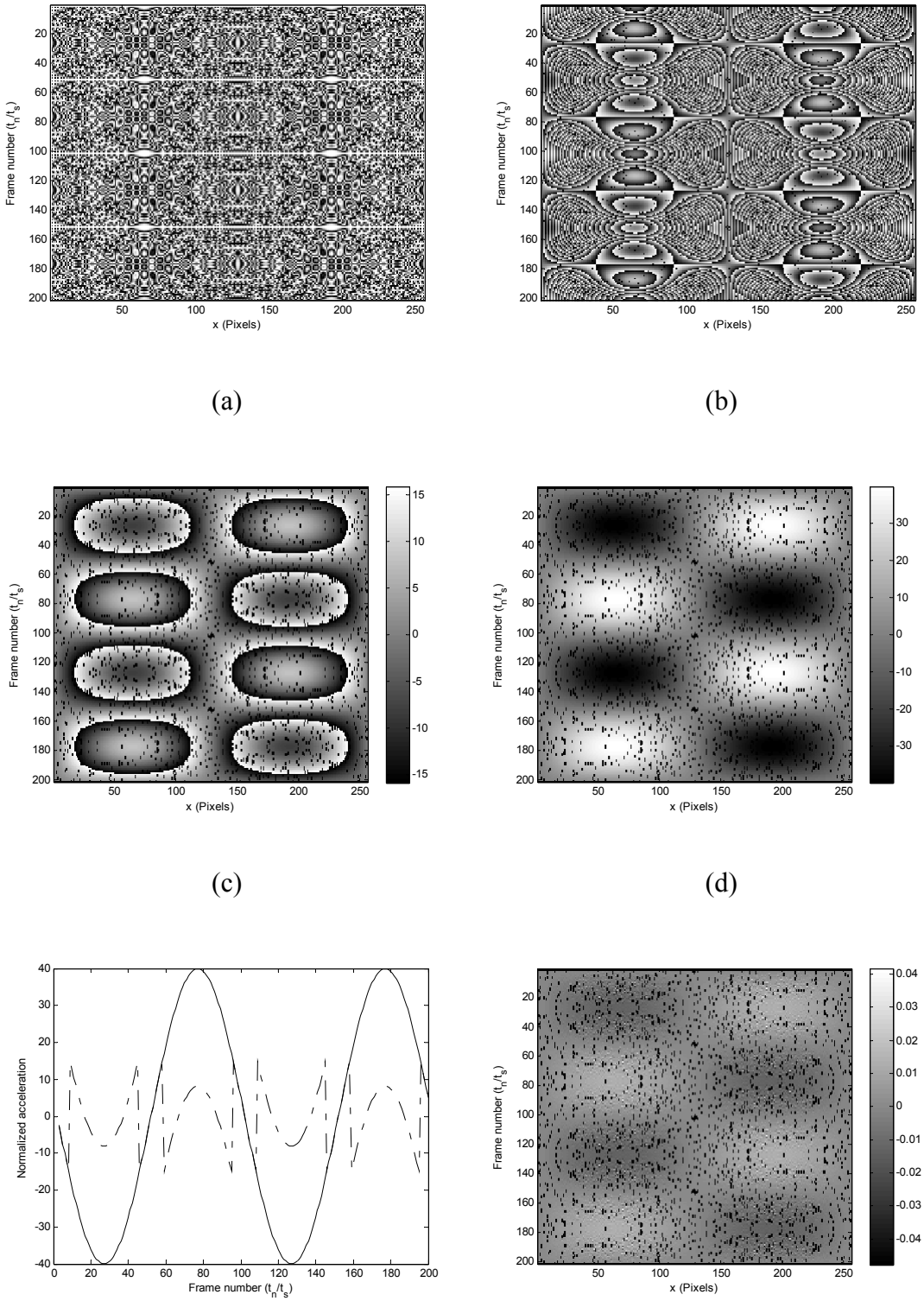

Figure 4.6 Simulation of spatial phase stepped SPI with random speckle phase suppressed: N=2, vibration amplitude $40v_{Nyq}$. (a) Intensity (I_n); (b) Wrapped phase difference (ΔI_O); (c) Normalized acceleration ($\Delta\Phi/(2\pi^2 ft_s)$); (d) Unwrapped normalized acceleration; (e) Wrapped and unwrapped normalized acceleration for column 64; (f) Error in normalized acceleration.

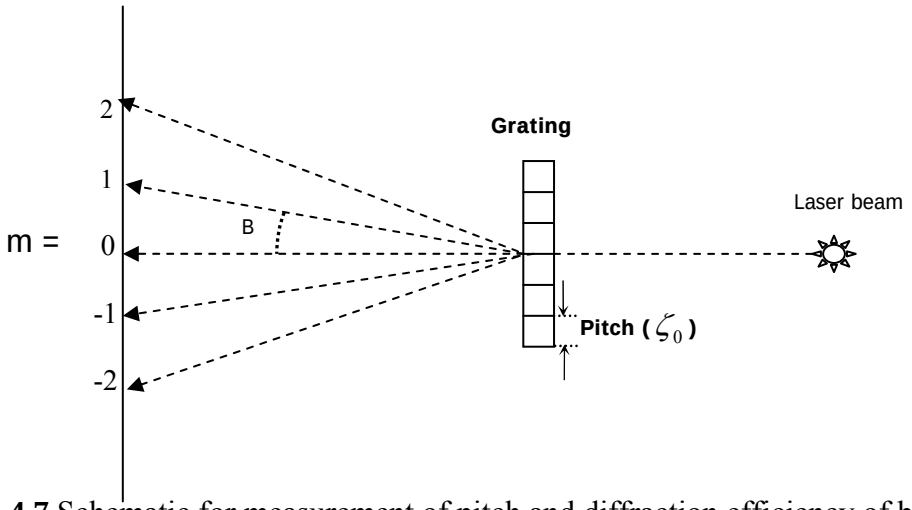

Figure 4.7 Schematic for measurement of pitch and diffraction efficiency of binary phase gratings.

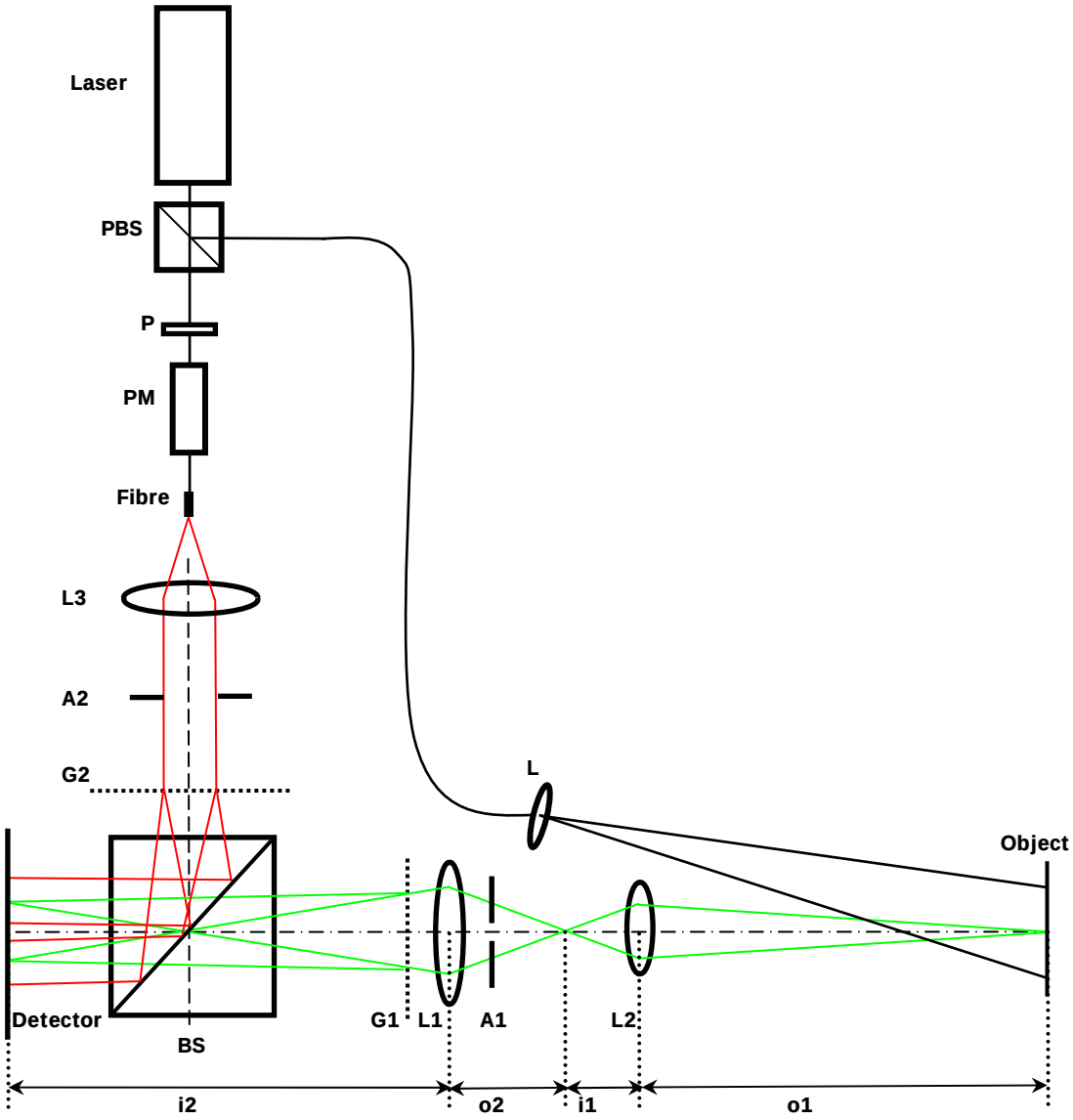

Figure 4.8 Schematic of spatial phase-stepped SPI setup. G – Binary phase grating; A – Aperture.

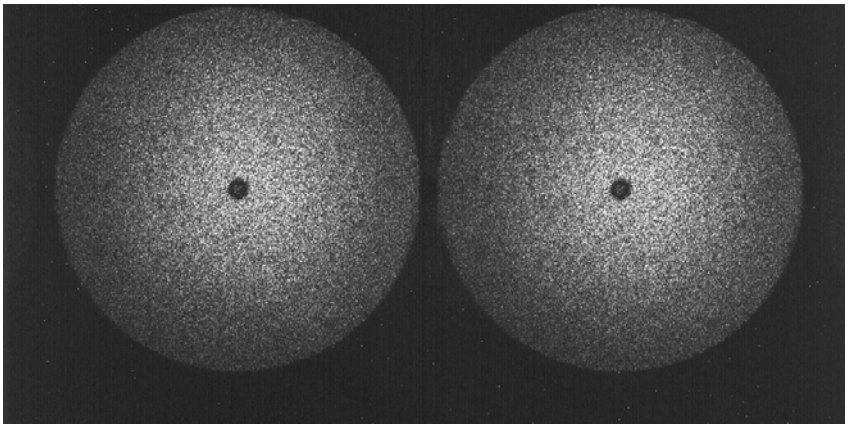

Figure 4.9 Image of a plate spatially separated by binary grating G1.

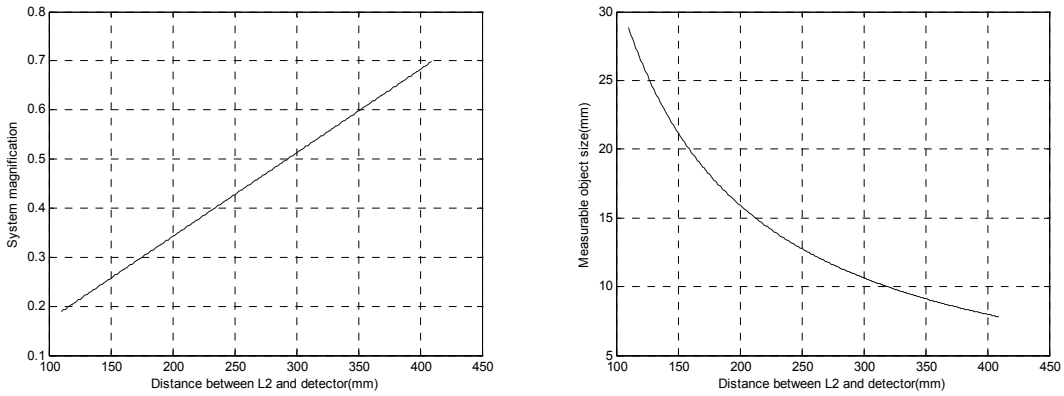

(a) (b)

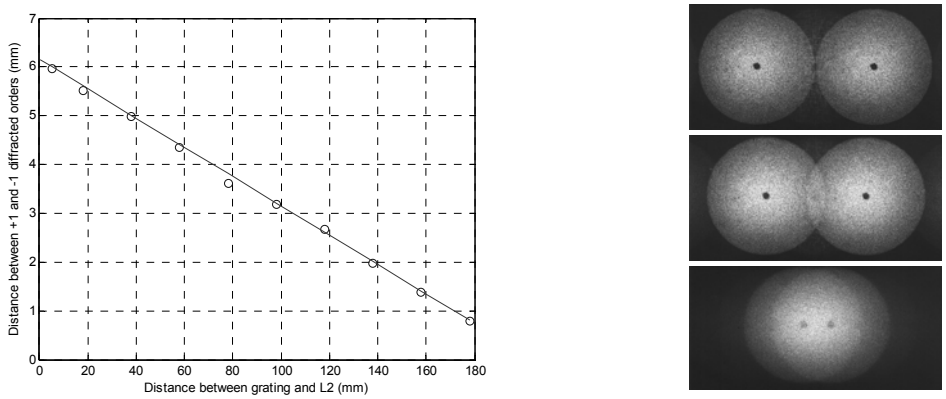

(c) (d)

Figure 4.10 Magnification of the imaging system

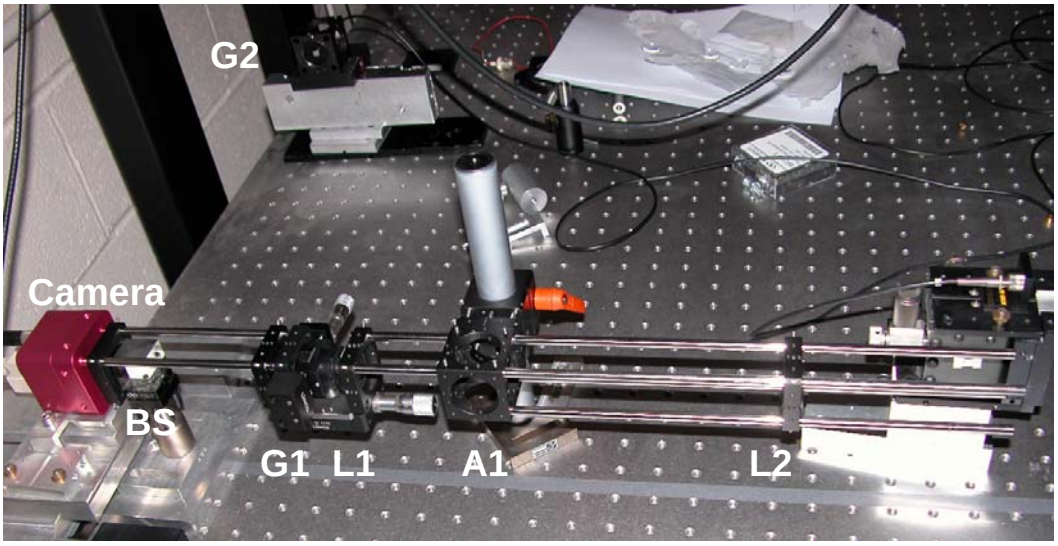

(a)

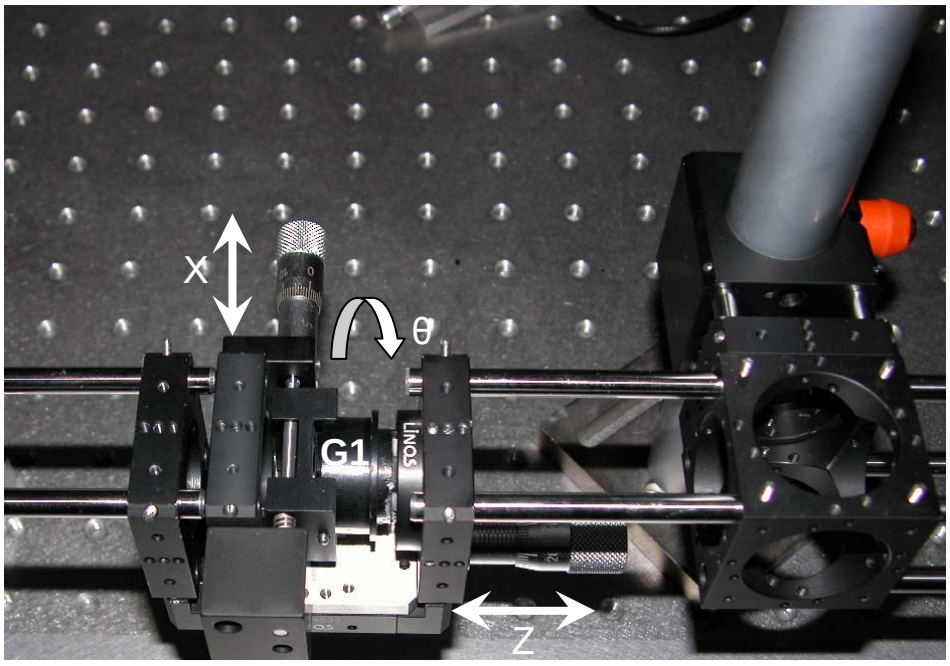

(b)

Figure 4.11 (a) Photo of spatial phase step system. (b) Close-up of object beam grating, showing axes of position control.

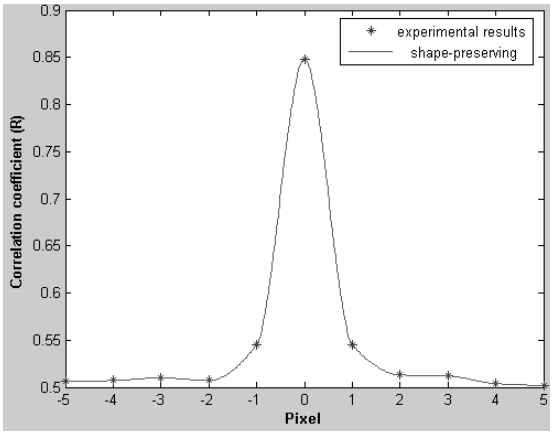

Figure 4.12 Correlation coefficient of two diffracted orders.

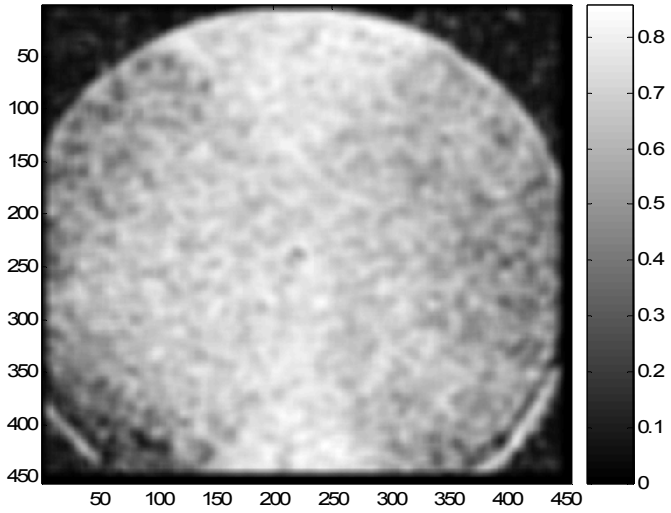

Figure 4.13 2-D map of correlation coefficients of two diffracted order.

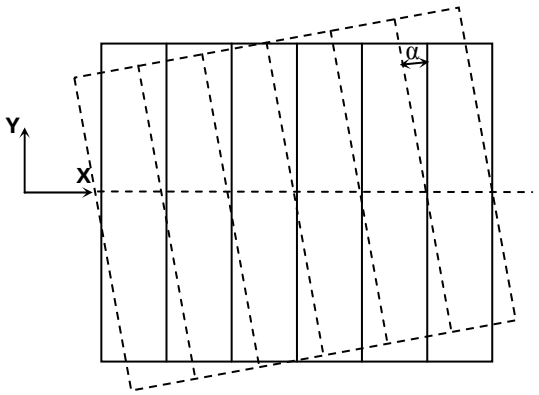

Figure 4.14 Schematic of relative rotation between the object and reference gratings.

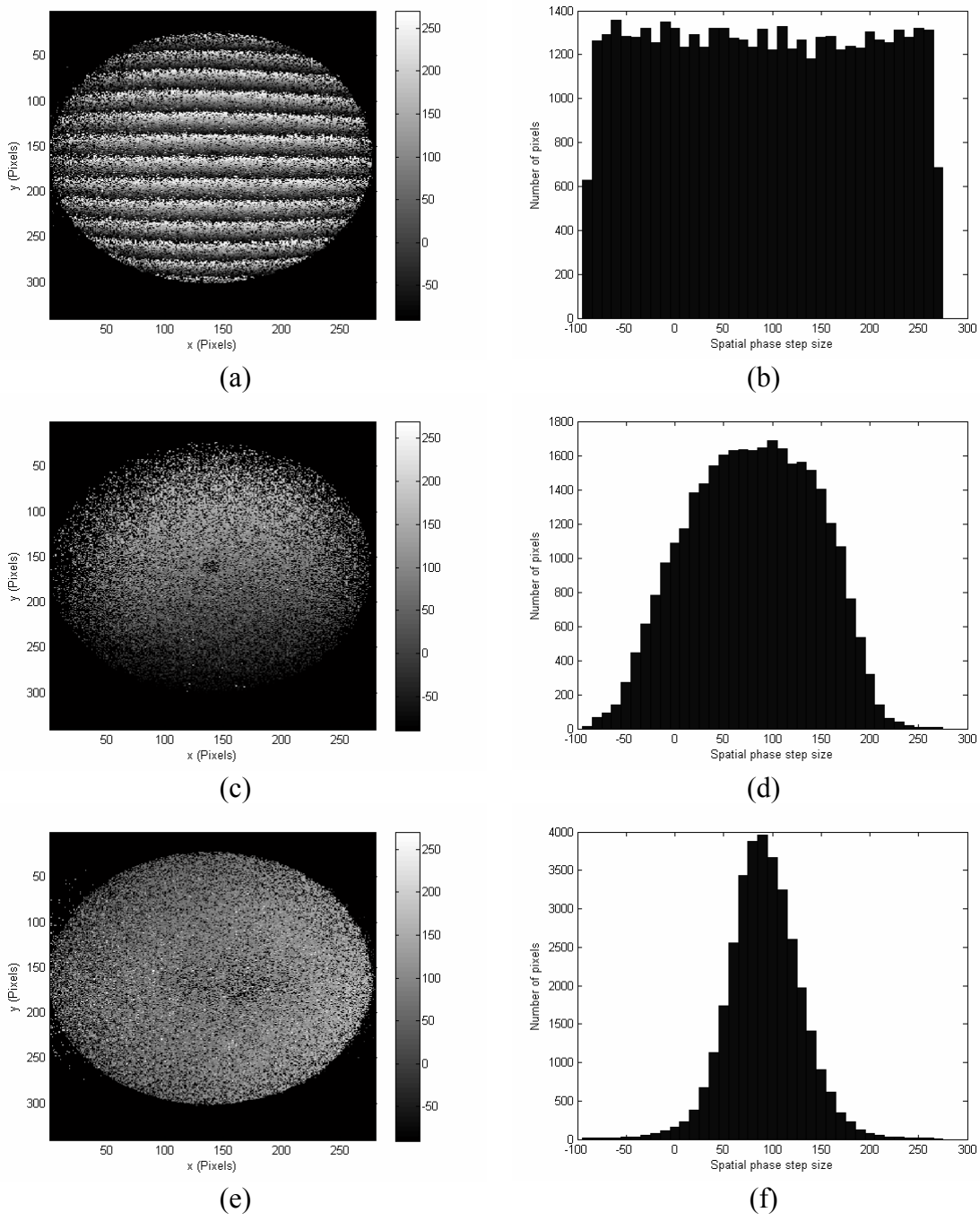

Figure 4.15 (a), (c), (e) Wrapped phase maps and (b), (d), (f) histograms of the phase difference between the two diffracted orders, with decreasing relative rotation between two gratings.

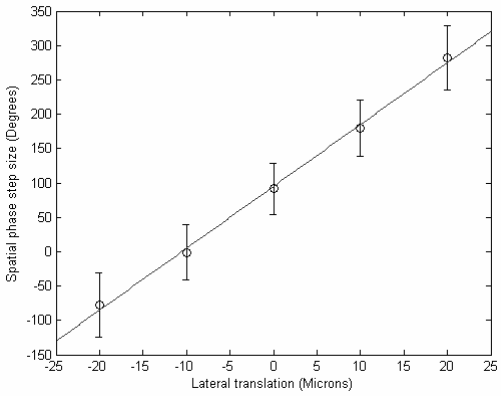

Figure 4.16 Calibration of spatial phase-step size using inter-frame phase-stepping. Mean phase step over all pixels in image plotted against lateral x-translation of reference grating. Error bars show plus / minus three standard deviations.

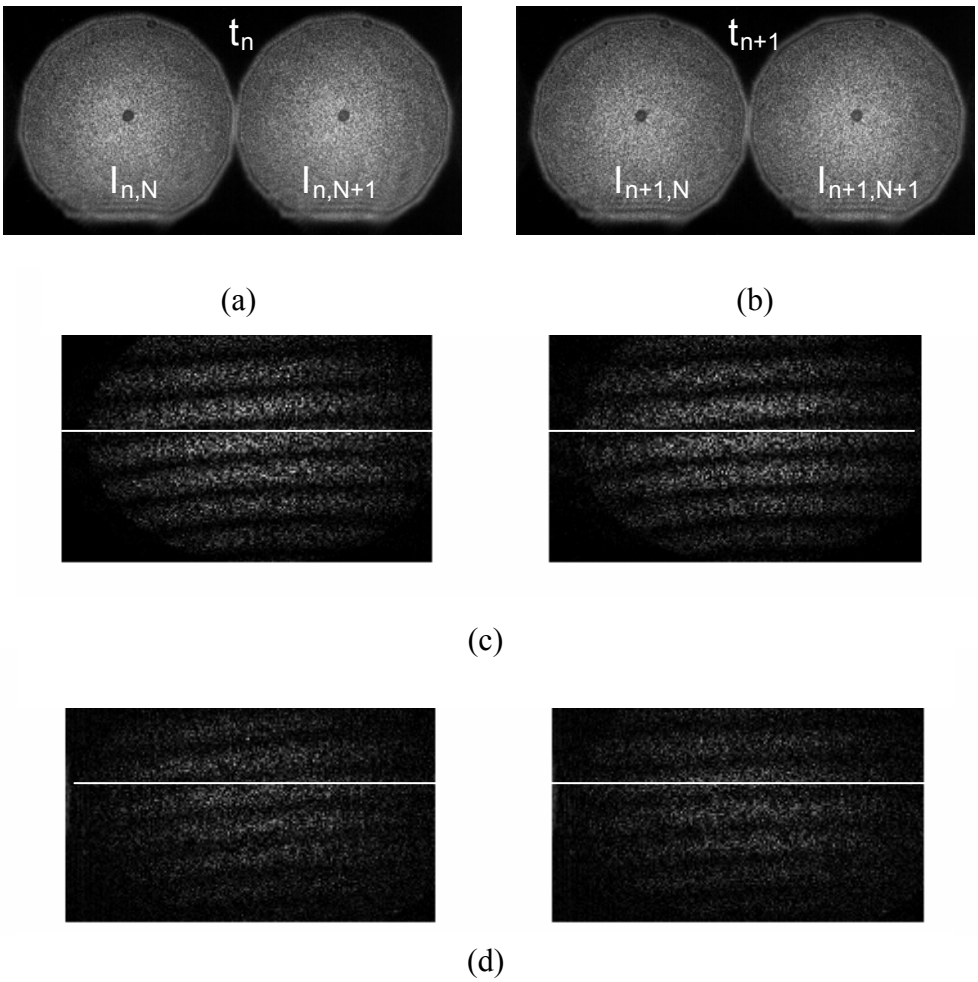

Figure 4.17 Spatial phase stepped results recorded for out-of-plane deformation of a test surface. Phase referenced speckle patterns (a) at t_n 'before deformation' $I_{n,N}(x,y,t_n)$ and $I_{n,N+1}(x,y,t_n)$ and (b) t_{n+1} 'after deformation' $I_{n+1,N}(x,y,t_{n+1})$ and $I_{n+1,N+1}(x,y,t_{n+1})$. (c) Subtraction correlation fringes ($I_{n+1,N}$ - $I_{n,N}$ and $I_{n+1,N+1}$ - $I_{n,N+1}$). (d) Cross-subtraction correlation fringes ($I_{n+1,N}$ - $I_{n,N+1}$ and $I_{n+1,N+1}$ - $I_{n,N}$).

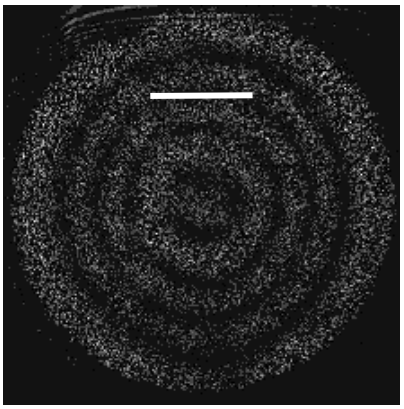

Figure 4.18: Time-averaged subtraction fringe pattern recorded at 25 frames per second showing the target vibrating at 518 Hz. The horizontal ROI was interrogated at 20 kHz, corresponding to a maximum normalized velocity of 0.3 (maximum surface velocity of 1.25 mm/s, λ=532 nm and η=2).

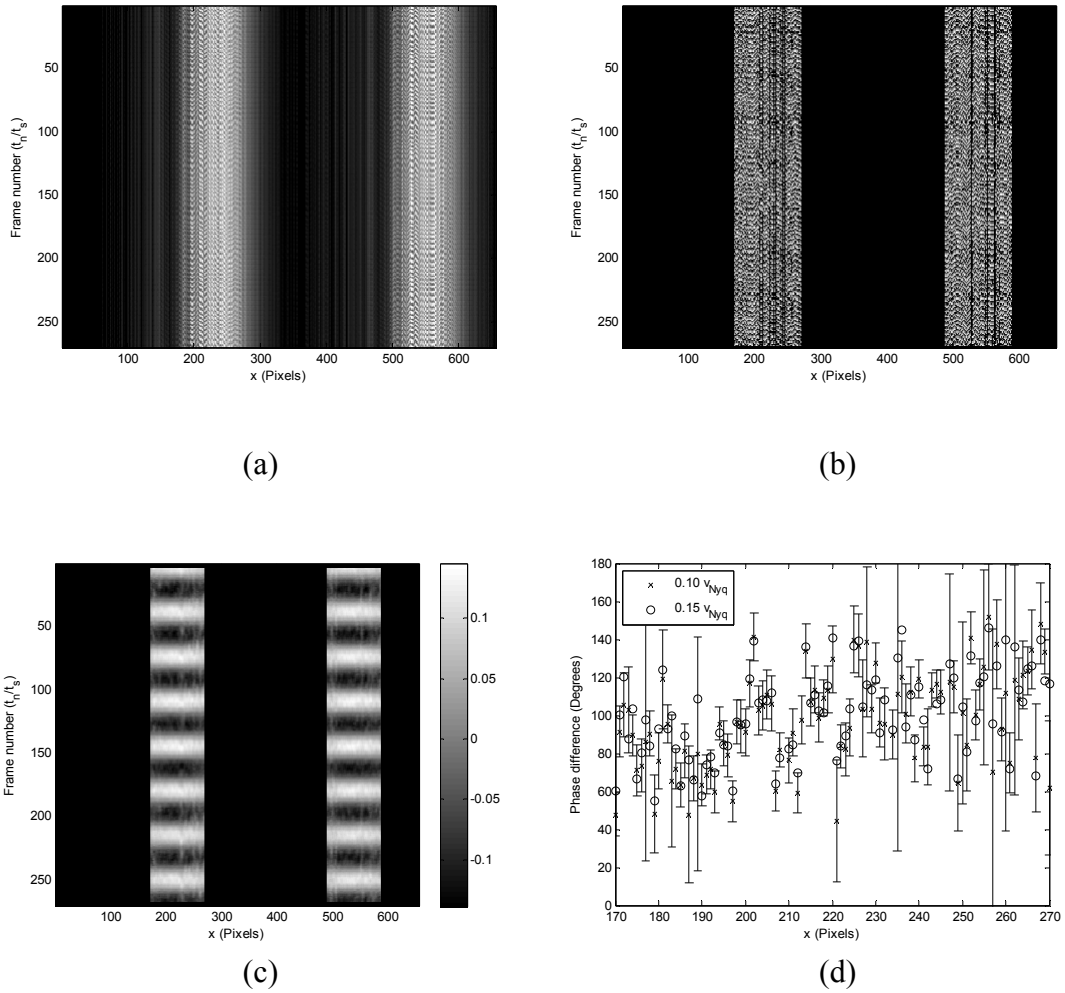

Figure 4.19: (a) Spatio-temporal speckle pattern showing intensity variation for the horizontal ROI (656 × 1 pixels) recorded at 20 kHz for object vibrating harmonically at 518 Hz. Nominal maximum surface velocity $0.1v_{Nyq.}$ (b) Phase from inter-frame phase step. (c) Normalized velocity, $\Delta\Phi/\pi$. (d) Mean phase difference between corresponding pixels (columns).

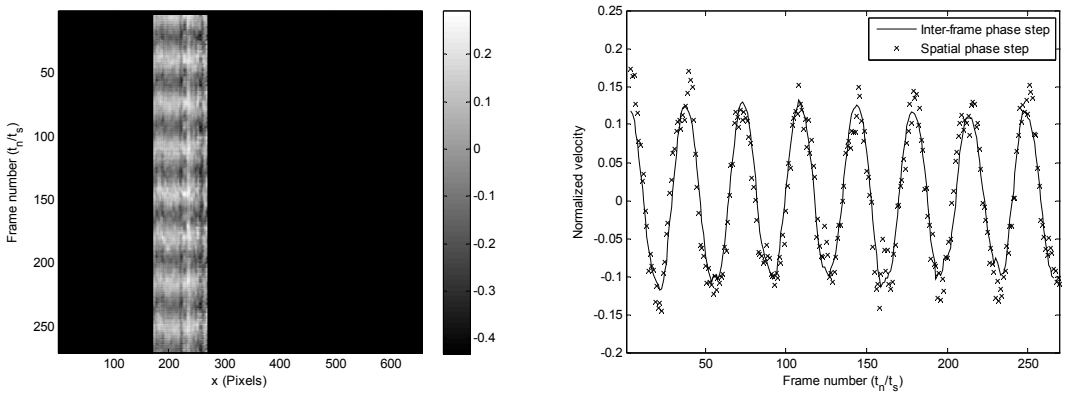

(a) (b)

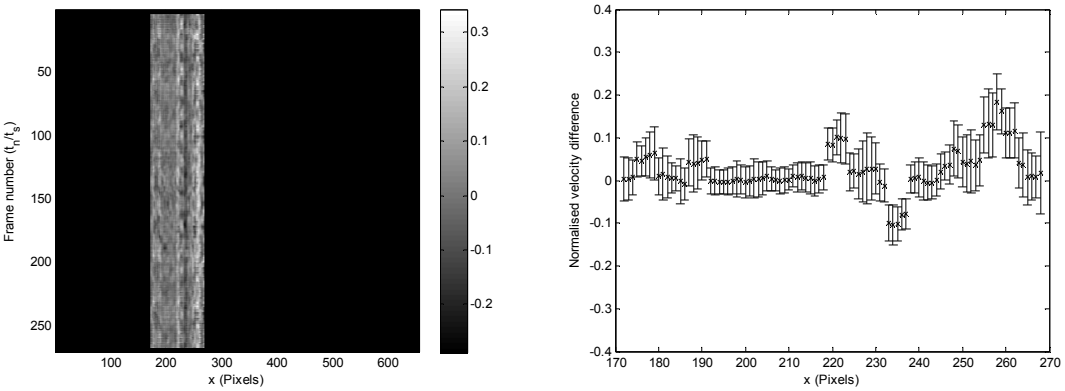

(c) (d)

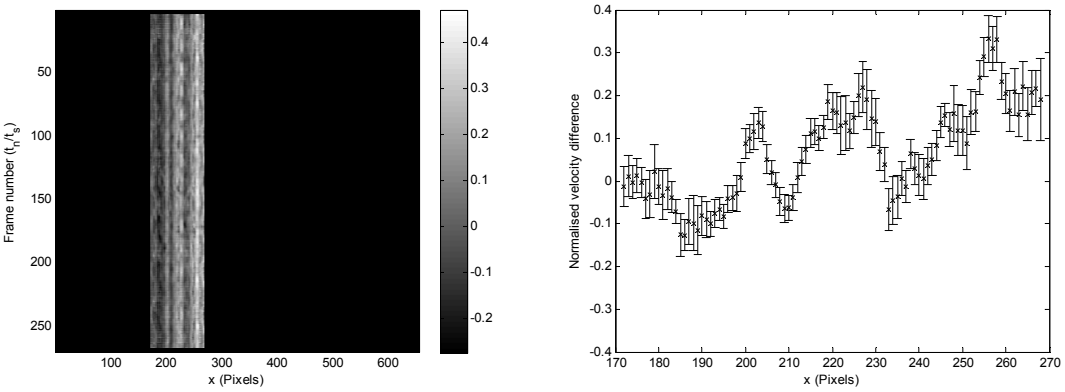

(e) (f)

Figure 4.20: Spatial phase step algorithm applied to inter-frame phase stepped data of Figure 4.19. Normalized velocity, $\Delta\Phi/\pi$, using compensating spatial phase step algorithm for (a) all columns and (b) column 207. Difference between normalized velocities from inter-frame and compensating spatial phase-stepped algorithms for (c) all columns and (d) column 207. Difference between inter-frame and standard spatial phase-stepped normalized velocities for (e) all columns and (f) column 207.

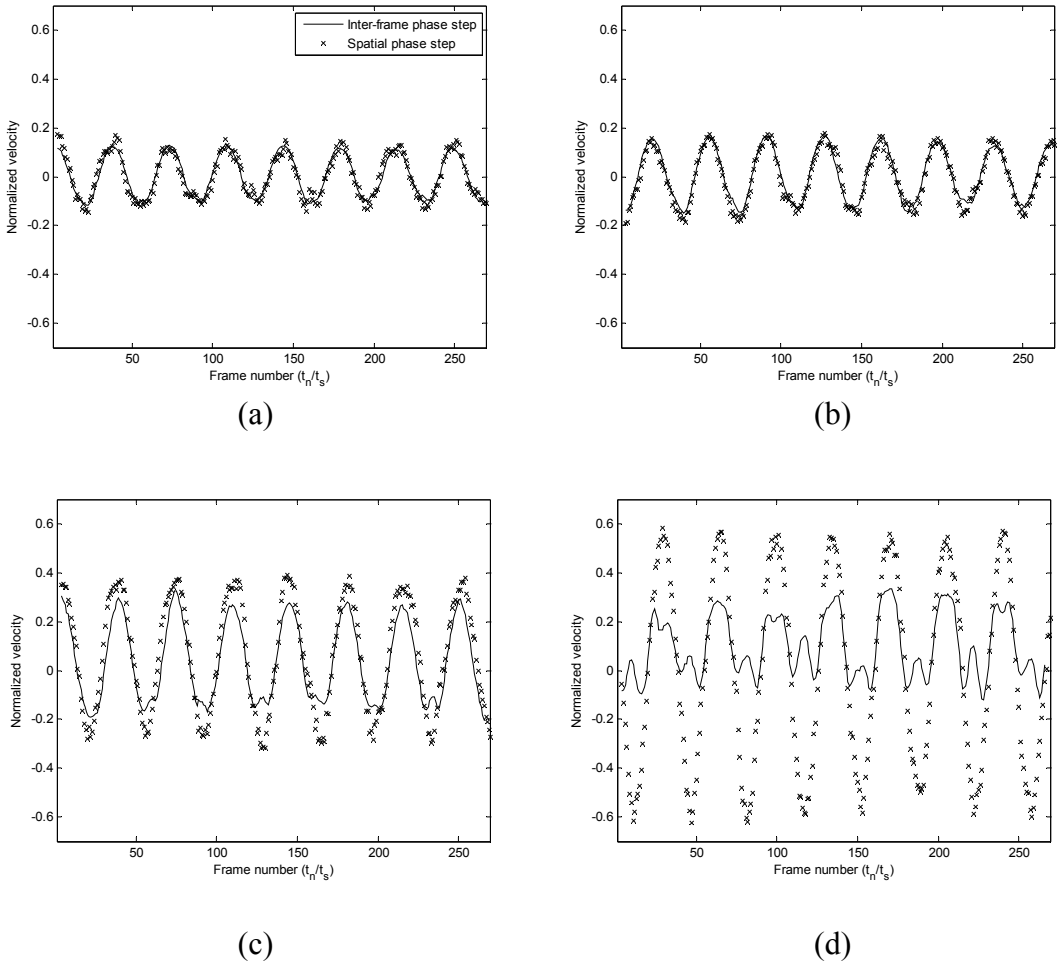

Figure 4.21: Normalized velocity, $\Delta\Phi/\pi$, calculated from inter-frame phase stepped data for column 207 at increasing nominal surface velocities of (a) $0.1v_{Nyq}$, (b) $0.15v_{Nyq}$, (c) $0.3v_{Nyq}$ and (d) $0.5v_{Nyq}$. Data in (a) correspond to Figure 4.19 and Figure 4.20.

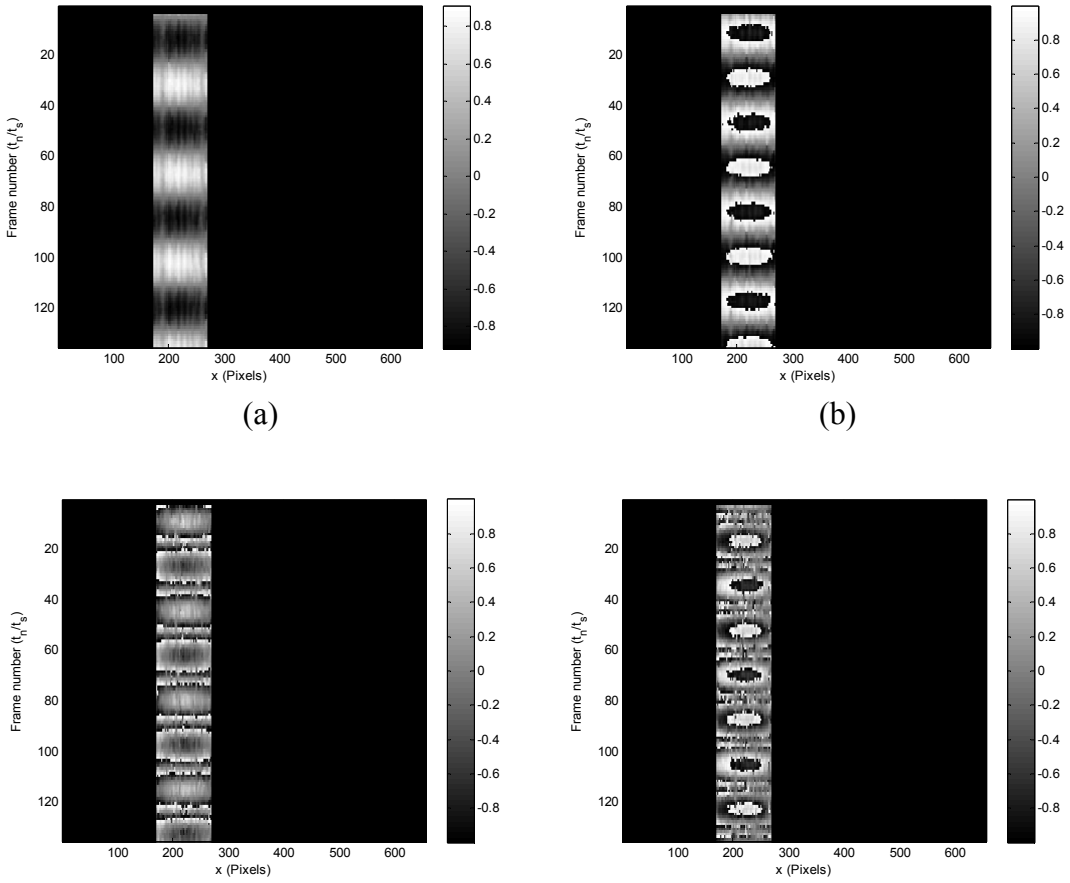

Figure 4.22: Normalized velocity, $\Delta\Phi/\pi$, calculated from spatial phase stepped data at increasing nominal surface velocities of (a) $0.84v_{Nyq}$, (b) $1.25v_{Nyq}$, (c) $2.0v_{Nyq}$ and (d) $3.0v_{Nyq}$.

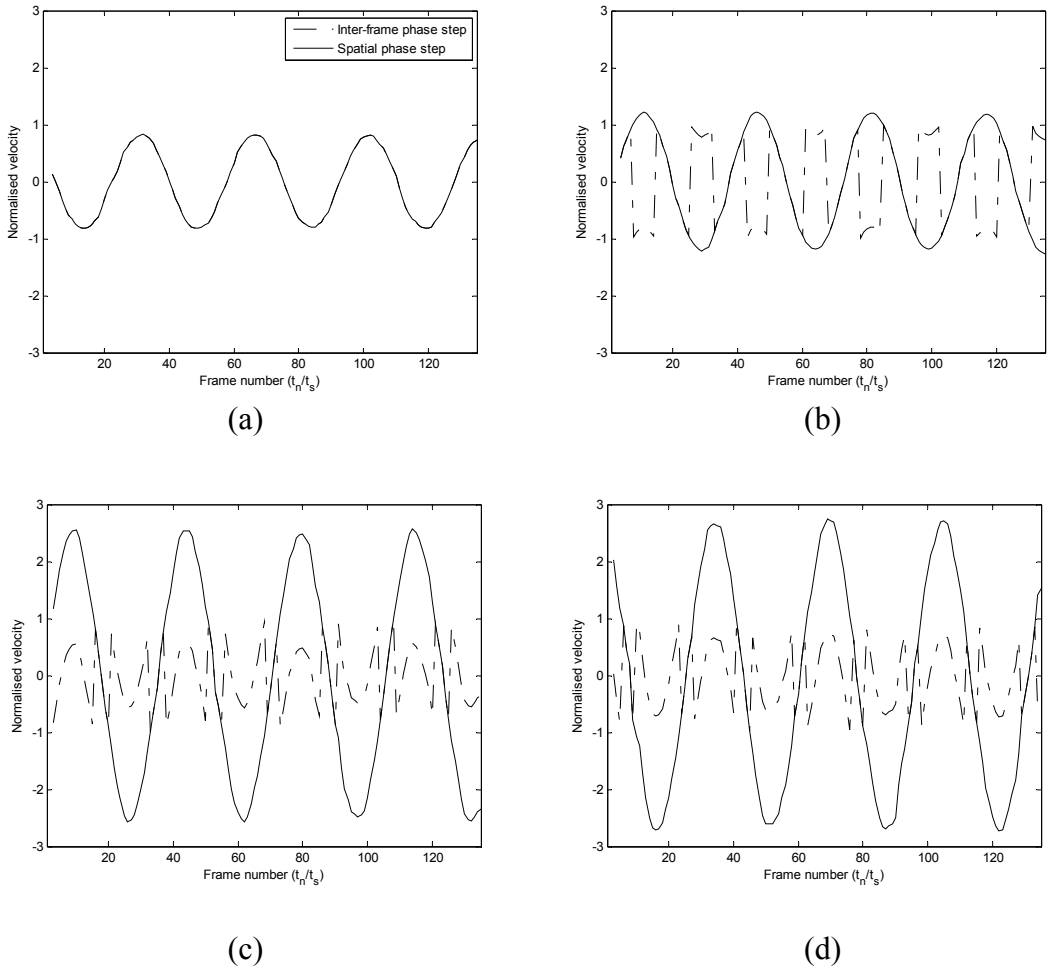

Figure 4.23: Normalized velocity, $\Delta\Phi/\pi$, calculated from spatial phase stepped data at increasing nominal surface velocities of (a) $0.84v_{Nyq}$, (b) $1.25v_{Nyq}$, (c) $2.0v_{Nyq}$ and (d) $3.0v_{Nyq}$. Column 229 for (a)-(c) and column 179 for (d).

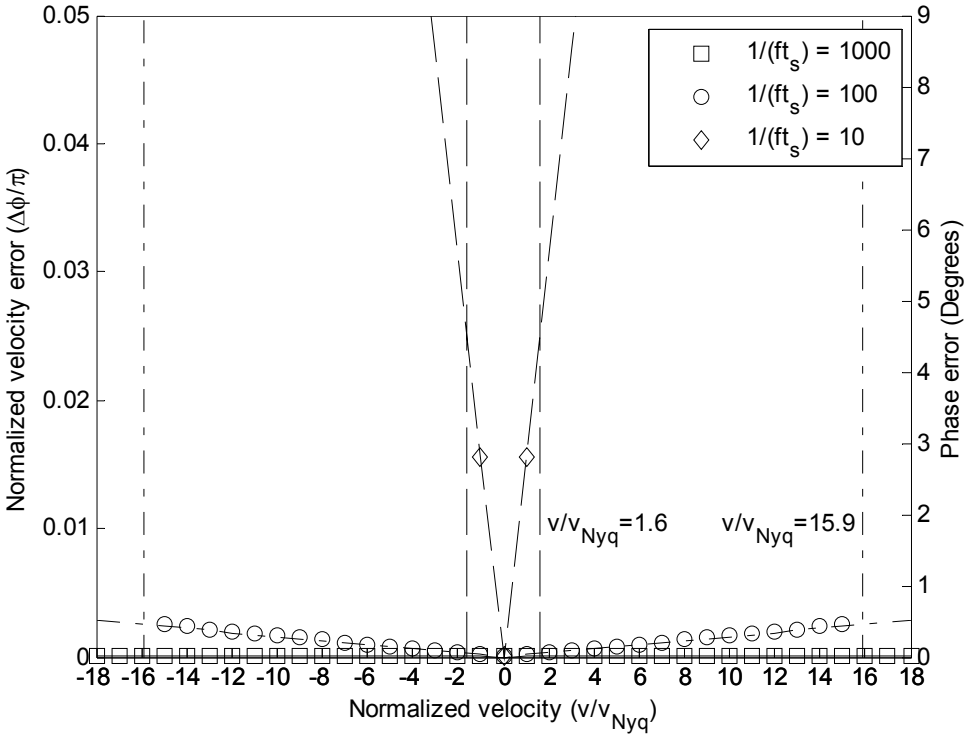

Figure 4.24: Maximum normalized velocity error plotted against normalized surface velocity for all algorithms (4-step, single step and compensating single step).

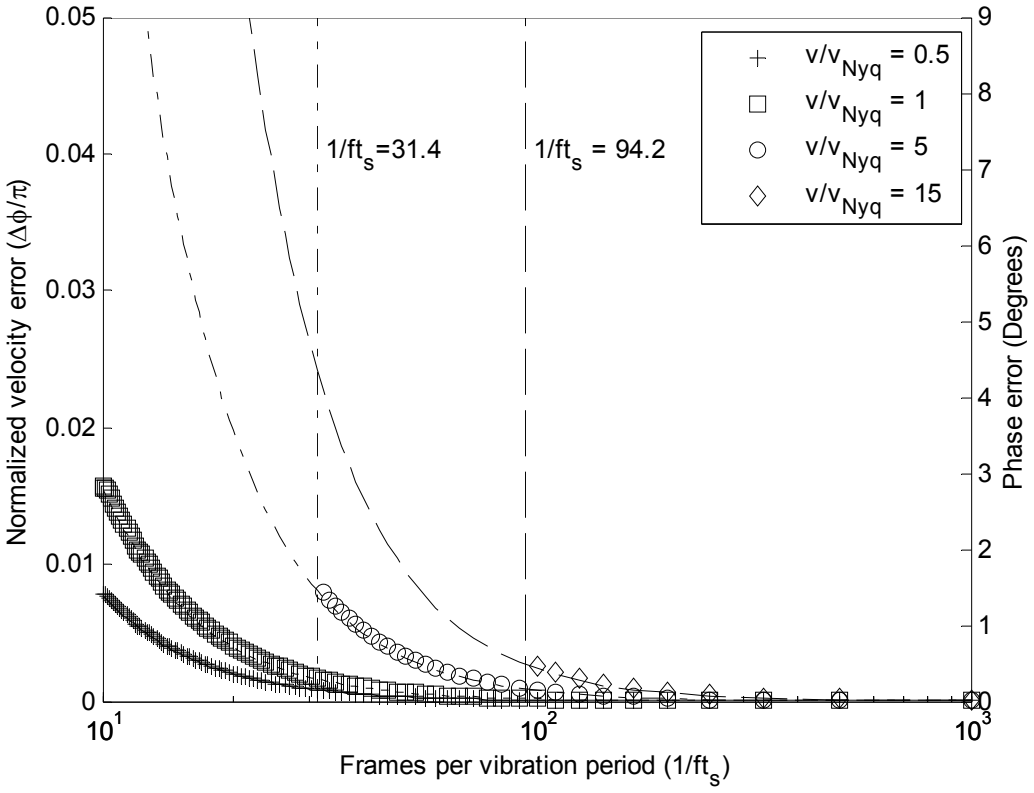

Figure 4.25: Maximum normalized velocity error plotted against the number of frames per vibration period for all algorithms (4-step, single step and compensating single step). Influence of maximum normalized surface velocity.

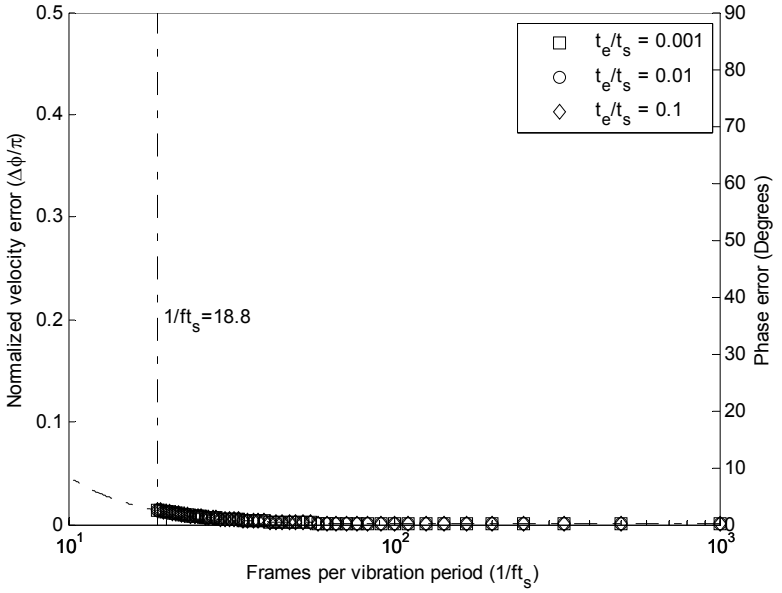

(a)

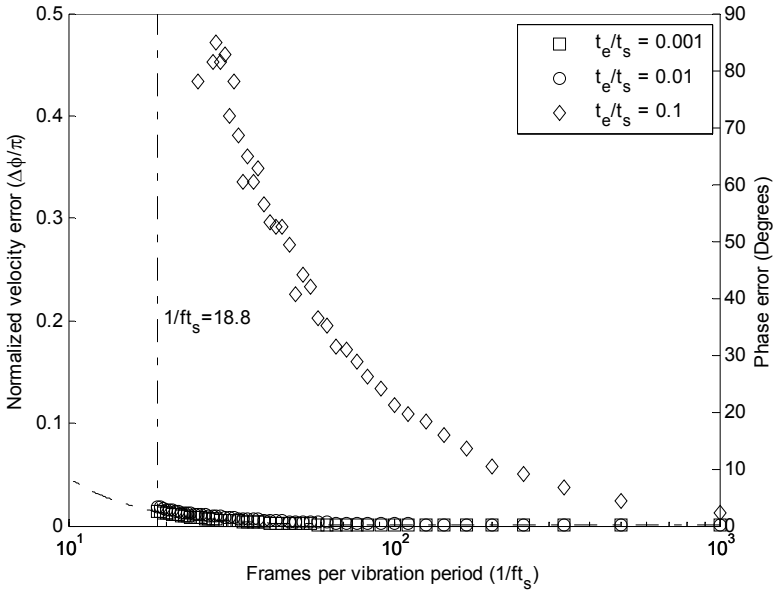

(b)

Figure 4.26: Maximum normalized velocity error plotted against number of frames per vibration period. (a) Four-frame algorithm and (b) single-step and compensating single-step algorithms. Influence of exposure time for $v_{max}/|v_{Nyq}| = 3$.

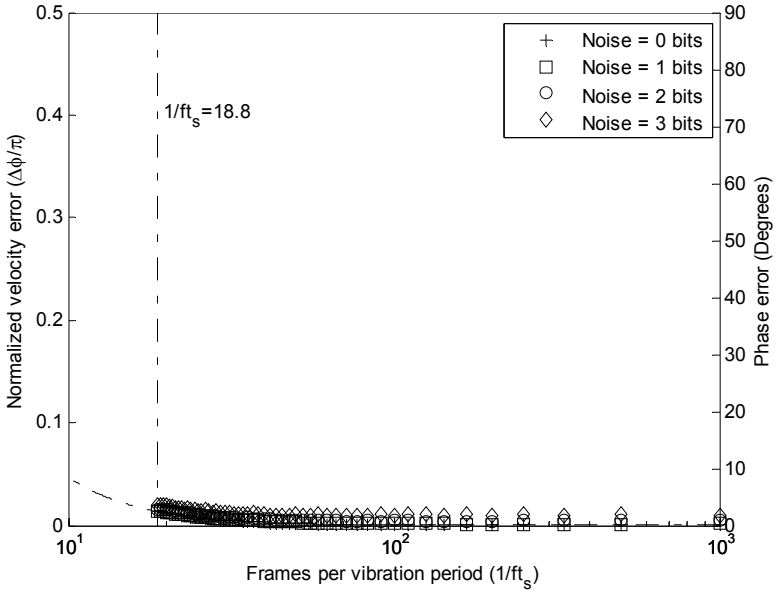

(a)

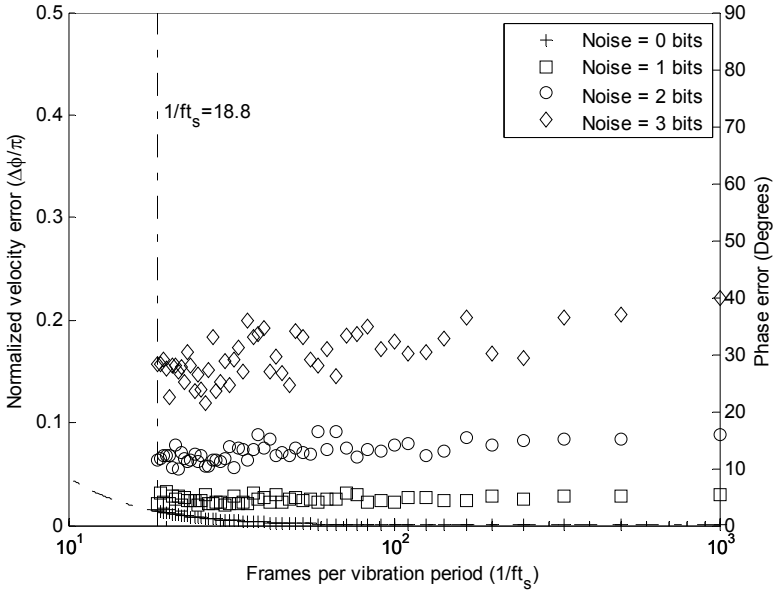

(b)

Figure 4.27: Maximum normalized velocity error plotted against number of frames per vibration period for (a) four-frame algorithm and (b) single-step and compensating single-step algorithms. Influence of intensity noise for $v_{max}/|v_{Nyq}| = 3$.

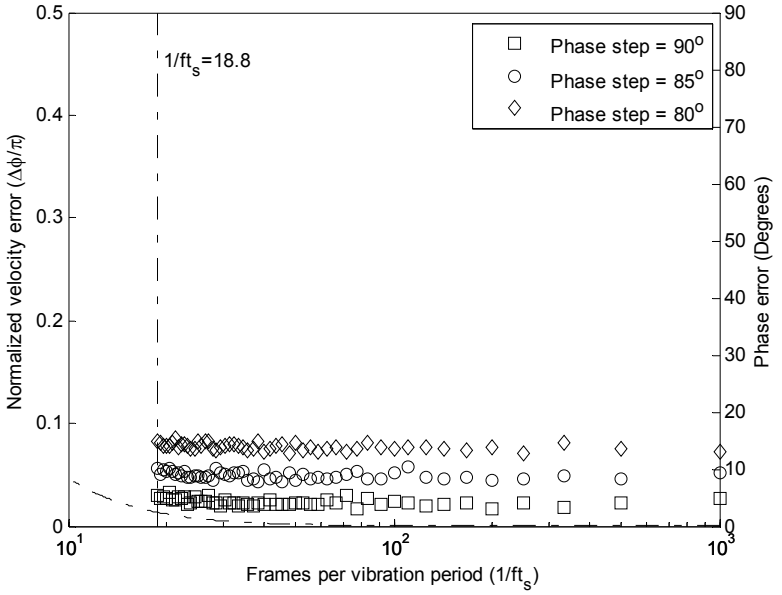

(a)

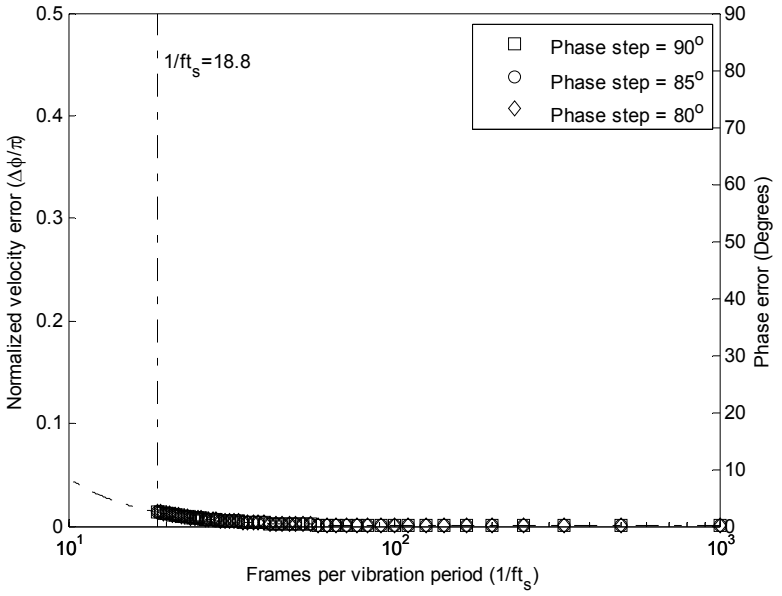

(b)

Figure 4.28: Maximum normalized velocity error plotted against number of frames per vibration period for (a) four-frame and single-step algorithms and (b) compensating single-step algorithm. Influence of phase step error for $v_{max}/|v_{Nyq}| = 3$.

5

Non-Linear CMOS Response

In this chapter the Linlog™ (Linear-logarithmic) response of the CMOS camera is applied in the inter-frame phase-stepped SPI system. The parameters of the camera Linlog mode are optimized. Then the characteristic response curve of the Linlog response is calibrated. Significant improvement of the experimental results under Linlog mode was obtained. The SPI system was applied to record the model response of an object of interest to AWE.

5.1 Application of Linlog response in SPI

In CMOS sensors, every pixel can be readout independently. The charge to voltage conversion is not done in one readout, but in every single pixel. Therefore, ROIs can be readout with high frame rate. The speed is only limited by the pixel clock of the sensor and the exposure time. The linear response of a CMOS detector has been used to record subtraction fringes for 128×128 pixels at 900 Hz, although no quantitative analysis was performed[86]. The nonlinear response of a CMOS detector has also been used to record subtraction fringes from an object with large brightness variations[87]. Again, no quantitative analysis was undertaken. In this chapter, the application of non-linear response of the CMOS detector in high-speed SPI will be investigated.

5.1.1 Introduction of Linlog response of CMOS camera

The Linlog mode of a CMOS camera (modal MV-D1024-80-CL, www.Photonfocus.com) was designed to take images with high contrast ratios. The function is based on logarithmic compression of the higher intensity levels in the response curve. The transition point between the linear and logarithmic response curves can be set by the user. However, a disadvantage of the Linlog mode is that a heavy compression of the intensity levels decreases the output range of the camera. Therefore, the settings of the camera must be carefully chosen for different images to enable the maximum output range to be used.

Under Linlog mode, three parameters need to be set: Two parameters are threshold values. The first value is called LL1 as seen in Figure 5.1, all grey levels above the first threshold will be fully compressed while the grey levels below that will not be affected. The manufacturer states that the lowest practically possible value for the first threshold is 174. Any values higher than 174 will no longer influence the characteristic curve significantly. But in the experiment sometimes values higher than 174 were chosen, because we still see some difference in the results and believed that sometimes a higher value may be more suitable for a individual case. A second threshold value is called LL2. It is used to define the transition point to separate a full compression from a combination of a linear and a logarithmic compression. LL1 and LL2 are implemented as 255-LL1 and 255-LL2, which means that increasing LL1 brings transition point down as shown in Figure 5.3. The value of the second threshold must be higher than the first threshold. The grey levels above second threshold will be fully compressed and the grey levels under the first threshold will not be affected. The grey levels between first and second threshold will be composed of an amount of the linear response and an amount of logarithmic response, the ratio is defined by the parameter COMP (percentage of strong compression) as shown in Figure 5.4.

The manufacturer does not provide an analytical expression that can be used to compute the Linlog response curve based on the values of LL1, LL2 and COMP. The manufacturer states that the response curve can not be calculated to a useful degree of accuracy by a simple analytical expression, because the Linlog response depends on a few factors:

- Integration time

- LL1 and LL2 values
- LL1 and LL2 time setting (COMP)
- Temperature (weakly)
- Frame rate (weakly)

Therefore it is necessary to obtain the response curve after the parameters are set and then invert the response curve to convert the intensities under Linlog mode back to the intensities under conventional linear response. The intensity could then be used to calculate phase of the object surface. Calibration of the response curve needs to be done every time after the optimal settings are found.

5.1.2 Calibration of non-linear CMOS response

To find out the best values of LL1, LL2 and COMP for an application, they were first set to LL1=LL2=COMP=0 for detecting any overexposed areas in the image. So the camera is effectively working under linear mode. Then the three parameters can be set by following the flow chart provided by the camera manufacturer as shown in Figure 5.5.

Firstly, a speckle pattern interferogram is recorded under LL1=LL2=COMP=0 as shown in Figure 5.6(a). It can be seen that some pixels in the middle of the interferogram are saturated while the pixels around the edge are still relatively dark, which is confirmed by its intensity histogram. Then LL1 is set to be 100, so the actual first transition level is 255-100=155 and grey levels above 155 are fully compressed. As seen in Figure 5.6(b) too many pixels are compressed: No pixel is saturated, but the dynamic range is poor. It can be seen in the histogram that output levels above 170 are not used. The value of LL1 is then changed to 80 so that the actual transition level is now 175. With a higher transition level, fewer bright pixels are compressed, but as seen in Figure 5.6(c), the compression is still too strong. The brighter pixels are compressed into a small range of grey levels, and still no pixel is saturated. To make the compression weaker, the COMP value is set to be 10, that means the pixels above 175 are now 10% compressed while 90% unaffected. It can be seen in Figure 5.6(d) that the dynamic range is improved, but some pixels become saturated because the COMP of 10% is low.

LL2 is then set to be 55 so that the second transition point is now 195. In this case, the pixels above 195 are 100% compressed, pixels between 175 and 195 are now 10% compressed and 90% unaffected while the pixels below 175 are unaffected. As seen in Figure 5.6(e) that the dynamic range is good ((full range of 0-255 is used) while few pixels are saturated. The whole procedure could be tedious because not only a single parameter needs to be determined but the perfect combination of the parameters needs to be found.

With the camera operating at 5 kHz and a ROI of 1 x 300 pixels, the parameters of LL1=80, LL2=55, COMP= 18 were chosen by following the procedure above. To find out the response curve of the settings, a laser beam was used as a reliable linear light input. It was proposed that the power of the laser beam is linear against the laser power output which can be read from the front panel of the laser controller. This was confirmed by measuring the laser beam intensity with a calibrated power meter with respect to different levels of laser power outputs between 0 and 500 mW. The laser beam directly shined onto the sensor. A sequence of images were acquired at different laser powers from 0 to 500 mW with an increment of 10 mW. The characteristic curve was obtained as shown in Figure 5.7. For the convenience of image processing when converting the Linlog grey levels back into linear grey levels, the laser power of 0 to 500 mW is normalized into the range of 0 to 255. The normalized response curve and the inversed response curve were shown in Figure 5.8. Based on the inversed response curve, a look-up table was generated.

5.1.3 Applicatin of Linlog response in SPI

Figure 5.9 and Figure 5.10 show the composite spatio-temporal phase-stepped speckle interferograms, with each row corresponding to a single frame of 300 x 1 pixels transferred to the PC at 5 kHz, when the object is stationary. The exposure time for the results in Figure 5.9 is 0.09 ms and in Figure 5.10 the exposure time is 0.12 ms. When the exposure time is 0.09 ms, the interferogram under linear response does not suffer from the overexposure problem. Over the whole sequence of 1000 images, the mean phase difference is 0.16° and standard deviation is 6.27°. By comparison, under Linlog response under the same experiment condition, the mean phase difference is 0.12° and standard deviation is 6.18°. When the exposure time became 0.12 ms, it can be seen in Figure 5.9 (b) that many pixels were saturated under linear response. By comparing the

histograms of linear and Linlog response, the brightness of those brighter pixels are shifted towards middle range while the brightness of those darker pixels are not significantly affected, which is expected.

Then the interferograms of a vibrating surface were captured in both linear and non-linear response, as shown in Figure 5.11. The images were captured with inter-frame phase-stepping. Under linear response, as shown in Figure 5.11 (a) & (b), some pixels were saturated. While under Linlog response, as seen in Figure 5.11 (c) & (d), few pixels were saturated and a good output range was maintained. The interferograms were then processed to retrieve the velocity based on Carré's algorithm. It can be seen in Figure 5.12 (a) that a lot of pixels in the middle of the image are marked off due to saturation. The Linlog response did not suffer from the same problem as seen in Figure 5.12 (b).

For the experimental results of inter-frame phase-stepped system discussed in Chapter 3, spatiotemporal velocity maps were processed based on the criteria discussed in section 4.1. The values of those marked pixels are approximated from its neighboring pixels by using a 1×3 filter along the columns. In the spatial phase-stepped system discussed in Chapter 4, because of the additional alignment errors, bigger spatial phase-stepping calibration errors and lower modulation amplitude due to faster surface velocity, results were processed with a 3×3 square filter. No filtering was applied to the measurement data shown in Figure 5.12.

5.2 Application of high-speed SPI to modal analysis

The inter-frame phase-stepped SPI system developed in this thesis has been used by fellow PhD student Steven Earl to measure transient vibration response and evaluate the application of the vibrometer to modal testing in a project collaborated with AWE (Atomic Weapons Establishment). The objective of the project was to investigate the feasibility of acquiring data for model validation for the transient response of a damped structure using the high-speed inter-frame phase-stepped SPI system. The modal assurance criteria (MAC) were obtained from the linear response of the components of a simple test structure in a modal test. Results from the SPI system were compared to those collected at AWE using an accelerometer.

The test object comprised two square plates bolted together along a single edge was held in free-free suspension, by rubber ties from the four outer corners. 21 points were used for the test locations and were marked in Figure 5.13. Six camera ROIs were chosen to capture the response data from those 21 test points. Each test point corresponded to a pixel on the camera, so that the vibration response of these test points can be recorded at these coordinates. The plates were then excited by a modal hammer. The excitation point was kept in a single location as highlighted in Figure 5.13. The force data from the modal hammer were recorded by a digital oscilloscope and the CMOS camera was synchronized with the modal hammer through Labview. Data acquisition was triggered by the impact signal from the modal hammer.

For each ROI, a sequence of up to 5000 interferograms of a horizontal ROI (1x256 pixels) was transferred to the PC as seen in Figure 5.14 (a). Both force data and interferograms were imported to Matlab for signal processing. The Matlab program converted the intensity history of the interferogram sequence into velocity map based on Carré's algorithm using the procedure discussed in Chapter 3. The ring down effect of the impact down the columns can be seen from the velocity map in Figure 5.14 (b). An FFT (Fast Fourier Transform) was then applied to both force and response time signals and the frequency domain data was used to produce FRF (Frequency Response Function) data. Figure 5.15 shows the waterfall FRF of the data from Figure 5.14 (b). It can be seen from that the operational deflection shapes (ODS) can be observed and the resonant frequencies can be identified (in this case 96 Hz, 211Hz, 248Hz, 458Hz, 552 Hz, 724 Hz, 860 Hz and 906 Hz). The FRF data was then used for modal analysis.

This is the first time that a high-speed phase-stepped SPI system is applied into modal analysis. The results were promising especially with the ODS shapes and the resonant frequencies can be easily observed. The results show that the optical system can be used to perform modal testing with the benefits of non-contact multi-point measurement, which include the ability to measure non-repeatable transient events and the reduction in time required for data acquisition.

5.3 Discussion

Due to spatial variations in speckle intensity, some low-modulating and saturated pixels could not be analysed. It is showed that these lost data points could be saved by using the Linlog response of the CMOS camera. The valid measurement area on the object surface is increased compared to a linear detector. The errors of Linlog approach and linear approach are still in a similar range. The mean phase difference is 0.12° and standard deviation is 6.18° for linear approach. The mean phase difference is 0.16° and standard deviation is 6.27° for Linlog approach. The vibration measurement result showed that a significantly number of data points could be saved without increased noise levels.

It was also noted that the dynamic range of the inter-frame phase-stepped SPI system for surface velocity measurement is a main limit for its applications in industry. The raw velocity data was investigated that a single test pixel was measured by both the inter-frame phase-stepped system and a single-point vibrometer from Polytec with similar force level input. Both measurements showed ring-down effects after impact as expected, but the single-point vibrometer showed a maximum velocity of 3 mm/s, well in excess of the 1.4 mm/s velocity limit of the SPI system. The velocity limit was set by the Nyquist limit for sampling the interference signal as discussed in equation (5-1) in Chapter3, which depends on the wavelength of the laser, frame rate and the interferometer sensitivity factor (equals to 2 in this SPI system). The effect of exceeding the maximum velocity limit can be seen in Figure 5.14 (b) as discontinuities in the data, that introduced errors into the recovered vibration amplitude. However, it is expected that the new sub-Nyquist spatial phase-stepped SPI system will significantly increase the measurement ability by at least an order of magnitude and should be able to tackle the problem in future.

Another limit of the current system is that the system has a relatively small data acquisition buffer length (a current hardware limit) which restricts the number of the samples in one recording up to 5000, equivalent to a sampling window of ~0.7 seconds in this experiment. The short sampling window resulted that only 8 natural frequencies were obtained compared to 12+ from the accelerometer. However, this is a technical restriction that can be improved by introducing new hardware with larger buffer capacity.

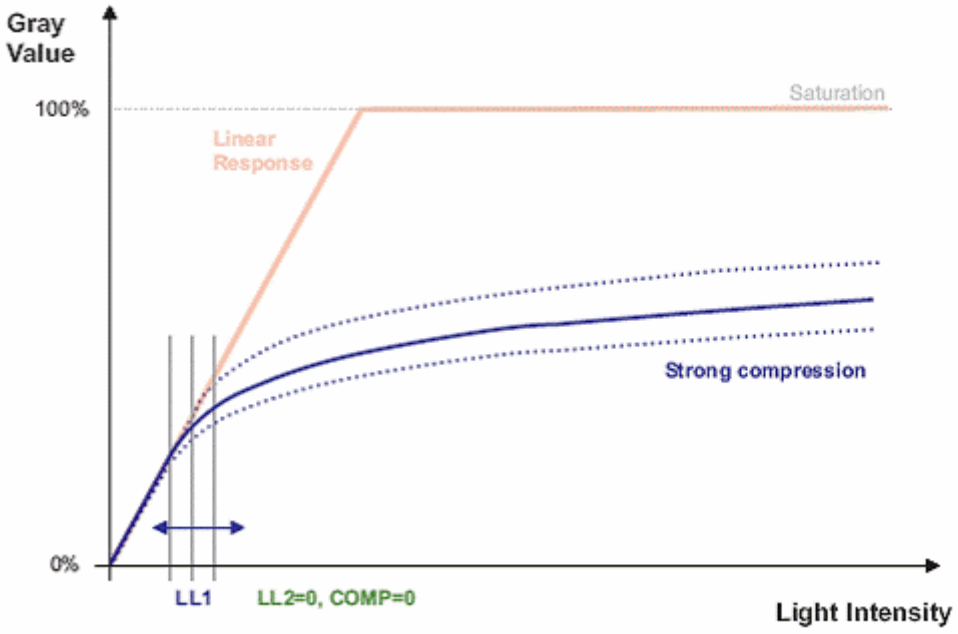

Figure 5.1 Simplest Linlog setup: LL2=0, COMP=0.(www.photonfocus.com)

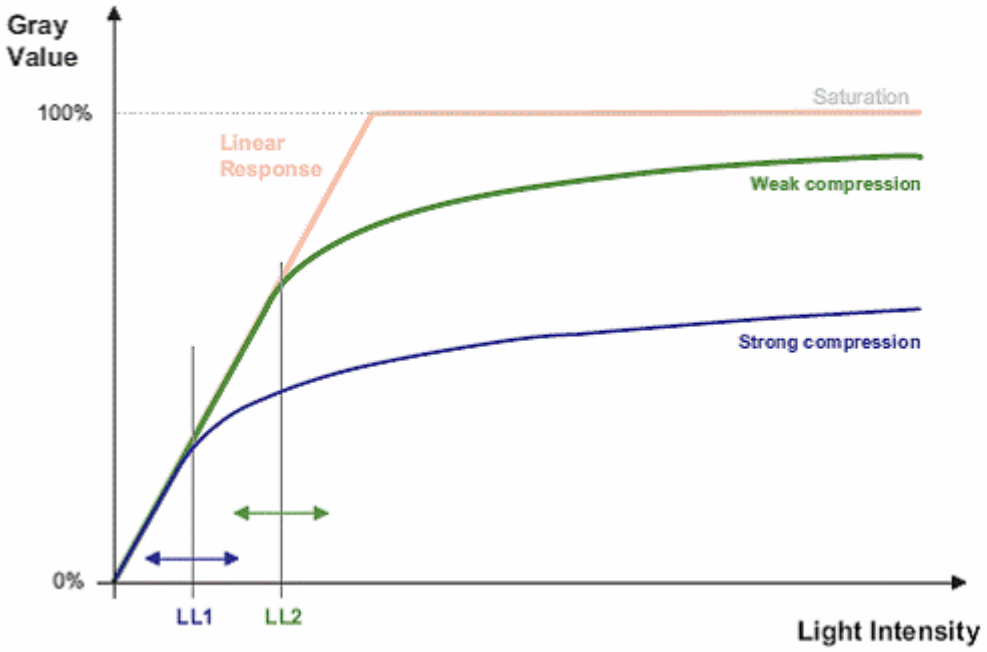

Figure 5.2 Strong and week compression. (www.photonfocus.com)

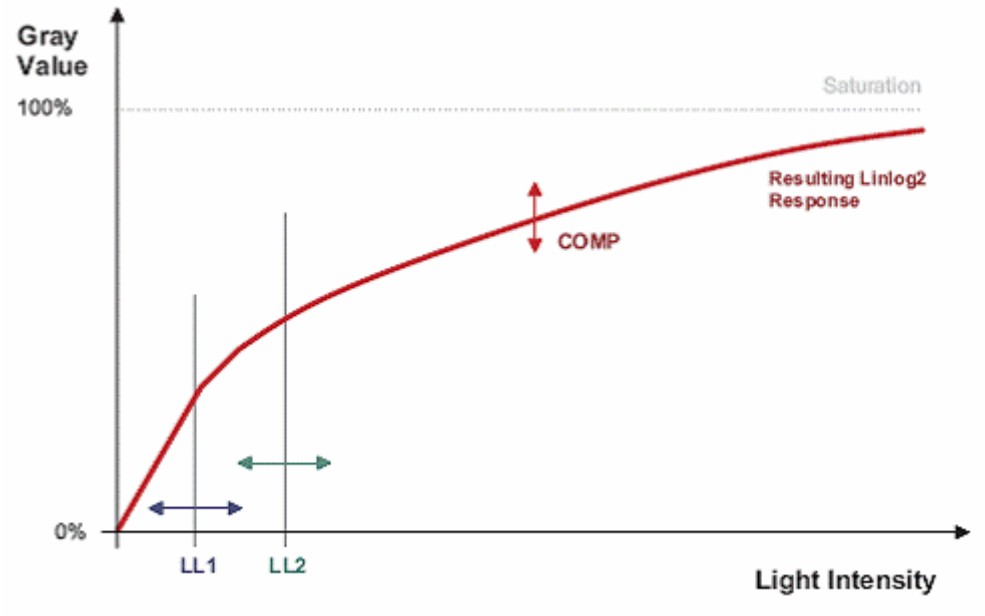

Figure 5.3 Linlog2.(www.photonfocus.com)

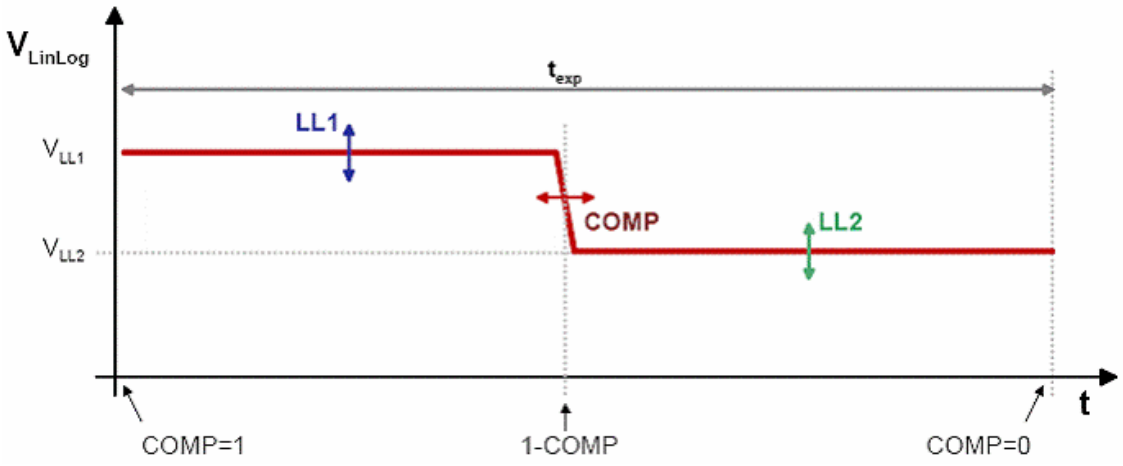

Figure 5.4 Explanation of LL1, LL2 and COMP. (www.photonfocus.com)

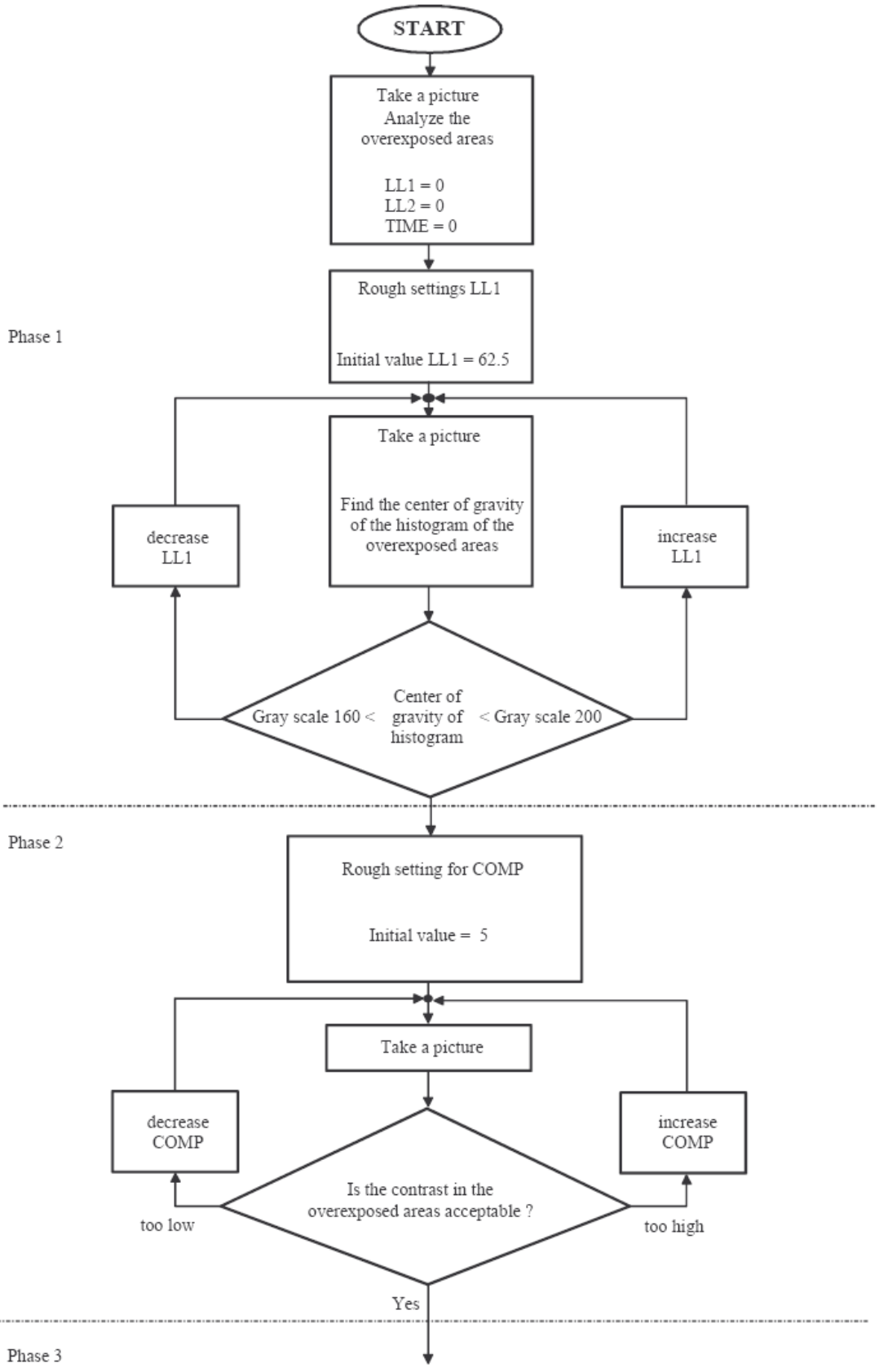
START
Take a picture
Analyze the overexposed areas
LL1 = 0
LL2 = 0
TIME = 0
Rough settings LL1
Initial value LL1 = 62.5
Phase 1
Take a picture
Find the center of gravity of the histogram of the overexposed areas
decrease LL1
increase LL1
Gray scale 160 <
Center of gravity of histogram
< Gray scale 200
Phase 2
Rough setting for COMP
Initial value = 5
Take a picture
decrease COMP
increase COMP
Is the contrast in the overexposed areas acceptable ?
too low
too high
Yes
Phase 3

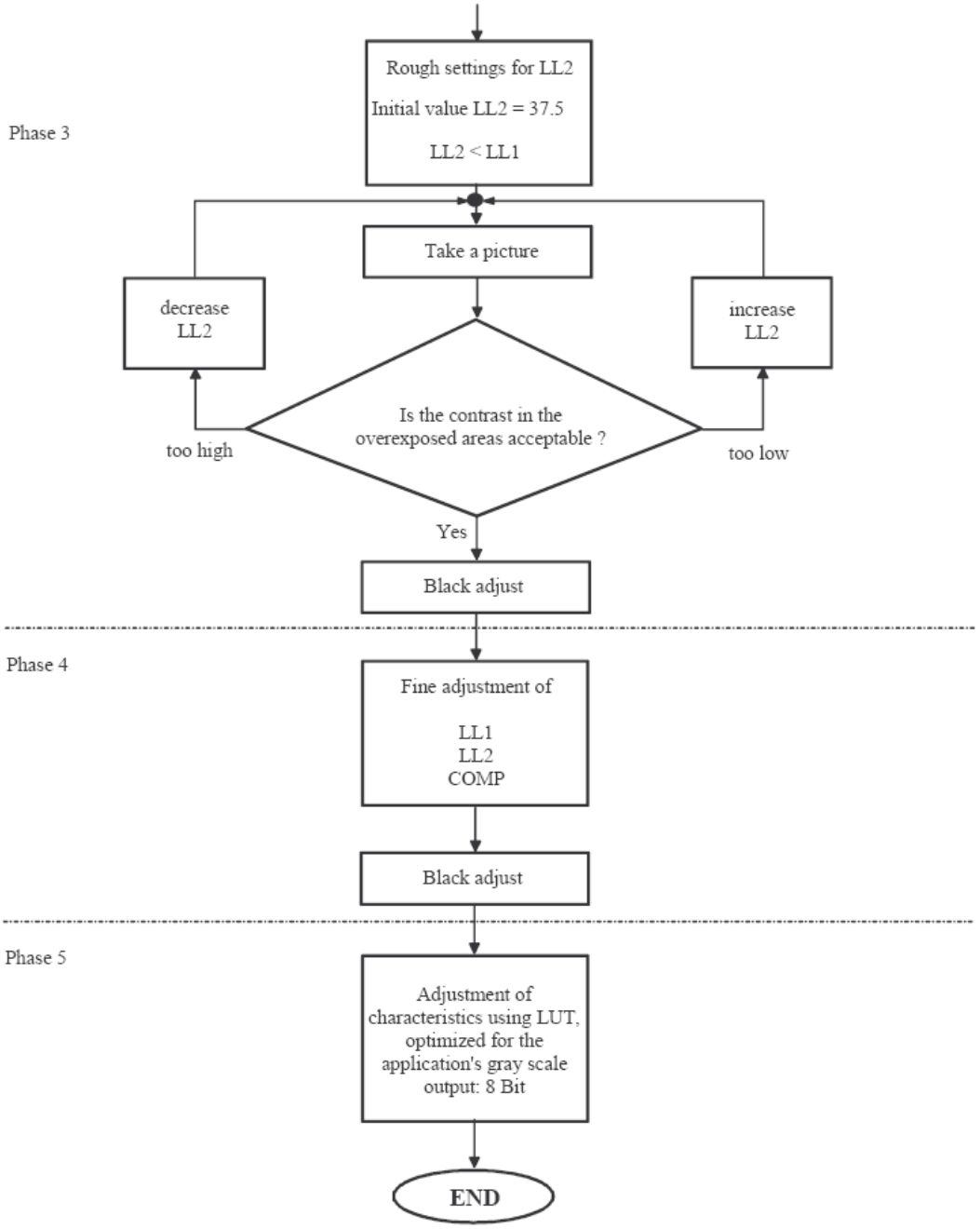

Figure 5.5: Flow chart for optimizing Linlog parameters. (www.photonfocus.com)

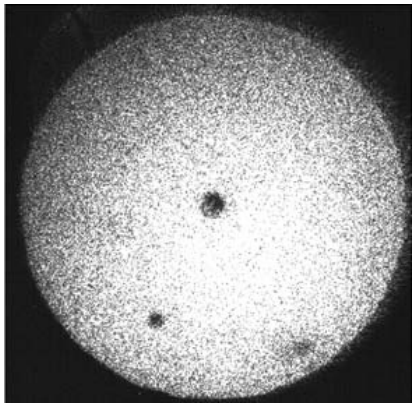

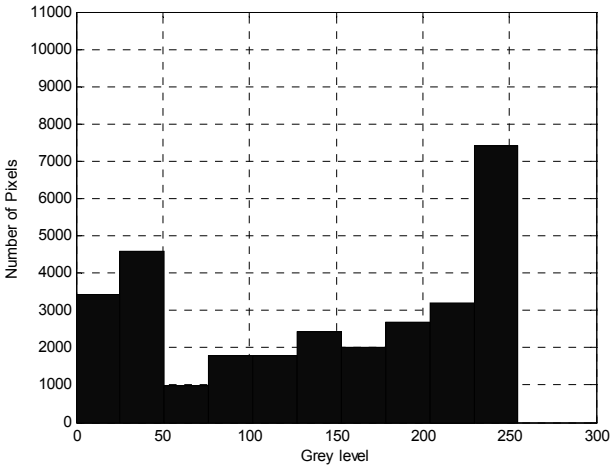
Number of Pixels
Grey level
0
1000
2000
3000
4000
5000
6000
7000
8000
9000
10000
11000
0
50
100
150
200
250
300

(a)

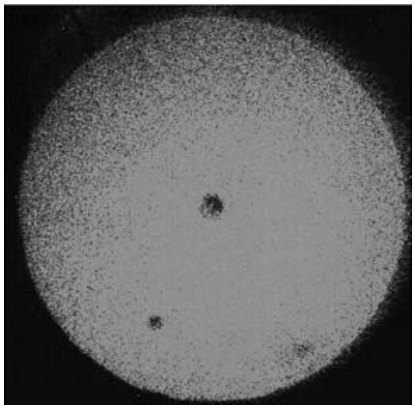

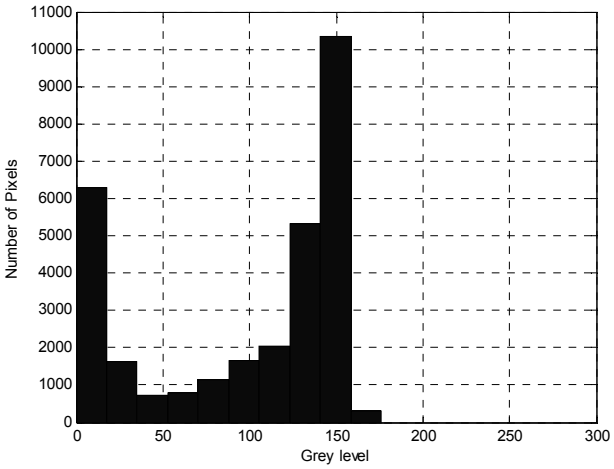
Number of Pixels
Grey level
0
1000
2000
3000
4000
5000
6000
7000
8000
9000
10000
11000
0
50
100
150
200
250
300

(b)

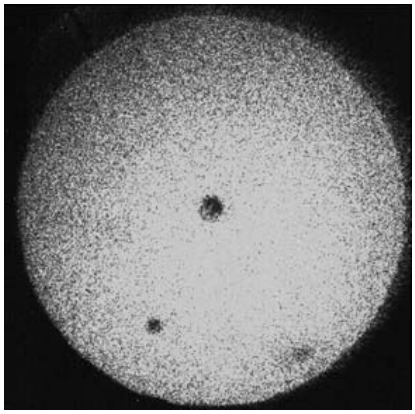

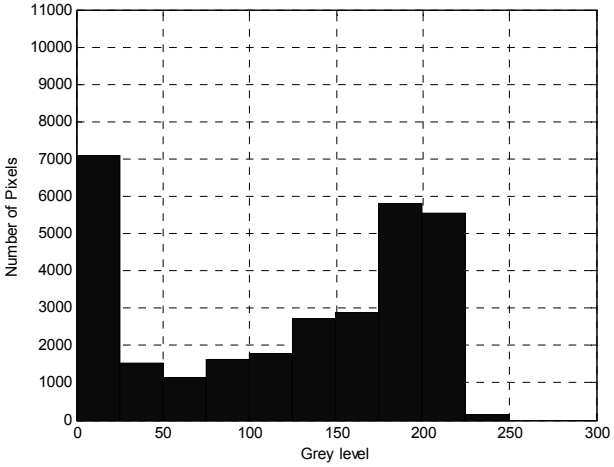
Number of Pixels
Grey level
0
1000
2000
3000
4000
5000
6000
7000
8000
9000
10000
11000
0
50
100
150
200
250
300

(c)

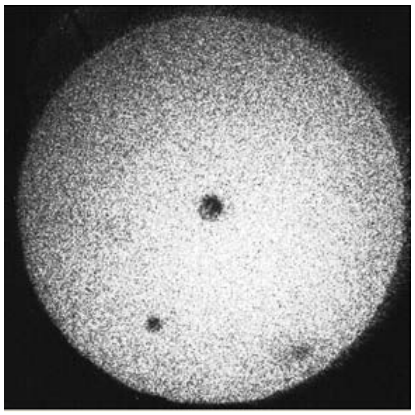

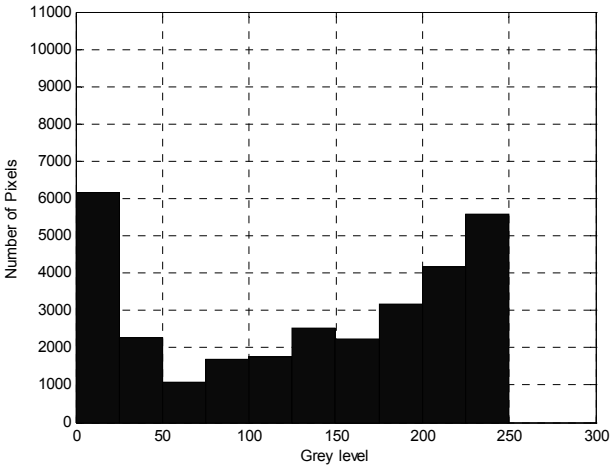

(d)

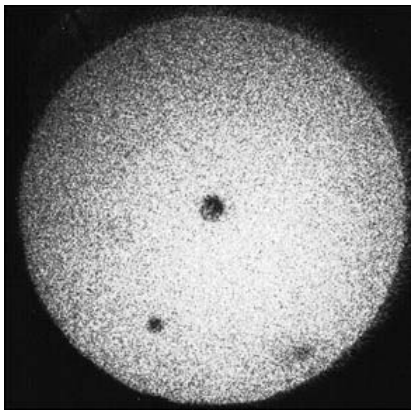

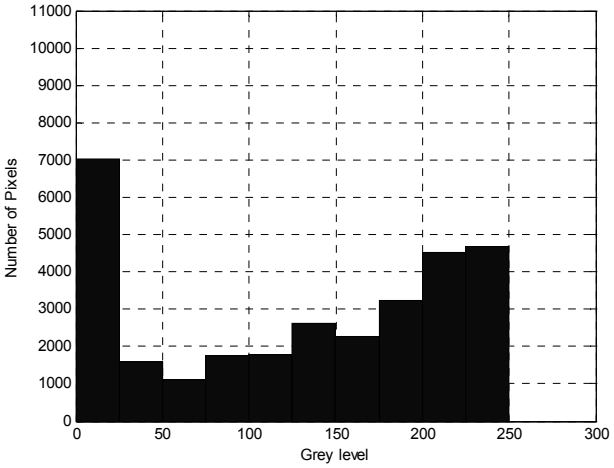

(e)

Figure 5.6 Interferograms recorded under linear and Linlog response and their histograms. (a) linear response, (b) Linlog response LL1=100, LL2=0, COMP=0, (c) Linlog response LL1=80, LL2=0, COMP=0, (d) Linlog response LL1=80, LL2=0, COMP=10, (e) Linlog response LL1=80, LL2=55, COMP=10.

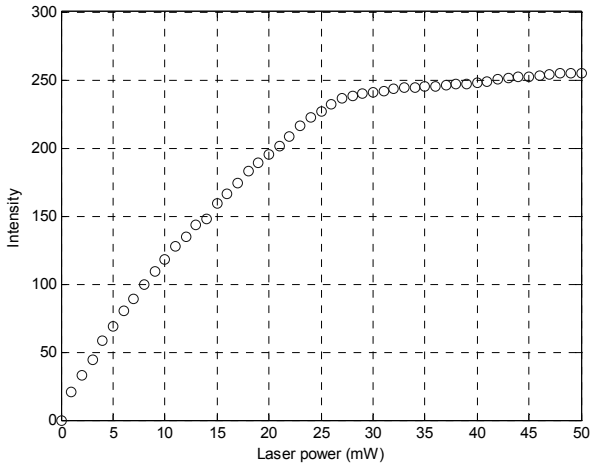

Figure 5.7 Characteristic response obtained for Linlog response by different laser power.

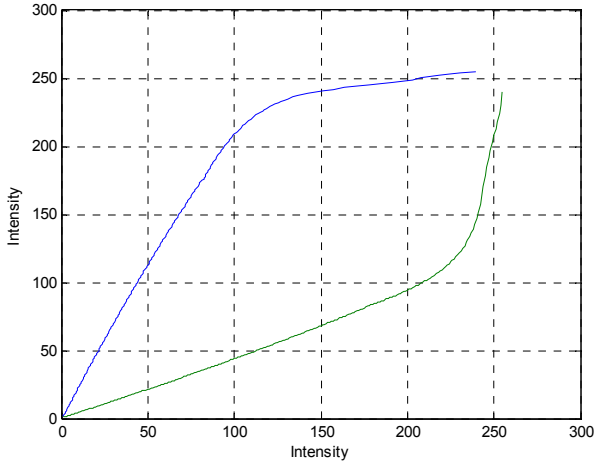

Figure 5.8: Fitted characteristic response curve for Linlog response and inversed response curve.

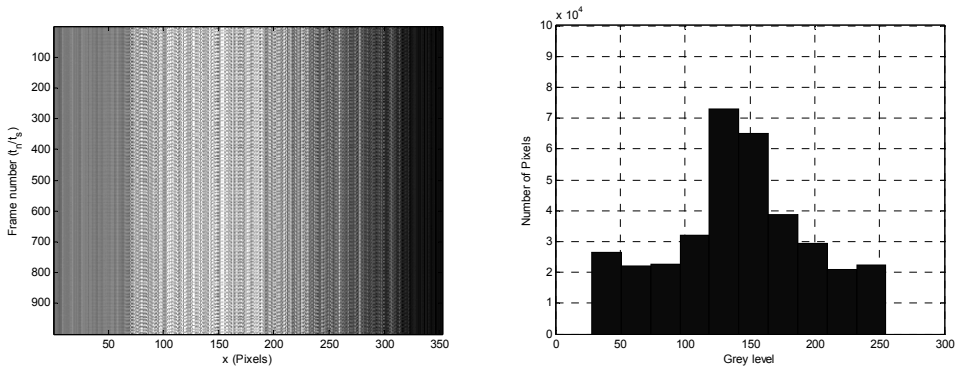

(a) (b)

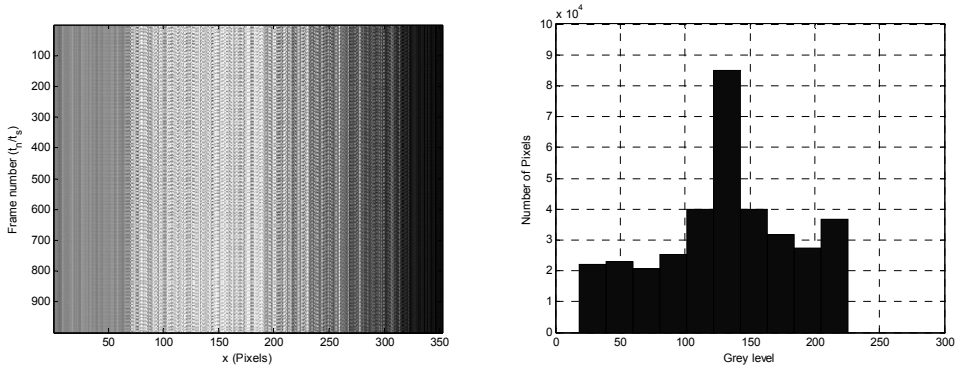

(c) (d)

Figure 5.9 Spatial-temporal speckle pattern showing intensity variation for the horizon ROI (300 x 1 pixels) recorded at 5 kHz for stationary object. Exposure time = 0.09 ms. (a) linear response and (b) histogram. (c) Linlog response and (d) histogram.

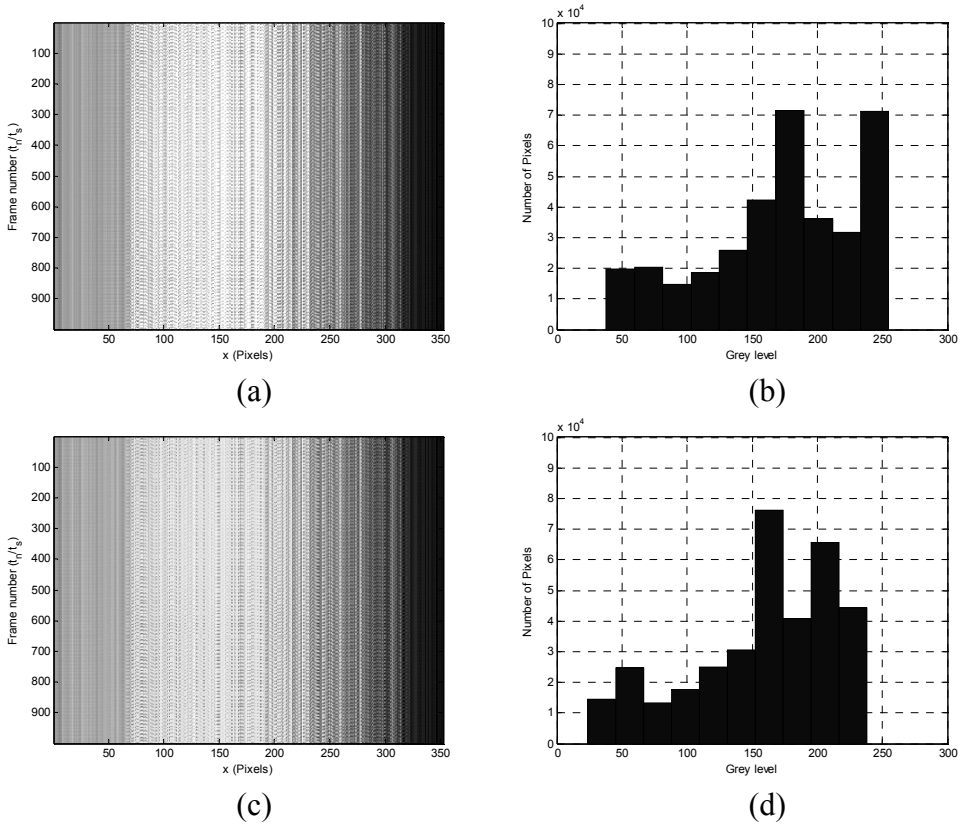

Figure 5.10 Spatial-temporal speckle pattern showing intensity variation for the horizon ROI (300 x 1 pixels) recorded at 5 kHz for stationary object. Exposure time = 0.12 ms. (a) linear response and (b) histogram. (c) Linlog response and (d) histogram.

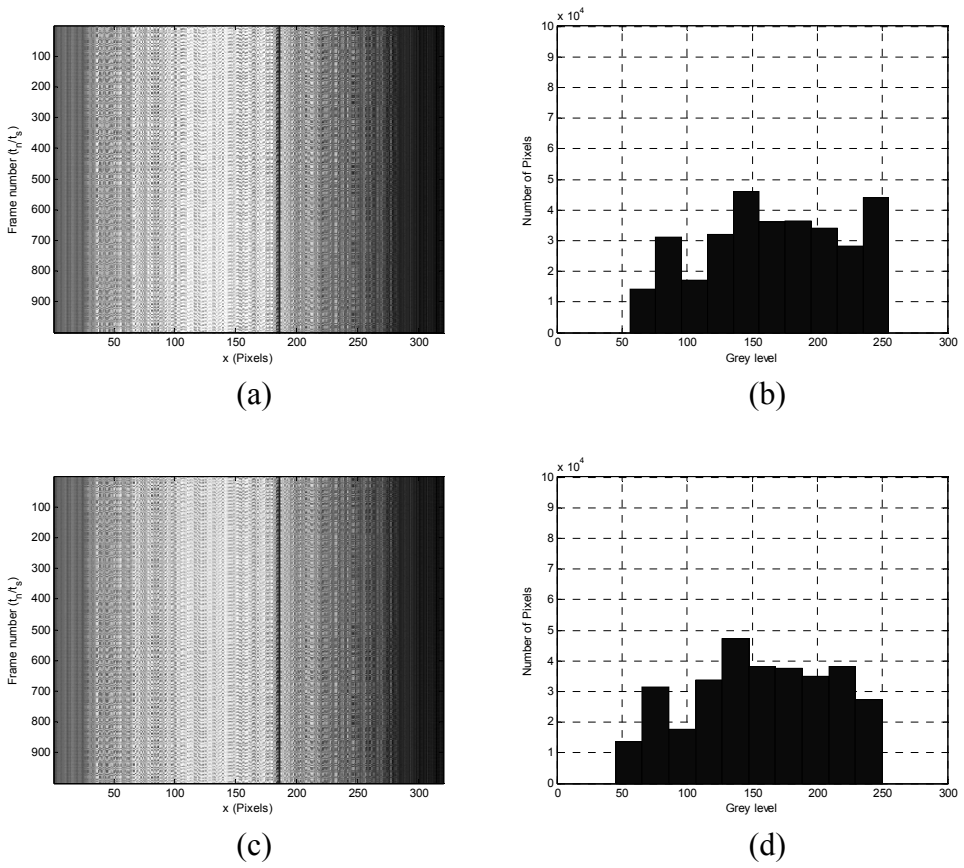

Figure 5.11 Spatial-temporal speckle pattern showing intensity variation for the horizon ROI (300 x 1 pixels) recorded at 5 kHz for a vibrating object. Exposure time = 0.12 ms. (a) linear response and (b) histogram. (c) Linlog response and (d) histogram.

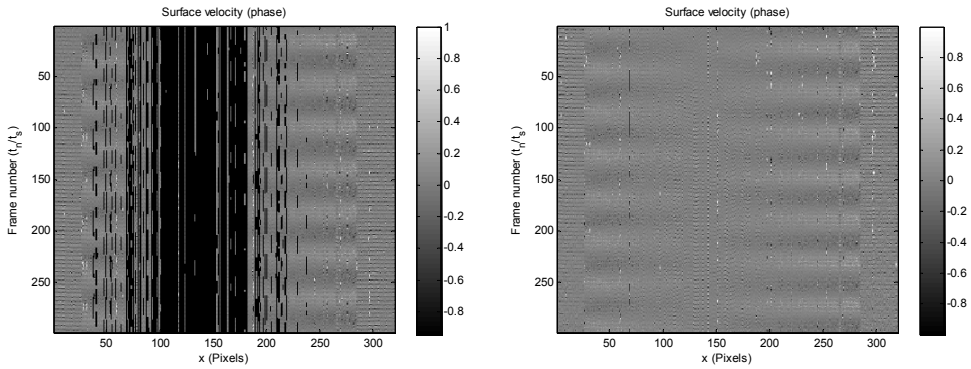

Figure 5.12: 2-D spatio-temporal result for the horizon ROI (300 x 1 pixels) recorded at 5 kHz for a vibrating object. Exposure time = 0.12 ms. (a) linear reponse (b) Linlog response

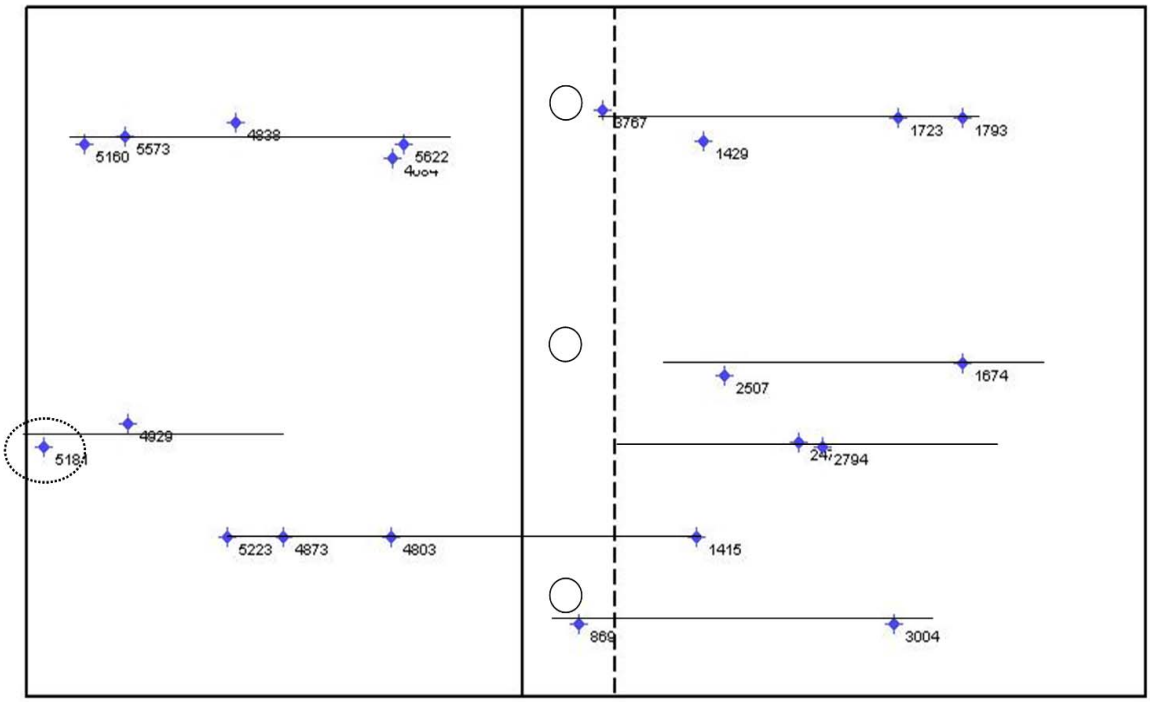

Figure 5.13: Test object with 7 ROI and the excitation point marked

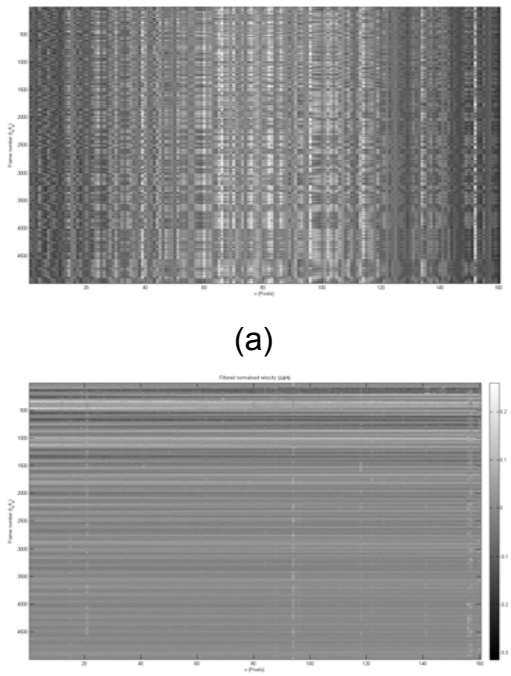

(a)

(b)

Figure 5.14 (a) Composite spatio-temporal interferogram of the vibrating object. (b) Filtered velocity against frame number

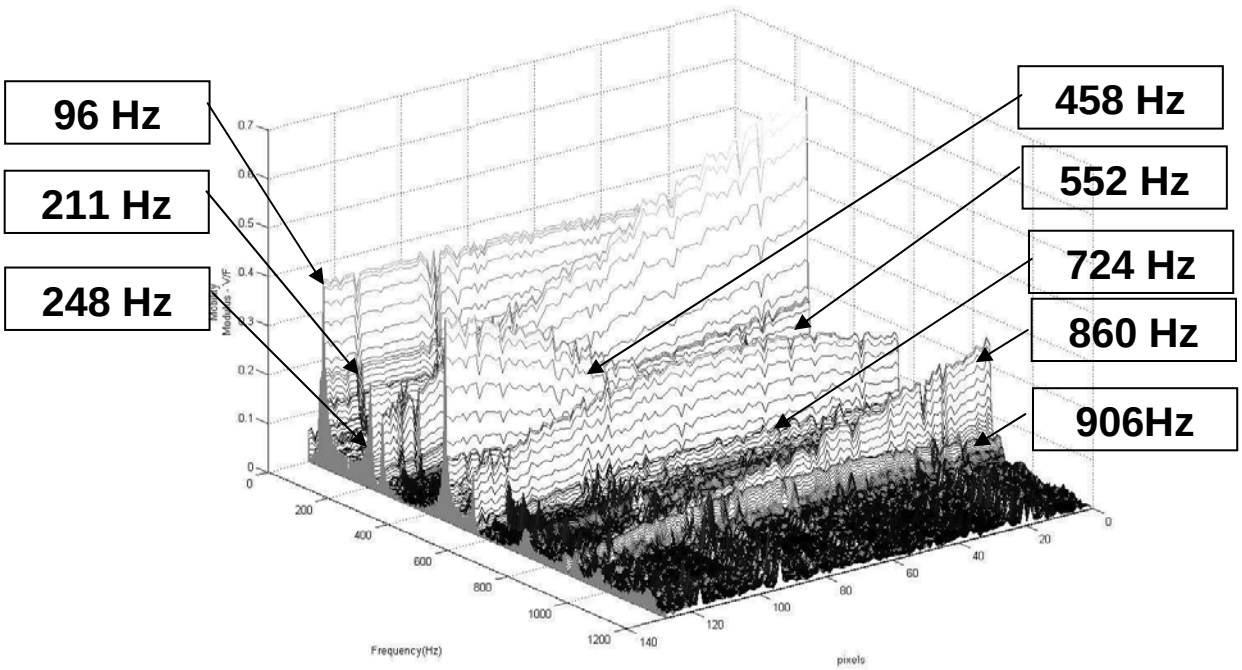

Figure 5.15 Results from a ROI with resonances shown

6

Conclusions and Future Work

In this chapter the work presented in this thesis will be briefly summarized. Following an assessment and an analysis, the final conclusions will be presented. Finally various suggestions for direction of further work are noted.

6.1 Conclusion

We have demonstrated a multi-point vibrometer based on a CMOS camera and inter-frame phase-stepping. The temporal evolution of dynamic deformation was measured using the system. An advantage that CMOS sensors have over CCDs is that each photo-site in a CMOS sensor can be read out independently. This flexibility enables ROIs to be identified with full-field time-averaged measurements and then to interrogate those regions with time-resolved measurements sampled at 70 kHz. Surface velocity and acceleration plots were presented for a vibrating test target.

A numerical and analytical investigation determined the velocity limit of the system for the first time based on the effect of surface velocity, surface acceleration, and camera frame rate for the first time for inter-frame SPI. The surface velocity has been

expressed in normalized velocity based on the Nyquist limit. We conclude that the maximum surface velocity that can be reliably measured with inter-frame phase-stepping corresponds to 0.3 Nyquist limit.

With the aim to increase the velocity limit, we then developed a high-speed spatial phase-stepped SPI system. Binary gratings were used in SPI for the first time to split the images, introduce phase step and meanwhile to suppress the even-order quadrants. The system was aligned precisely with the aid of digital image correlation and the spatial phase step size was calibrated by using inter-frame phase-stepped PSI. A 2-image algorithm which calculates the phase change directly is used to recover the surface velocity. A compensating algorithm based on the actual phase step size was used to reduce phase step errors.

The spatial phase-stepped SPI system was then combined with sub-Nyquist theory. Numerical and analytical investigation showed that the basic assumption that the interference fringes must be sampled at least twice per fringe could be overcome. The effect of surface velocity, surface acceleration, camera frame rate, exposure time, intensity noise and miscalibration of spatial phase step were quantified. A successful measurement of velocity of $15.9v_{Nyq}$ was verified in the simulation by assuming the surface velocity is continuous. By assuming the surface acceleration is continuous, the measurement range of acceleration could be further extended to $253.3v_{Nyq}$. The experimental results of the sub-Nyquist spatial SPI system confirmed that the current measurement limit of the system had been increased by an order of magnitude compared to that of the inter-frame phase-stepped SPI system. However, to fully realize the potential of sub-Nyquist SPI, the accuracy of the SPI system need be further increased and thus the current hardware setup also need be improved, for example a shorter exposure time.

Compared to commercially available LDVs, high-speed SPI has long been suffering from its relatively low inter-frame resolution (up to 20 mm/s at a recording speed of 1 MHz with 532 nm laser) compared to ~1 m/s of LDVs, although the high-speed SPI technique enjoys the advantage of high spatial resolution. This project showed that the Nyquist limit could be exceeded. By upgrading only to a commercially available 1 MHz high-speed camera, measurement ability of 0.2 m/s can be realized. By further

reducing the exposure time, the measurement ability could potentially be increased to the order of metres per second.

6.2 Future work

To achieve the full potential of the sub-Nyquist SPI in the experiment, there are a few aspects that could be improved as discussed in Chapter 4: 1) phase-stepping errors, 2) exposure time, and 3) noise level.

1. It is showed in Figure 4.14 that the phase-stepping errors are very sensitive to the relative rotation between the gratings. A rotation controller with fine adjustment for both gratings could be implemented to achieve a more accurate spatial phase step.

2. Alternative approaches could also be used to improve the accuracy of spatial phase step.

   Professor Andrew Moore at Heriot-Watt University proposed that a polarization-selective DOE could eliminate tilt-dependent phase-step errors. The polarisation-selective DOEs comprise two anisotropic substrates joined together with an isotropic material at their etched surfaces. The two birefringent substrates are arranged with their optical axes mutually orthogonal and normal to the incident beam, and introduce independent impulse responses for two orthogonal linear states of polarisation[88]. The orthogonally polarized beams follow a common path through the DOE, but are treated independently to introduce the required relative phase steps between the diffracted orders.

   A pixelated phase mask could also be used to introduce spatial phase stepping. The phase mask consists of a micropolarizer array which is divided into unit cells. Each unit cell consists of four pixels, each containing a wire grid polarizer orientated such that a relative phase step of $\pi/2$ is induced between each pixel.

3. The exposure time is crucial for the accuracy of the spatial phase-stepping method, as discussed in Chapter 4. At higher velocities, the exposure time became the dominant factor restricting the accuracy of the measured phase and

the highest surface velocity that could be achieved. The simulation in Chapter 4 showed that by shortening the exposure time with a high-power pulse laser which is synchronized to the high-speed camera, the measurement range of the system could be significantly increased.

4. For high-speed imaging, it is desirable to preserve high signal-to-noise ratio under low light conditions, which mainly depends on the ability of the camera. The noise level could be decreased with a camera which has a higher signal-to-noise ratio.

5. A beam shaper could be included into the system to help achieve more uniform illuminations for both reference and object beams. This will greatly increase the number of the available measurement points.

References:

1 L.Scalise and N.Paone. Laser Doppler vibrometry based on self-mixing effect, Opt. Laser Eng, 38,173 (2002)

2 L.Scalise, G.Stavrakakis. A.Pouliezos.Fault detection for quality control of household appliances by non-invasive laser Doppler technique and likelihood classifier.Measurement, 25, 237 (2000)

3 Q.V.Davis, W.K.Kulczyk. Vibrations of turbine blades by means of a laser. Nature, 222, 475 (1969)

4 C.J.D.Pickering, N.A.Halliwell. The laser vibrometer: a portable instrument. J. Sound and Vibration 107, 471 (1986)

5 A.B.Stanbridge, D.J.Ewins. Modal testing using a scanning laser Doppler vibrometer. Mechanical Systems and Signal Processing. 13(2), 255 (1999)

6 A.B.Stanbridge, A.Z.Khan, D.J.Ewins. Modal testing using impact excitation and a scanning ldv, Shock and Vibration 7(2). 91 (2000)

7 A.B.Stanbridge, M.Martarelli, D.J.Ewins. Scanning laser doppler vibrometer applied to impact modal testing, Shock and Vibration Digest 32 (1). 35 (2000)

8 A.B.Stanbridge, M.Martarelli, D.J.Ewins. Measuring area vibration mode shapes with a continuous-scan LDV. Measurement, 35, 181 (2004)

9 M.Martarelli, D.J.Ewins. Continuous scanning laser doppler vibrometry and speckle noise occurrence, Mechanical Systems and Signal Processing. 20(8). 2277 (2006)

10 http://www. metrolaserinc. com/vibromet_multibeam.htm

11 http://ipp. gsfc. nasa. gov/downloads/HHT_expo_fleming.pdf

12 D.Gabor. A new microscopic principle, Nature, 161, 777 (1948)

13 K.A.Stetson and R.L.Powell. Interferometric hologram evaluation and real-time vibration analysis of diffuse objects, J. Opt. Soc. Am. 55 1694 (1965)

14 C.M.Vest. Holographic interferometry, Wiley (1979)

15 T.Kreis. Holographic Interferometry (Berlin: Akademie) (1996)

16 R.L.Powell, K.A.Stetson. Interferometric vibration analysis by wavefront reconstruction, J. Opt Soc. America, 55(12), 1593 (1965)

17 U.Schnars and W.Juptner. Direct recording of holograms by a CCD-target and numerical reconstruction. appl. Opt. 33. 179 (1994)

18 F.Zhang, J.D.R.Valera, I.Yamaguchi, M.Yokota, and G.Mills. Vibration Analysis by Phase Shifting Digital Holography. Opt. Rev. 11(5), 297 (2004)

19 Y.Fu, G.Pedrini, W.Osten. Vibration measurement by temporal Fourier analyses of a digital hologram sequence. Appl. Opt. 46(23), 5719 (2007)

20 L.Yang, A.Ettemeyer. Strain measurement by three-dimensional electronic speckle pattern interferometry: potential, limitations and applications. Opt. Eng. 42(5), 1257 (2003)

21 J.A.Leendertz, J.N.Butters. Speckle pattern and holographic techniques in engineering metrology. Opt. Laser Technol. 3, 26 (1971)

22 H.Atcha, R.P.Tatam, Heterodyning of fibre optic electronic speckle pattern interferometers using laser diode wavelength modulation, Meas. Sci. Technol. 5, 704 (1994)

23 H.D.Ford, H.Atcha, R.P.Tatam. Optical fibre technique for the measurement of small frequency separations: application to surface profile measurements using electronic speckle pattern interferometry, Meas. Sci. Technol. 4, 601 (1993)

24 K.J.Gasvik. Optical Metrology, Wiley (1995)

25 J.N.Butters, J.A.Leendertz. Holographic and video techniques applied to engineering measurement. J. Meas. Contro l4, 349 (1971)

26 A.J.Moore, J.D.C.Jones, J.D.R.Valera. 'Dynamic measurements' in Digital speckle interferometry and relatedtechniques, ed. Rastogi P. K, Wiley (2001)

27 K.Creath. Phase-shifting speckle interferometry. Appl. Opt. 24, 3053 (1985)

28 D.W.Robinson and D.C.Williams. Digital phase stepping speckle interferometry. Opt. Comm. 57, 26 (1986)

29 K.Hoegmoen, O.J.Lokberg. Detection and measurement of small vibrations using electronic speckle pattern interferometry. Appl. Opt. 16, 1869 (1977)

30 O.J.Lokberg, K.Hogmoen. Vibration phase mapping using electronic speckle pattern interferometry. Appl. Opt., 15(11), 2701 (1976)

31 S.Nakadate, T.Yatagai, H.Saito. Electronic speckle pattern interferometry using digital image processing techniques. Appl. Opt. 19, 1879 (1980)

32 C.Joenathan. Vibration fringes by phase stepping on an electronic speckle pattern interferometer: an analysis. Appl. Opt. 30, 4658 (1991)

33 T.J.Cookson, J.N.Butters, H.C.Pollard. Pulsed lasers in electronic speckle pattern interferometry. Opt laser Technol. 10, 119 (1978)

34 A.J.Moore, C.Pérez-López. Low-frequency harmonic vibration analysis with double-pulsed addition electronic speckle pattern interferometry, Opt. Eng. 35(9), 2641 (1996)

35 F.M.Santoyo, A.J.Moore, J.R.Tyrer, N.A.Ochoa. Noise reduction in twin-pulsed addition electronic speckle pattern interferometry fringe patterns. Opt Eng, 33(5), 1712 (1994)

36 A.Davila, D.Kerr, G.H.Kaufmann. Digital processing of electronic speckle pattern interferometry addition fringes. Appl Opt, 33(25), 5964 (1994)

37 D.I.Farrant, G.H.Kaufmann, J.N.Petzing, J.R.Tyrer, B.F.Oreb, D.Kerr. Measurement of transient deformations with dual-pulse addition electronic speckle-pattern interferometry. Appl Opt, 37(31), 7259 (1998)

38 N.Alcala-Ochoa, F.M.Santoyo, A.J.Moore, C.Perez-Lopez. Contrast enhancement of electronic speckle pattern interferometry addition fringes. Appl Opt, 36(13), 2783 (1997)

39 R.Spooren. Double pulsed subtraction TV holography. Opt Eng, 31, 1000 (1992)

40 G.Pedrini, Y.L.Zou, H.J.Tiziani. Digital double-pulse holographic interferometry for vibration analysis. J Mod Opt, 42, 367 (1995)

41 A.Fernandez, A.J.Moore, C.Perez-Lopez, A.F.Doval, J.Blanco-Garcia. Study of transient deformations with pulsed TV holography: application to crack detection. Appl Opt, 36(10), 2058 (1997)

42 M.C.Shellabear, J.R.Tyrer. Application of ESPI to three dimensional vibration measurement. Opt Laser Eng, 15, 43 (1991)

43 J.D.R. Valera, A.F. Doval and J.D.C. Jones, “Determination of vibration phase with electronic speckle pattern interferometry”, Electron. Lett 28 2292-2294 (1992)

44 A.J.Moore, D.P.Hand, J.S.Barton, J.D.C.Jones. Transient deformation measurement with electronic speckle pattern interferometry and a high-speed camera. Appl Opt 38(7), 1159 (1999)

45 M.Reeves, N.Taylor, C.Edwards, D.Williams, C.H.Buckberry. A study of brake disc modal behavior during squeal generation using high-speed electronic speckle pattern interferometry and near-field sound pressure measurements. Proc Instn Mech Engrs;214(Part D) 285 (2000)

46 C.Buckberry, M.Reeves, A.J.Moore, D.P.Hand, J.S.Barton, J.D.C.Jones. The application of high-speed TV-holography to time-resolved vibration measurements. Opt. Las. Eng. 32, 387 (2000)

47 J.M.Kilpatrick, A.J.Moore, J.S.Barton, J.D.C.Jones, M.Reeves, C.Buckberry. Measurement of complex surface deformation by high-speed dynamic phase-stepped digital speckle pattern interferometry. Opt. Letts. 25(15), 1068 (2000)

48 P.Carré. Installation et utilisation du comparateur photoélectrique et interférential du Bureau International des Poids et Mesures. Metrologia. 2, 13 (1966**)**

49 C.Joenathan, B.Franze, P.Haible, H.J.Tiziani. "Speckle interferometry with temporal phase evaluation for measuring large-object deformation. Appl. Opt. 37, 2608 (1998)

50 M.Takeda, I.Hideki and S.Kobayashi. Fourier-transform method of fringe pattern analysis for computer based topography and interferometry. J Opt Soc Am 2, 156 (1983)

51 A.Fernandez, G.H.Kaufmann, A.F.Doval, J.Blanco-Garcia and J.L.Fernandez. Comparison of carrier removal methods in the analysis of television holography fringes by the Fourier transform method. Opt Eng 37(11), 2899 (1998)

52 G.H.Kaufmann and G.E.Galizzi. Phase measurement in temporal speckle pattern interferometry: Comparison between the phase-shifting and the Fourier transform methods, Appl. Opt. 41, 7254 (2002)

53 J.M.Huntley, G.H.Kaufmann, D.Kerr. Phase shifted dynamic speckle pattern interferometry at 1 kHz. Appl. Opt. 38(31), 6556 (1999)

54 J.M.Huntley, H.Saldner. Temporal phase-unwrapping algorithm for automated interferogram analysis. Appl. Opt, 32, 3047 (1993.

55 J.M.Huntley. Phase errors in low-frequency vibration measurement with high-speed phase-shifting speckle pattern interferometry. Opt Eng (2001);40(9):1984–92.

56 A.Davila, J.M.Huntley, G.H.Kaufmann and D.Kerr. High-speed dynamic speckle interferometry: phase errors due to intensity, velocity and speckle decorrelation,. Appl. Opt. 44(19) 3954-3962 (2005)

57 P.D.Ruiz, J.M.Huntley, Y.Shen, C.R.Coggrave, and G.H.Kaufmann. Effects of random vibration in high-speed phase-shifting speckle pattern interferometry. Appl. Opt. 41, 3941 (2002)

58 J.Kauffmann and H.J.Tiziani, Time-resolved vibration measurement with temporal speckle pattern interferometry, Appl. Opt. 45, 6682 (2006)

59 G.Pedrini, W.Osten and M.E.Gusev. High-speed digital holographic interferometry for vibration measurement. Appl. Opt. 45, 3456 (2006)

60 R.Smythe, R.Moore. Instantaneous Phase Measuring Interferometry. Opt. Eng. 23(4) 361 (1984)

61 M.Kujawinska and D.W.Robinson. Multichannel phase-stepped holographic interferometry. Appl. Opt. 27(2), 312 (1988)

62 L.Salbut, K.Patorski and M.Kujawinska, Polarization approach to high-sensitivity moiré interferometry. Opt. Eng. 31(3), 434 (1992)

63 Q.Kemao, W.Xiaoping, and A.Asundi. Grating-based real-time polarization phase-shifting interferometry: error analysis. Appl. Opt. 41, 2448 (2002)

64 M.Kujawinska and D.W.Robinson. Multichannel phase-stepped holographic interferometryAppl. Opt. 27(2), 312 (1988)

65 O.Kwon. Multichannel phase-shifted interferometer. Opt. Lett. 9(2), 59 (1984)

66 O.Y.Kwon, D.M.Shough and R.A.Williams. Stroboscopic phase-shifting interferometry. Opt. Lett. 12(11), 855 (1987)

67 A.J.P.Haasteren and H.J.Frankena. Real-time displacement measurement using a multicamera phase-stepping speckle interferometer. Appl. Opt. 33(19), 4137 (1994)

68 A.L.Weijers, H.van Brug, and H.J.Frankena. Polarization phase stepping with a savart element. Appl. Opt. 37, 5150 (1998)

69 T.D.Upton and D.W.Watt. Optical and electronic design of a calibrated multichannel electronic interferometer for quantitative flow visualization. Appl. Opt. 34(25), 5602 (1995)

70 A.Hettwer, J.Kranz, J.Schwider. Three channel phase-shifting interferometer using polarization-optics and a diffraction grating. Opt. Eng. 39(4), 960 (2000)

71 B.Barrientos Garcia, A.J.Moore, C.Perez-Lopez, L.Wang, T.Tschudi, Transient deformation measurement with electronic speckle pattern interferometry by use of a holographic optical element for spatial phase stepping. Appl Opt (1999);38(28):5944–7.

72 B.Barrientos Garcia, A.J.Moore, C.Perez-Lopez, L.Wang, T.Tschudi, Spatial phase-stepped interferometry using a holographic optical element. Opt. Eng. 38(2), 2069. 1999

73 J.Millerd, N.Brock, J Hayes, M.North-Morris, M.Novak and J.Wyant. Pixelated phase-mask dynamic interferometer. Proc. SPIE. 5531, 304 (2004)

74 J.Wyant. Going through a phase- dynamic phase-shifting interferometry beats vibration. OEmagazine. August. (2005):
http://spie.org/x15791.xml?highlight=x2404&ArticleID=x15791

75 J.Grievenkamp. Sub-Nyquist interferometry. Appl. Opt. 26(24), 5245. (1987)

76 J.E.Greivenkamp, A.E.Lowman and R.J.Palum. Sub-Nyquist interferometry: implementation and measurement capability. Opt. Eng. 35(10), 2962 (1996)

77 M.Servin, A.Davila and J.A.Quiroga. Extended-range temporal electronic speckle pattern interferometry. Appl. Opt. 41, 46 (2002)

78 J.Munoz, M.Strojnik and G.Paez. Detection and interpretation of high-frequency spatial interferograms. Appl Opt, 42(34), 6846 (2003)

79 P.Ferraro, C.Del Core, L.Miccio, S.Grilli, S.De Nicola, A.Finizio and G.Coppola. Phase map retrieval in digital holography: avoiding the undersampling effect by a lateral shear approach. Opt. Letters. 32(15), 2233 (2007)

80 C.Falldorf, Y.Heimbach, C.V.Kopylow and W.Juptner. Efficient reconstruction of spatially limited phase distributions from their sheared representation. Appl. Opt. 46, 5038 (2007)

81 T.Wu, J.D.C Jones, A.J.Moore. High-speed phase-stepped digital speckle pattern interferometry using a CMOS camera. Appl Opt 45(23), 5845 (2006)

82 J.Schwider, R.Burrow, K.-E.Elssner, J.Grzanna, R.Spolaczyk and K.Merkel. Digital wave-front measuring interferometry: some systematic error sources. Appl. Opt., 22(21), 3421 (1983)

83 K.Creath. Temporal phase measurement methods. Interferogram Analysis, D. W. Robinson and G. T. Reid, eds., (IOP, Bristol, UK, (1993)

84 P.A.A.Somers, H. van Brug. A single camera, dual image real-time-phase-stepped shearing speckle interferometer. in Proceedings, Fringe (2001) W. Osten and W. Jutner, eds. , Elsevier (2001), 573. Fringe'01 573 (2001)

85 M.Reeves, A.J.Moore, D.P.Hand and J.D.C.Jones. Dynamic shape measurement system for laser materials processing. Opt. Eng. 42, 2923 (2003)

86 H.Helmers, M.Schellenberg. CMOS vs. CCD sensors in speckle interferometry", Optics and Laser technology, 35, 587 (2003)

87 A. Serov, B. Steinacher, and T. Lasser. Full-field laser Doppler perfusion imaging and monitoring with an intelligent CMOS camera. Opt. Express 13, 3681 (2005).

88 F.Xu, J.E.Ford and Y.Fainman. Polarization-selective computer-generated holograms: design, fabrication, and applications. Appl. Opt. 34 256 (1995)